Influence of monocrystalline surfaces on switching possibilities of 4-anilino-4’nitroazobenzene

Maciej Bazarnik
Faculty of Technical Physics, Institute of Physics
Poznan University of Technology

A thesis submitted for the degree of
Doctor of Philosophy(PhD)

2011

1. Reviewer: prof. Dr.Sci. Bronisław Susła

2. Reviewer: prof. Dr.Sci. Marek Szymoński

Day of the defense:

Signature from head of PhD committee:

Abstract

Molecular electronics proposes to use single molecules as functional units within larger circuits. As a possible switch the cis-trans isomerisation of azobenzene derivative stimulated mostly by electrons and by photons has been extensively studied. On surfaces, this molecule class was mostly investigated on Au(111) because it is known to weakly interact with adsorbed molecules. However, electronic industry is based on semiconductor monocrystalline surfaces, in particular Si(100), which interact more strongly with molecules. Therefore thinking about incorporating molecular switches into devices we must find molecules which can act as a switch on silicon.

In this thesis, I show the properties of 4-anilino-4'-nitroazobenzene molecules. I compare the adsorption configurations of the molecules adsorbed on the Cu(111) and Si(100). I show the evidence of isomerization reactions of single adsorbed molecules on both surfaces and discuss the differences in isomerisation capabilities of adsorbed molecules arising from interactions between the molecules and the substrates.

Streszczenie

Dzisiejsza nanoelektronika dociera do granic miniaturyzacji z wymiarami lateralnymi na poziomie 30 nm. Granica ta może zostać do pewnego stopnia przesunięta. Niemniej dalszy skok technologiczny będzie wymagać wynalezienia technologii pozwalającej na obniżenie rozmiarów podstawowych urządzeń elektronicznych o kolejny rząd wielkości. Występuje kilka trendów w nanonauce i nanotechnologii zmierzających do tego celu. Jednym z nich jest nanoelektronika molekularna. W nanoelektronice molekularnej pojedyncze molekuły są używane jako jednostki funkcyjne w obwodach elektrycznych. Przełączniki są podstawowym urządzeniem dynamicznym i jednocześnie najprostszą dynamiczną jednostką funkcyjną w obwodzie. Jako przełączniki mogą służyć molekuły posiadające minimum dwie stabilne konfiguracje, reagujące powtarzalnie na bodziec zewnętrzny przełączając się pomiędzy tymi konfiguracjami.

Natura zna tego typu rozwiązania. Jednym z nich jest *cis-trans* izomeryzacja retinalu, molekuły wbudowanej w rodopsynę, czyli białko będące budulcem dna oka ludzkiego, a odpowiedzialnego za zmysł wzroku. Retinal absorbując światło ulega reakcji izomeryzacji przechodząc od kompaktowej formy *cis* do wydłużonej formy *trans*. Innymi związkami zdolnymi do reakcji izomeryzacji *cis-trans* są związki azowe, dlatego pochodne azobenzenu wydają się być idealnym kandydatem w tworzeniu przełączników molekularnych. Wywoływana głównie elektronami lub fotonami izomeryzacja tych związków jest tematem wielu badań z ostatnich lat. Myśląc o elektronice trzeba pamiętać, że obwody są budowane na określonym podłożu. Do tej pory, w badaniach jako podłoża najczęściej używano Au(111) ze względu na jego słabą interakcję z adsorbatami. Z drugiej strony przemysł elektroniczny opiera się na technologii krzemowej. Dlatego, myśląc o wykorzystaniu molekuł w przemyśle należy znaleźć przełączniki molekularne działające na

powierzchni krzemu. Krzem w porównaniu z metalami jest powierzchnią eksperymentalnie dużo trudniejszą i bardziej wymagającą. Badania prowadzone na powierzchni krzemu są dużo bardziej czasochłonne. Dlatego też jako temat mojej pracy doktorskiej wybrałem wpływ powierzchni monokrystalicznych na zdolność izomeryzacji pochodnej azobenzenu. Celem pracy było wyznaczenie tego wpływu i znalezienie odpowiedzi na pytanie, czy na podstawie wyników uzyskanych dla molekuł zaadsorbowanych na metalu można przewidzieć wyniki dla molekuł zaadsorbowanych na krzemie.

Jako modelową molekułę wybrałem 4-anilino-4'-nitroazobenzen. W pierwszej części pracy wybrałem podłoże Cu(111), będące dużo bardziej reaktywną powierzchnią od Au(111), a co za tym idzie bliższą Si(100). Powodzenie procesu izomeryzacji badanej cząsteczki na Cu(111) dałoby nadzieję na przeprowadzenie tego procesu na podłożu krzemowym. Aby wyznaczyć wpływ powierzchni musiałem zrealizować pięć zadań:

- zbudować nowy układ próżniowy przystosowany do badań powierzchni metalicznych oraz powierzchni krzemu,
- scharakteryzować czyste podłoża Cu(111) oraz Si(100),
- dogłębnie scharakteryzować wybrane molekuły używając makroskopowych metod spektroskopowych,
- osadzić pojedyncze molekuły na powierzchni Cu(111) i Si(100), oraz scharakteryzować ich konfiguracje adsorpcyjne,
- wywołać reakcje izomeryzacji na obu powierzchniach.

Głównym narzędziem badawczym w skali nano jest ultra wysokopróżniowy (UHV) niskotemperaturowy (LT) skaningowy mikroskop tunelowy (STM) pracujący w temperaturze poniżej 6 K. Dodatkowo, w pracy badawczej stosowałem metody makroskopowe takie jak spektroskopia UV-VIS, spektroskopia IR, spektroskopia Ramana, czy fotoliza błyskowa. Interpretacja danych jest wspomagana numerycznymi metodami chemii kwantowej - obliczenia struktury geometrycznej za pomocą teorii funkcjonału gęstości, metod półempirycznych (np. PM3, ZINDO).

Pierwsza część rozprawy doktorskiej traktuje o podstawach teoretycznych badanych procesów oraz o sposobach ich badania. Następnie, skrótowo przedstawiam wszystkie wykorzystane metody eksperymentalne. Dalej omawiam zaprojektowany i wykonany układ eksperymentalny, jak również układ eksperymentalny z Uniwersytetu Leibniza w Hanowerze. W kolejnej części prezentuję wyniki badań i ich dyskusję, a całość zakończona jest podsumowaniem. W tym rozszerzonym streszczeniu pominę pierwsze trzy rozdziały i zacznę od opisu zaprojektowanego układu eksperymentalnego.

Projekt układu opiera się na 4 założeniach:

- trójstopniowy system załadunku próbki,
- oddzielenie komory preparacyjnej od komory analitycznej,
- najniższe ciśnienie w komorze analitycznej lepsze niż 1×10^{-10} mbar,
- kompatybilność z eksperymentami związanymi z molekułami organicznymi.

Komora analityczna jest wyposażona w skaningowy mikroskop próbnikowy STM/AFM firmy Omicron pracujący w warunkach ultra wysokiej próżni, oraz spektrometr LEED/AES firmy OCI. Komora preparacyjna posiada działo jonowe, układ do wygrzewania (działo elektronowe, grzałka oporowa, podłączenie do przepuszczania prądu przez próbkę) i chłodzenia próbek, 3 źródła parowania w tym jedno przeznaczone do osadzania molekuł organicznych. Cały system umożliwia badania powierzchni półprzewodników (krzem, german, tellurek bizmutu) oraz metali (miedź, molibden, złoto, wolfram).

Powierzchnia Cu(111) ma trójkrotną symetrię i nie wykazuje żadnej rekonstrukcji powierzchniowej, a jedynie relaksację powierzchniową. Posiada stan powierzchniowy o energii -435 mV względem energii Fermiego, tworzący quasi 2D słabo związany gaz elektronowy. Ten stan powierzchniowy w znacznym stopniu jest odpowiedzialny za reaktywność chemiczną tej powierzchni. Struktura elektronowa Cu(111) jest zdominowana przez elektrony pasma d, ze zmniejszoną gęstością w okolicach energii Fermiego, składającą się głównie z elektronów pasma s. Powierzchnia Si(100) jest dużo bardziej skomplikowana, zarówno geometrycznie, jak i elektronowo. Rekonstruuje w komórkach typu c(4x2) lub p(2x2), zależnie od rodzaju domieszkowania krzemu. W temperaturze pokojowej jest obserwowana rekonstrukcja (2x1), która jest efektem ciągłego ruchu dimerów krzemu. W niższych temperaturach ruch ten jest zamrażany. Niemniej w temperaturach kriogenicznych, poniżej 40 K może również występować rekonstrukcja (2x1) związana z oddziaływaniem ostrza STM z podłożem. W strukturze elektronowej poniżej energii Fermiego dominują elektrony pasma p, powyżej dominuje pasmo d.

4-anilino-4'-nitroazobenzen jest zbudowany z trzech aromatycznych pierścieni węglowych połączonych odpowiednio grupą aminową (-NH-) i azową (-N=N-), a do końcowego pierścienia podstawiona jest grupa nitrowa (-NO_2). Molekuła posiada dwie stabilne konformacje między którymi może izomeryzować poprzez dwa przejścia: inwersyjne związane z przejściem S_0-S_1 oraz rotacyjne związane z przejściem S_0-S_2. Badania na temat izomeryzacji pojedynczych, zaadsorbowanych molekuł na powierzchni Au(111) wykazały, że po adsorpcji molekuła zachowuje zdolność do zmiany konformacji.

Część badawczą rozpocząłem od obliczeń strukturalnych wolnej izolowanej molekuły metodą DFT. W ten sposób wyznaczyłem obie konformacje , długość wiązań i kąty torsyjne w molekule. Następnie wyznaczyłem przestrzenny rozkład ładunku zrzutowany na stałą gęstość stanów elektronowych. Sprawdziłem również możliwości adaptacyjne molekuły poprzez rotację niektórych grup wokół osi pojedynczych wiązań. Wiązanie grupy C_6H_5NH- z resztą molekuły jest łatwo rotowane, z różnicą energetyczną pomiędzy kolejnymi konfiguracjami mniejszą niż 1 eV. Dane te były wykorzystywane w dalszej interpretacji danych.

Przeprowadziłem charakteryzację molekuł w stanie stałym, za pomocą spektroskopii IR, UV-VIS i Ramana. Wyznaczyłem pasma odpowiedzialne za przejścia S_0-S_1 oraz S_0-S_2, odpowiednio 250 nm i 414 nm dla izomeru *cis*, oraz 318 nm i 508 nm dla izomeru *trans*. Pasma są szerokie na 50 nm. Podczas badań molekuł w cieczach lub w fazie gazowej wartości pasm ulegają zmianie. Porównując widma IR i Ramana z wynikami obliczeń, wyznaczyłem i scharakteryzowałem szereg modów wibracyjnych molekuły. Wibracje te zostały użyte do identyfikacji konfiguracji adsorpcyjnych molekuł na Cu(111).

W kolejnym etapie, przeprowadziłem badania dynamiki reakcji izomeryzacji metodą fotolizy błyskowej. Izomeryzacja wywoływana laserem o długości fali 266 nm zachodzi poprzez wyższe poziomy singletowe, a czas życia poziomu S_2, z którego zachodzi reakcja izomeryzacji został wyznaczony na 218 ns ±12 ns. Ten stosunkowo długi czas życia i powolna reakcja pozwala sądzić, że na powierzchni zajdzie proces izomeryzacji. Natomiast istnieje prawdopodobieństwo, że długi czas życia stanu wzbudzonego molekuły ulegnie drastycznemu skróceniu jeśli na powierzchni zachodziłyby procesy transferu energii Dextera, czy Förstera.

W badaniach, które prowadziłem na powierzchni Cu(111) zastosowałem fizysorpcję jako metodę osłabienia interakcji między podłożem, a molekułą. Pojedyncze molekuły zostały osadzone na powierzchni miedzi utrzymywanej w temperaturze 100 K i 20 K. Wynikiem osadzenia na podłożu w temperaturze 100 K była dominacja fragmentów molekuły na powierzchni, związana z dysocjacyjną adsorpcją. Przy temperaturze podłoża równej 20 K dominowały całe molekuły , lecz brak energii na przejście do jednej ze stabilnych konfiguracji adsorpcyjnych spowodował, że obserwowałem wiele różnych konfiguracji. Tylko dwie z nich były stabilne, reszta przełączała się nawet w trakcie rejestracji obrazu STM. Aby rozpoznać, która z dwóch stabilnych konfiguracji jest izomerem *cis*, a która izomerem *trans* przeprowadziłem obliczenia strukturalne w oparciu o metody półempiryczne, jako że DFT nie odwzorowywuje fizysorpcji. W oparciu o te obliczenia oraz o pomiary spektroskopii nieelastycznie tunelujących elektronów dla obu izomerów rozpoznałem obie konfiguracje adsorpcyjne. Aby potwierdzić fizysorpcję molekuł na powierzchni wywołałem chemisorpcję molekuł za pomocą impulsu wysokiego napięcia i wysokiego prądu (150V, 1mA). W wyniku zastosowania powyższej procedury obserwowałem molekuły o kształcie molekuł chemisorbowanych na powierzchni Au(111). Transformacji z fizysorcji do chemisorpcji nie można dokonać za pomocą wygrzewania ze względu na termiczną desorpcję molekuł.

W badaniach na powierzchni Si(100) zastosowanie fizysorpcji okazało się niemożliwe. Nawet przy osadzaniu na podłoże w temperaturze 20 K otrzymywałem molekuły chemisorbowane. Na powierzchni krzemu obserwowałem trzy stabilne konfiguracje adsorpcyjne. W tej rozprawie, w dalszych rozważaniach nie brałem pod uwagę konfiguracji będącej swego rodzaju aglomeratem molekuł. Z pozostałych dwóch konfiguracji jedna jest konfiguracją molekuły leżącej na powierzchni (ponad 70% populacji), gdzie przynajmniej dwa pierścienie są związane z podłożem, a druga jest konfiguracją stojącą (około 11% populacji), gdzie jeden pierścień jest przyłączony do powierzchni, natomiast część nitrobenzenowa molekuły jest prostopadła do powierzchni. Identyfikacji konfiguracji dokonałem na podstawie pomiarów STM, STS oraz symulacji DFT. Okazało się, że konfiguracja stojąca ma dwie wariacje. Tym wariacjom przypisałem formy *cis* i *trans* stojącej części molekuły. W tej konfiguracji grupa aminowa izoluje część nitroazobenzenową od powierzchni dając szanse na izomeryzację, pomimo silnego chemicznego wiązania do podłoża.

Molekuły zaadsorbowane na obu powierzchniach zbadałem pod kątem możliwości wywołania reakcji izomeryzacji. Stale utrzymując próbkę w temperaturze poniżej 6K wykluczyłem możliwość termicznej izomeryzacji molekuł. Osłona termiczna kriostatu osłaniała powierzchnię i zaadsorbowane molekuły od wszelkich sztucznych źródeł światła. Spontaniczne reakcje izomeryzacji zostały w ten sposób wyeliminowane. Do wywołania reakcji użyłem nieelastycznie tunelujących elektronów oraz promieniowania elektromagnetycznego z zakresu UV-VIS.

Zakres energetyczny elektronów w eksperymentach na Cu(111) wynosił $< 150 \text{ meV}, 600 \text{ meV} >$. Reakcje izomeryzacji zaczęły pojawiać się powyżej 200 meV, a wydajność tych reakcji wzrastała wraz z energią elektronów. Nie zaobserwowałem natomiast brzegowej energii aktywacji, która mogłaby świadczyć o energii aktywacji konkretnego przejścia. Poza pojedynczymi aktami izomeryzacji obserwowałem również reakcje wielokrotne, których efektem była rotacja molekuły na powierzchni. Izomeryzacja *trans-cis* jest wydajniejsza niż reakcja odwrotna. Wskazuje to, że *cis* jest formą energetycznie korzystniejszą i stabilniejszą na podłożu. Energie elektronów pozwalające na izomeryzację molekuły są o rząd wielkości mniejsze niż energie fotonów potrzebne do tego samego celu. Świadczy to o odmiennym mechanizmie reakcji. Istnieją dwie możliwości: pompowanie energii poprzez kolejne poziomy wibracyjne, aż do energii poziomu wzbudzonego $\mathrm{S_n}$, bądź występuje proces adiabatyczny, który zachodzi stricte poprzez poziomy wibracyjne. Pojedyncza izomeryzacja jest procesem dominującym w zakresie $<$ 375 meV, 500 meV$>$ z wydajnością na poziomie $10^{-7}\ \bar{\mathrm{e}}^{-1}$. Jest to o rząd wielkości wyższa wydajność w porównaniu z tą obserwowaną na powierzchni Au(111). Z eksperymentu wynika, że nie występuje zależność wydajności i kierunku reakcji od miejsca impulsu nieelastycznie tunelujących elektronów.

Zakres energii tunelujących elektronów w eksperymentach na Si(100) musiał być odmienny ze względu na przerwę energetyczną krzemu i wynosił $<1,7$ eV, 5 meV$>$. Poza pojedynczymi zaobserwowanymi reakcjami, molekuły w żadnej z form nie reagowały na nieelastycznie tunelujące elektrony. Pojedyncze zaobserwowane reakcje nie były reakcjami izomeryzacji, a raczej dekompozycją molekuły. Jest to związane z bardzo silnym wiązaniem molekuły w pozycji planarnej z podłożem (na poziomie 9 eV), które musiałoby być zerwane, aby izomeryzacja była możliwa. W przypadku molekuły stojącej, najprawdopodobniej odpowiedzialna jest zmiana orientacji orbitalu w porównaniu z molekułą leżącą. Przez to elektron tunelujący z ostrza do próbki, aby wzbudzić molekułę, musiałby zmienić swój kierunek pędu. Proces taki jest mało prawdopodobny, w związku z czym izomeryzacja nie była obserwowana.

Drugim czynnikiem stosowanym w eksperymentach wymuszającym izomeryzację było promieniowanie elektromagnetyczne z zakresu UV-VIS generowane w lampie rtęciowej poza układem UHV, a świecące na próbkę przez okno szafirowe i otwieraną przesłonę w osłonie kriogenicznej STM. Procedurę naświetlania zaczynałem od zrobienia obrazu STM powierzchni z charakterystycznym elementem, takim jak nietypowy kształt tarasu czy dyslokacja. Następnie ostrze STM oddalałem maksymalnie od powierzchni próbki i od kierunku padania światła. Próbka była naświetlana, a w trakcie naświetlania temperatura próbki była stale monitorowana. Po naświetlaniu ostrze STM wracało na swoją pozycję i charakterystyczny punkt był odnajdywany. Następnie, rejestrowałem obraz po naświetlaniu. Porównanie obrazów sprzed i po pozwoliło stwierdzić, czy reakcja zaszła.

Na podłożu Cu(111) ponad 600 molekuł wystawiłem na pełne spektrum lampy rtęciowej przez 20 minut. Odpowiada to dawce 1×10^{20} cm^{-2} fotonów. 4% populacji uległo izomeryzacji, a 0,5% uległo wielokrotnej izomeryzacji obserwowanej jako rotacja molekuły. Rozstrzygnięcie, który spośród kilku możliwych mechanizmów reakcji zachodzi na powierzchni było możliwe dzięki przeprowadzeniu eksperymentu z zastosowaniem filtrów selektywnych. W ten sposób dowiodłem, że za reakcje izomeryzacji odpowiadają linie widmowe 260 nm, 280 nm i 290-300 nm. Oznacza to, że mechanizm reakcji jest bezpośredni i jest związany z przejściem $S_0 - S_2$, czyli jest to mechanizm rotacji wokół wiązania podwójnego w grupie azowej. Licząc wielokrotną izomeryzację jako podwójną i biorąc pod uwagę, że tylko fotony o energiach poniżej 315 nm biorą udział w procesie, efektywny przekrój czynny izomeryzacji wynosi 6×10^{-20} cm^{-2}.

Na powierzchni Si(100), przełączeniu za pomocą światła może ulec jedynie forma stojąca molekuły. Ponieważ na powierzchni tylko 11% populacji przedstawia tę konfigurację adsorpcyjną, w okienku pomiarowym znajdowało się średnio zaledwie 20 molekuł. Wydłużając czas naświetlania, pierwsze efekty uzyskałem po 180 minutach naświetlania. Sprawdzałem również dłuższe czasy to jest 300 oraz 600 minut. W przypadku czasów 180 i 600 minut zachodziła tylko izomeryzacja *trans-cis*. Natomiast w przypadku naświetlań w czasie 300 minut stosunek izomeryzacji *cis-trans* i *trans-cis* jest bliski jedności. Blisko 17% z ponad 160 naświetlonych molekuł izomeryzowało na powierzchni, jednak przy znacznie wydłużonych czasach naświetlania. Dało to efektywny przekrój czynny izomeryzacji na poziomie $1,6 \times 10^{-21}$ cm^{-2}. Ponieważ nitrobenzenowa część molekuły jest izolowana od powierzchni (na co wskazują obliczenia DFT) to reakcja izomeryzacji zachodzi w sposób podobny jak dla molekuł swobodnych.

Analizując możliwość transferu molekuł z powierzchni metalicznej na krzemową należy wziąć pod uwagę następujące czynniki:

- różna geometria podłoża powoduje, że nie wszystkie części molekuły jednakowo oddziaływują z powierzchnią,
- struktura elektronowa powierzchni znacznie się różni: na metalach typu Au i Cu dominują elektrony pasma d, natomiast na Si dominują elektrony pasma p,
- mechanizm reakcji izomeryzacji będzie się różnił w związku z innym przekrywaniem się pasm HOMO-LUMO oraz pasma d podłoża,
- geometria orbitali związanych z grupą azową wpływa na prawdopodobieństwo wzbudzenia izomeryzacji za pomocą nieelastycznie tunelujących elektronów.

Podsumowując, wykonałem wszystkie pięć zadań wytyczonych w rozprawie doktorskiej.

- Zaprojektowałem i zbudowałem nowy układ UHV, umożliwiający pracę z próbkami metalicznymi jak i półprzewodnikowymi. System ten jest wyposażony w działo jonowe oraz urządzenia umożliwiające zastosowanie różnych metod wygrzewania próbek prowadzących do ich oczyszczania . Projekt systemu maksymalizuje stabilność mikroskopu pozwalając na bardzo dokładne pomiary STM.
- Wszechstronnie scharakteryzowałem molekuły 4-anilino-4'-nitroazobenzenu. Wyznaczyłem i zidentyfikowałem ich poziomy wibracyjne, zmierzyłem spektrum absorpcyjne dla ciała stałego jak i roztworu oraz oznaczyłem przejścia $S_0 - S_1$ i $S_0 - S_2$. Prędkość reakcji izomeryzacji oraz czas życia stanu wzbudzonego zmierzyłem metodą fotolizy błyskowej.
- Czyste powierzchnie Si(100) i Cu(111) scharakteryzowałem przy użyciu STM i DFT.

- Opracowałem metodę osadzania pojedynczych molekuł 4-anilino-4'-nitroazobenzenu na czystych powierzchniach Cu(111) i Si (100). Zidentyfikowałem konfiguracje adsorpcyjne molekuł za pomocą STM, obliczeń DFT, IETS i STS.
- Wywołałem reakcje izomeryzacji na obydwu powierzchniach. Na powierzchni Cu(111) izomeryzacja nieelastycznie tunelującymi elektronami okazała się bardzo efektywna w zakresie niskich energii. Wymusiłem również bezpośrednią fotoizomeryzację z porównywalnie wysokim efektywnym przekrojem czynnym. Izomeryzacji towarzyszy blisko zasięgowa dyfuzja, co sprawia że przełącznik nie jest stricte bistabilny. Na powierzchni Si(100) tylko stojące konfiguracje adsorpcyjne okazały się zdolne do izomeryzacji. Fotoizomeryzację na podłożu Si(111) wymusiłem z niższym efektywnym przekrojem czynnym niż na Cu(111). Nieelastycznie tunelujące elektrony nie wywołują izomeryzacji w związku z konieczną zmianą momentu pędu elektronu. Przewagą fotoizomeryzacji na Si(100) jest bistabilność molekuł wywołana chemisorpcją.

To all those close to me: my family and friends.

Acknowledgements

I would like to offer my deep thanks to Prof. Ryszard Czajka for his support and good words throughout my struggle with my PhD, to Prof. Karina Morgenstern for her invitation to Hannover and long hours spent on fruitful discussions, and to my colleagues from the laboratories in Poznan and Hannover: Maciej Cęgiel, Wojtek Koczorowski, Hubert Gojżewski, Jakub Dąbrowski, Michał Hermanowicz, Jörg Henzl, Jędrzej Schmeidel, and Sarah Heighorn for their support, patience and understanding.

Contents

Acronyms **vi**

1 Introduction **1**

1.1 Molecular Nanoelectronics 1

1.2 Aims 2

2 Theoretical Concepts **4**

2.1 Elastic and Inelastic Electron Tunneling 4

2.1.1 Elastic Tunneling in the Scanning Tunneling Microscope 6

2.1.2 Inelastic Tunneling in the Scanning Tunneling Microscope 8

2.2 Computational Methods in Nanoscience 10

2.2.1 Density functional theorem 11

2.2.2 Semi-empirical methods 13

2.3 *Cis* - *Trans* Isomerization 14

3 Methods **17**

3.1 The Scanning Tunneling Microscope 17

3.1.1 Scanning tunneling spectroscopy 20

3.1.2 Inelastic electron tunneling manipulation 22

3.1.3 Irradiation of the sample 23

3.1.4 Local high voltage/high current treatment 24

3.2 Optical spectroscopy 25

3.2.1 Infrared Spectroscopy 25

3.2.2 Raman Spectroscopy 27

3.2.3 Flash Photolysis 28

3.3 Computer Simulations 29

3.3.1 ArgusLab 30
3.3.2 ABINIT 32
3.3.3 Fireball 32

4 Experimental Setups **33**
4.1 Room Temperature Ultra-high Vacuum Chamber 33
4.1.1 Analysis 33
4.1.2 Preparation 35
4.1.3 Pumping system 35
4.2 Low Temperature Ultra-high Vacuum Chamber 36
4.2.1 Analysis 36
4.2.2 Preparation 37
4.2.3 Pumping system 38

5 Materials **39**
5.1 Monocrystalline Substrates 39
5.1.1 Copper(111) 39
5.1.2 Silicon(100) 41
5.2 4-anilino-4'nitroazobenzene 44

6 Results and Discussion **50**
6.1 Calculated Molecules Structure in Gas Phase 50
6.2 Optical Spectroscopy 52
6.3 Flash Photolysis 56
6.4 Adsorption Geometries at Monocrystalline Surfaces 58
6.4.1 4-anilino-4'nitroazobenzene on Cu(111) 58
6.4.2 4-anilino-4'nitroazobenzene on Si(100) 63
6.5 The IETS of Single Molecules 71
6.6 *Cis-Trans* Isomerization Induced by Light and Electrons 74
6.6.1 IET induced surface processes on Cu(111) 74
6.6.2 IET induced surface processes on Si(100) 76
6.6.3 Photoisomerization at the Cu(111) surface 78
6.6.4 Photoisomerization at the Si(100) surface 82

7 Conclusions **84**

Apprendix 1 **86**

References **90**

List of Figures **98**

List of Tables **100**

Acronyms

1D one dimensional

2D two dimensional

3D three dimensional

ACN acetonitrile

AM1 Austin Model 1

amine -NH-

anilino C_6H_5NH-

azo -N=N-

DAC digital-analog converter

DFT density functional theorem

DOS density of states

ESP electrostatic potential

fcc faced-centreed cubic

FTIR fourier transform infrared spectroscopy

GGA generalized gradient approximation

HOMO highest occupied molecular orbital

IET inelastic electron tunneling

IETS inelastic electron tunneling spectroscopy

IR infrared spectroscopy

IVC *I* to *V* converter

LDA local density approximation

LDOS local density of states

LEED/AES low energy electron diffraction / Auger electron spectroscopy

LN liquid nitrogen

LT low temperature

LUMO lowest unoccupied molecular orbital

MNDO Modified Neglect of Diatomic Overlap

MO molecular orbital

NDDO neglect of diatomic overlap

nitro -NO_2

PM3 Parametric Method Number 3

RT room temperature

SCF self consistent field

SPM scanning probe microscope

STM scanning tunneling microscope

STS scanning tunneling spectroscopy

TSP titanium sublimation pump

UHV ultra-high vacuum

UV-VIS ultraviolet-visible

Chapter 1

Introduction

1.1 Molecular Nanoelectronics

Nowdays, nanoelectronics are reaching the smallest possible dimensions at a level of 30 nm; and to some extent this border might even be moved beyond today's limit. Nevertheless, there is a need to develop new technologies that would take the place of the standard silicon based technology, moving the miniaturization an order of magnitude down. There are currently several trends in science, one of which is the so called molecular nanoelectronics. This trend uses organic molecules as the building blocks for electronic devices. There are several devices make up the building blocks of electronics, namely: wire, capacitor, resistor, switch, and transistor. Only the switch and transistor are, however, dynamic elements that change their properties; and of these switches are the simpler.

Nature has developed many intriguing solutions to people's problems. Therefore, just as in many other branches of science and technology so too in molecular electronics people try to mimic nature. Switches, being the first dynamic devices, are now attracting much attention. In nature in the retina of the human eye there is a protein called rhodopsin responsible for the sense of sight. The photoactive part of this protein is retinal, a molecule incorporated into the rhodopsin. This molecule has two isomers: the elongated *trans* and the compact *cis*. The transition between these two forms is induced by light irradiation, and the rearrangement of the whole rhodopsin causes the electric impulse in the eye - and as a consequence the sense of sight.

One modern concept is to mimic the behavior of retinal, using molecules capable of isomerization as switches. For application reasons, though, the molecules have to be incorporated onto surfaces. A perfect solution is to incorporate molecular electronic's active parts such as switches into existing silicon electronic technology. Therefore, the ultimate goal is to build a molecular switch working on a silicon surface. As single molecules like retinal or azobenzen are very small, with lateral dimensions in the range of $< 1\mathrm{nm}, 3\mathrm{nm} >$, there are only a limited number of investigation techniques with sufficient resolution possible in order to achieve this.

Scanning probe microscopy (SPM), developed by G. Binnig and H. Rohrer in the early 80s[1, 2], has proved to be a universal technique to characterize the versatile physical properties of surfaces and nanostructures. The potential power of scanning probe microscopes (SPMs) has been shown in thousands of papers, on imaging surfaces with sub-nanometer (atomic) resolution, on the determination of the electron properties of nanostructures (quantum size effects - QSE, the coulomb blockade - CB), on the magnetic properties at the nanoscale and the mechanical properties of nano-objects e.g. of nanotubes, fullerenes, etc. SPMs enables also manipulations of individual molecules and atoms[3]. The evolution of the SPMs head construction, driving electronics and software forwards, enables more and more detailed studies of smaller and smaller objects such as clusters, individual molecules and atoms.

Electronic induced reactions, including the cleaving of molecule-surface bonds by inelastic tunneling of electrons from the scanning tunneling microscope (STM) tip, seems to be the most appropriate method for precise control of molecular reactions at a single site on a surface. All single molecules experiments are performed at low temperatures (LT, 5K) to reduce the thermal energy and therefore reduce the possibility of uncontrolled surface processes such as the molecules rotation or diffusion.

In this thesis I employ a very wide spectrum of techniques to investigate the electronic and chemical properties of organic systems on the atomic scale. The gained knowledge is believed to strongly influence many different areas of industry in particular molecular nanoelectronics.

1.2 Aims

The main task of this thesis is to determine the influence of monocrystaline surfaces on the switching possibilities of azobenzene derivatives. 4-anilino-4'nitroazobenzene is chosen as a model molecule and two substrates, Cu(111) and Si(100), are considered. To achieve this goal five tasks had to be accomplished:

- In order to investigate single molecules adsorbed on surfaces, the quality of those surfaces must be at the highest level. For this purpose a new UHV system capable of the investigation of clean metal and semiconductor surfaces had to be designed and built in Poznan.
- Clean Si(100) and Cu(111) surfaces were to be characterized by means of STM and density functional theorem (DFT).
- Next 4-anilino-4'nitroazobenzene molecules have to be characterized throughout using macroscopic methods.
- Single molecules were to be deposited onto Si(100) and Cu(111) surfaces. Adsorption configurations are to be recognized.
- Isomerization reactions were to be induced on both surfaces.

Finally, the influence of the surfaces on the switching possibilities of molecules was determined.

Chapter 2

Theoretical Concepts

2.1 Elastic and Inelastic Electron Tunneling

Tunneling is a quantum mechanical effect in which a particle has a non-zero probability of overcoming an energetic barrier even though its energy would not normally allow this according to classical physics. For simplicity, physicists use a one dimensional (1D) model to describe this phenomena. A particle traveling from left to right encounters a potential barrier of an energy V_0 and width a (see Figure 2.1).

$$V(x) = \begin{cases} V_0 & 0 \leq x \leq a \\ 0 & x < 0 \text{ or } x > a. \end{cases} \tag{2.1}$$

For a particle with $E < V_0$ the solution of Schrödinger's equation is given by three wave functions for three regions respectively

$$\begin{cases} \Psi_1(x) = Ae^{ik_1x} + Be^{ik_1x} & x < 0 \\ \Psi_2(x) = De^{-ik_2'x} + Fe^{-ik_1'x} & 0 < x < a \\ \Psi_3(x) = Ce^{ik_1x} & x > a. \end{cases} \tag{2.2}$$

where,

$$\begin{array}{l} k_1 = -\frac{\sqrt{2mE}}{\hbar} \\ k_2 = -\frac{\sqrt{2m(V_0-E).}}{\hbar} \\ k_2' = ik_2 \end{array} \tag{2.3}$$

Now we define the border conditions for these equations

$$\begin{array}{ll} \Psi_1(0) = \Psi_2(0) & \Psi_2(a) = \Psi_3(a) \\ \frac{\partial}{\partial x}\Psi_1(0) = \frac{\partial}{\partial x}\Psi_2(0) & \frac{\partial}{\partial x}\Psi_2(a) = \frac{\partial}{\partial x}\Psi_3(a) \end{array} \tag{2.4}$$

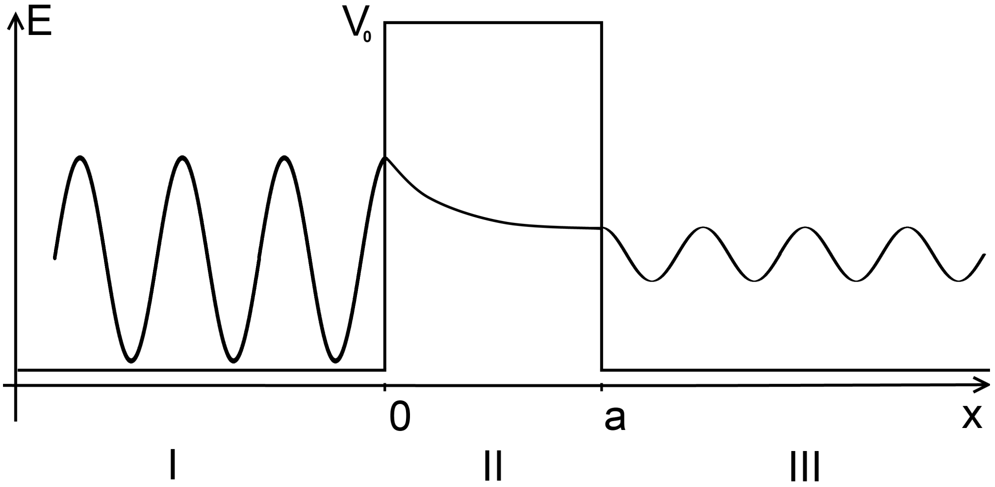

Figure 2.1: Schematics of the energetic barrier - Three areas are marked on the schematic: I and III, where the potential energy equals 0, and II where the potential energy equals V_0.

From this, one can derive four equations defining B, C, D, and F as a function of the incoming waves amplitude A.

$$\begin{cases} A + B = D + F \\ ik_1A - ik_1B = -ik_2D + ik_2F \\ De^{ik_2a} + Fe^{ik_2a} = Ce^{ik_1a} \\ -ik_2De^{-ik_2a} + ik_2Fe^{ik_2a} = ik_1Ce^{ik_1a} \end{cases} \tag{2.5}$$

Defining the transmition factor T as a ratio of the flux between the incident particles and the back scattered particles, one can derive such an equation as follows:

$$T = \frac{1}{1 + \left(\frac{k_1^2+k_2^2}{2k_1k_2}\right)^2 \sinh(k_2a)} \tag{2.6}$$

Because the k_1 and k_2 are related to the particles' energy and the energy of the barrier, the T also is a function of those energies. In fact, only the effective energy of the barrier is important; it doesn't matter if the barrier has very high energy and is very thin, or vice versa. The clue is that the probability of tunneling through the barrier by a particle depends on both the parameters of the particle itself and the parameters of the barrier.

In reality, the phenomena is a bit more complicated than it is depicted above as it goes from 1D to 2D or even 3D situations. In the STM the situation is three dimensional

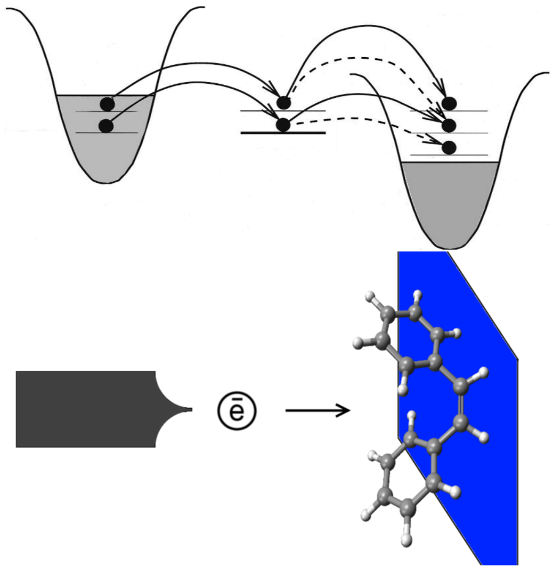

Figure 2.2: Elastic and inelastic tunneling processes - The energetic scheme of tunneling processes. A solid arrow indicates an elastic process in which the electron energy is preserved, while a dashed arrow indicates an inelastic electron tunneling.

(3D) where the electrons tunnel from the atomically sharp tip to the sample. There is a tunnel junction with a metal electrode (the tip), vacuum, air or liquid, as the barrier and a substrate as the second electrode. Electrons can tunnel in two fashions (see Figure 2.2), either elastically when they preserve their energy while tunneling, or inelastically when they give part of their energy to the medium through which they are tunneling [4, 5].

2.1.1 Elastic Tunneling in the Scanning Tunneling Microscope

In the STM in principle the tunneling current occurs between an atomically flat sample and a metallic pyramid shaped tip preferably with a single atom ending. There are not many approaches to theoretically treat tunneling electrons in the STM. The first and qualitatively giving reasonable fit of a theory to data gathered in measurements is the approach of Tersoff and Hamann [6]. According to Bardeen's formalism [7] the tunneling current is given to the first order by:

$$I = \frac{2\pi e}{\hbar} \sum_{\mu,\nu} f(E_\mu)[1 - f(E_\nu + eV)]|M_{\mu\nu}|^2 \sigma(E_\mu - E_\nu), \tag{2.7}$$

where $f(E)$ is the Fermi function, the applied voltage is marked as V,$M_{\mu\nu}$ is the tunneling matrix element between the probe and surface states, and E_μ and E_ν are the energy of the probe state and sample state in the absence of tunneling respectively. Essentially to solve this problem under a low temperature and small voltage limits, means to calculate the $M_{\mu\nu}$. Bardeen showed that for this one needs both surface and probe wave functions. For metallic substrates and probes it is reasonable to assume that the work functions are similar and for simplicity can be treated as identical. Tersoff and Hamann assumed a general expression for wave function in negligible potential [6]:

$$\psi_\nu = \Omega_s^{-1/2} \sum_G a_G \exp((\kappa^2 + \vec{\kappa}_G^2)^{1/2} z) \exp(i\vec{\kappa}_G \cdot \vec{x}), \tag{2.8}$$

where Ω_s is the sample volume, $\kappa = \hbar^{-1}(2m\phi)^{1/2}$ is the minimum inverse decay length for ψ in vacuum, ϕ is a work function $\vec{\kappa}_G = \vec{k}_{||} + \vec{G}$ where $\vec{G}$ is the reciprocal-lattice vector, and $\vec{k}_{||}$ is the surface Bloch wave vector of the state.

The probe is modeled as a locally spherical potential well of R the radius, with the center located at $\vec{r}_0$ and at the d distance to the surface [6]:

$$\psi_\mu = \Omega_t^{-1/2} c_t \kappa R e^{\kappa R} (\kappa|\vec{r} - \vec{r}_0|)^{-1} \exp(-\kappa|\vec{r} - \vec{r}_0|), \tag{2.9}$$

here Ω_t is the probe volume, and c_t is determined by the probe geometry, electronic structure and tip-vacuum boundary conditions. The ψ_μ is correctly normalized if c_t is of the order of 1.

Using such wave functions Tersoff and Hamann showed that the tunneling current can be described as [6]:

$$I = 32\pi^3 \hbar^{-1} e^2 V \phi^2 D_t(E_f) R^2 \kappa^{-4} e^{2\kappa R} \times \sum_\nu |\psi_\nu(\vec{r}_0)|^2 \delta(E_\nu - E_F), \tag{2.10}$$

where D_t is the density of states per unit volume of the probe. The crucial approximation in this approach is the evaluation of the matrix element only for s-wave tip wave function. However, a more exact treatment would require more specific information about probe wave function and therefore would not reduce to an explicit equation such as (2.10). Once substituting typical metallic values into (2.10), an expression for tunneling conductance is obtained [6]:

$$\sigma = 0.1R^2 e^{2\kappa R}\rho(\vec{r}_0, E_F), \tag{2.11}$$

here $\rho(\vec{r}_0, E_F)$ is the local density of states at Fermi energy in a point $\vec{r}_0$. Again it is important to remember that this model is limited to low voltage that is typically lower than several mV. But a general conclusion extrapolating from this model is that the tunneling current and therefore images registered with the scanning tunneling microscope highly depend on the local density of states at the energy $E_F - eV$. This energy dependence makes the STM a very powerful but tricky tool for surface analysis.

2.1.2 Inelastic Tunneling in the Scanning Tunneling Microscope

Inelastic processes can occur when an electron tunneling from the tip to the sample (or the other way around) encounters on its way a vibrator, a molecule or a possible surface phonon. Let's assume that we are in a low temperature regime, preferably lower than 10 K, then a probability of finding a vibrator in an excited state is negligible. In this case only an energy transfer from the electron to the vibrator is possible. The only way of opening an inelastic channel is that the electron possesses an energy not smaller than the quantum of the vibration [8].

Theoretical concepts of inelastic electron tunneling (IET) are focused on two main aspects. The first group treats instrinctly only the vibrations in molecules and only afterwards tries to show an influence on the tunneling current. The second group is focused on describing a measurable quantity such as the conductance of the tunneling junction. The second approach is more useful from the point of view of an experimentalist. Theoretical models describing conductance are focused on several approaches such as the numerical evaluation of transmission functions based on a suitable model Hamiltonian [9–14], or a more quantitative approach based on scattering formalism [15, 16], or those based on Green's functions [17, 18]. In the first approach the vibronic coupling in effective Hamiltonian appears as a parameter and therefore is not a consistent theory. Scattering formalism fixes the problem to some extent, still leaving the parameter of a lesser importance. Only since Troisi and Ratner [18–20] developed their approach based on Green's functions is a parameter free calculation of inelastic conductance and its quantitative role in respect to an elastic channel possible.

Troisi and Ratner calculate the transport on the basis of a Transmission operator matrix in which all elements are Green's functions. This matrix is modified for the vibronic case by defining the initial and final states as Born-Oppeneimer products of an electronic wave function and nuclear wave function. In their theory the first-order correction to the elastic conductation, represented by the truncated expansion, is nonzero only if the initial and final states differ by one vibrational quantum. Taking into account low temperature and bias regime, and assuming that the local density of states (LDOS) of the tip and sample are similar to those at Fermi energy, neglecting their energy dependence one can write:

$$I = I_{el} + I_{inel}, \tag{2.12}$$

where the elastic and inelastic contributions are given by:

$$\begin{aligned} I_{el} = \frac{g_c}{e}\Gamma^L(E_F)\Gamma^R(E_F)\int_{-\inf}^{+\inf} \mathrm{d}E|G^0_{1N}|^2[f_L(E) \\ \times(1-f_R(E)) - f_R(E)(1-f_L(E))], \end{aligned} \tag{2.13}$$

$$\begin{aligned} I_{inel} = \frac{g_c}{e}\Gamma^L(E_F)\Gamma^R(E_F)\sum_\alpha \frac{1}{2}\int_{-\inf}^{+\inf} \mathrm{d}E|G^1_{1N,\alpha}|^2[f_L(E) \\ \times(1-f_R(E-\hbar\omega_\alpha)) - f_R(E)(1-f_L(E-\hbar\omega_\alpha))], \end{aligned} \tag{2.14}$$

where $g_c = 2e^2/h$, Γ^L and Γ^R are twice the imaginary part of the self energy matrices associated with the interaction of the molecular subsystem with the probe and substrate metal continua respectively, $|G^a_{1N,\alpha}|$ is a α degree derivative of the retarded Green's function of the one-electron Hamiltonian, f_L and f_R are Fermi functions of the probe and substrate respectively assumed to be in thermal equilibrium, and ω_α is the frequency of the mode α. This equation describes the essential physics of inelastic transport in the inelastic electron tunneling spectroscopy (IETS) experiment, that is that the inelastic channel opens when the polarization bias is equal to $\hbar\omega_\alpha$ and it stays open for a larger bias. However, it does not point out why in the STM measurements we do not see all the possible vibrational modes.

Only when applying a localized representation of the above formula can we see geometric dependencies [19, 20]. Let us write Γ^L (for Γ^R it's similar) as the matrix of three spaces: A - interacting with the probe, B - the substrate, C - middle atomic orbitals not interacting with either electrode.

$$\Gamma^L = \begin{bmatrix} \Gamma^L_{AA} & \Gamma^L_{AC} & \Gamma^L_{AB} \\ \Gamma^L_{CA} & \Gamma^L_{CC} & \Gamma^L_{CB} \\ \Gamma^L_{BA} & \Gamma^L_{BC} & \Gamma^L_{BB} \end{bmatrix} = \begin{bmatrix} \Gamma^L_{AA} & 0 & 0 \\ 0 & 0 & 0 \\ 0 & 0 & 0 \end{bmatrix}. \tag{2.15}$$

As mentioned previously, the matrix for Γ^R is similar but the only nonzero element is the Γ^R_{BB}. To obtain the conductance $g(E)$ using the above equations we end up with a sum over all the tunneling channels. This leads to the equation for the intensity of the IETS peak W^α due to mode α [20]:

$$W^\alpha = g_c \sum_{\substack{m \in L \\ n \in R}} \Gamma^L_{mm}(E) \Gamma^R_{nn}(E) \frac{1}{2} \left| \frac{\partial G_{mn}(E)}{\partial Q^\alpha} \right|^2 \tag{2.16}$$

Using this model, Troisi and Ratner showed that in the STM IETS experiments [19, 20]:

- Only totally symmetric modes are active if there is only a single tunneling channel.
- The more the vibration is modifying the main tunneling path, the more active is this mode in IETS.
- If a π system is present, then vibrations that modulate the π orbital are active.
- The contribution of out-of-plane modes is important when the tunneling path involves orbitals of σ type on one side and π type on the other side.

2.2 Computational Methods in Nanoscience

Quantum chemistry computational methods are a very important branch of nanoscience. The capability to compute structure and the various properties of atoms, molecules and clusters can in many cases give answers to questions arising during experiments at the nanoscale. In an easy and cost efficient manner we are able to predict e.g. the change of physical and chemical properties while we transform the isolated system through a solution to a solid state. In particular, one can observe isolated and adsorbed molecules, comparing their properties. Also, thanks to the computational methods one can use different results gathered by experimental techniques operating on different scales to interpret the data oat the single molecular level.

Computational chemistry focuses on numerically solving quantum n-body problems which are otherwise analytically impossible to solve. Methods range from ones that are highly precise to very approximate attempts. The bigger the system is, the more approximations must be taken into account to solve the problem. The most accurate are *ab-initio* methods, which are based strictly on first principles. Semi-empirical methods are based on parameters gained from experiments or *ab-initio* simulations, if such values cannot be derived from experimental data. DFT calculations are somewhere in between. The code itself is consistent with *ab-initio* but not all potentials used for calculations are derived strictly from first principles. Therefore, DFT is treated as a separate branch of the calculation methods. All of the above are static methods; they do not involve any time dependence or fluctuations [21].

The first approximation used in quantum chemistry computational methods is the Born-Oppenheimer approximation, which states that because nuclei are much heavier than electrons and thus much slower than electrons we can treat them as static and assume the electrons to be in instantaneous equilibrium with them. In other words, nuclei are reduced to a given source of positive charge. In effect, we get a collection of electrons moving in a fixed potential of the nuclei [21, 22].

2.2.1 Density functional theorem

The main object in the DFT is the total electron density [21–23]:

$$\rho(\vec{r}) = N \int |\Psi(\vec{r}_1, \vec{r}_2, ..., \vec{r}_N)|^2 \mathrm{d}\vec{r}_1, \mathrm{d}\vec{r}_2, ..., \mathrm{d}\vec{r}_N, \tag{2.17}$$

where $\vec{r}$ is a position vector in 3D space, and the integration is done over spatial coordinates of $N-1$ electrons. Therefore, ρ is an object from real space, which has much information about the system. In the position of the molecular core the electron density is the highest, but the gradient has a discontinuity point at the center point. In the simplest Bader approach, it is useful to identify the stationary points of ρ and to calculate for each such point a matrix of second derivatives (Hessian matrix). After diagonalization of the Hessian we know if such a point is a maximum (non core charge attractors), a minimum (i.e. an electron hole), a first order saddle (i.e. middle of a ring), or a second order saddle (chemical bond) of an electron's density ρ [21].

In the basics of the DFT lie two Hohenberg-Kohn theories [21–23]:

- The ground state density uniquely determines the potential and thus all properties of the system, including the many-body wave function.

- There is an energy functional dependent on ρ which has its minimum exactly for ideal the ground state density.

The next mile step for the DFT is the Kohn-Sham theorem in which the authors built the concept of electrons which do not interact with each other but are influenced by unknown potential such that ρ is equal to the ideal ground state electron density. Because those electrons do not interact, it is easy to write their wave functions as a Slater determinant called the Kohn-Sham determinant [21, 22, 24].

In the DFT the total energy (E_{tot}) is a sum of the kinetic energy of not interacting electrons (T_0), the potential energy of interaction between electrons and the atomic core ($\int \nu(\vec{r})\rho(\vec{r})\mathrm{d}\vec{r}$), the energy of Coulomb interactions of ρ with itself ($\vec{J}[\rho]$), and the unknown exchange-correlation energy (E_{xc}) [21, 22, 24]:

$$E_{tot} = T_0 + \int \nu(\vec{r})\rho(\vec{r})\mathrm{d}\vec{r} + \vec{J}[\rho] + E_{xc}[\rho]. \tag{2.18}$$

In order to find the energy minimum, the problem with the unknown E_{xc} must be solved. At this point there are two traditional approaches to the case. The first is the local density approximation (LDA) which assumes that the density can be treated locally as a uniform electron gas, then the exchange correlation energy at each point in the system is the same as that of a uniform electron gas of the same density [22, 24]:

$$E_{xc}^{LDA} = \int \rho(r)\kappa_{ec}(\vec{r})\mathrm{d}\vec{r}, \tag{2.19}$$

here $\kappa_{ec}(\vec{r})$ is the exchange-correlation energy per particle of a uniform electron gas of density ρ.

LDA approximates the energy of the true density by the energy of a local constant density, therefore it fails in situations where the density undergoes rapid changes such as in molecules. This was fixed by considering the gradient of the electron density, the so-called generalized gradient approximation (GGA), in which [22, 25–28]:

$$E_{xc}^{GGA} = E_{xc}[\rho(r), \nabla\rho(\vec{r})]. \tag{2.20}$$

In both approximations the E_{xc} is substituted by a pseudo potential:

$$\nu_{xc} = \frac{\partial E_{xc}}{\partial \rho(\vec{r})}. \tag{2.21}$$

These potentials are either derived from first principles, or derived from experimental data e.g. atomization energies. This determines whether the DFT can be called *ab-initio* or not.

2.2.2 Semi-empirical methods

Most recent semi-empirical methods are based on molecular orbital (MO) theory and employ a minimal basis set for valence electrons. Out of several different types of approximations, neglect of diatomic overlap (NDDO) is the best because it retains the highest multipoles of charge distributions in the two-center interactions. All integrals are done numerically and therefore are approximate to some point, depending on the integral. Semiempirical MO methods are parameterized to reproduce experimental reference data or, possibly, accurate high-level theoretical predictions as substitutes for experimental data. The reference properties are selected such that they are representative for the intended applications. The quality of semiempirical results is strongly influenced by the effort put into the parameterization [29–34].

All of the recently used semiempirical methods are based on the Modified Neglect of Diatomic Overlap (MNDO) method [33, 35–38]. In MNDO molecular orbitals ψ_i and the corresponding orbital energies ϵ_i are obtained from the solution of the secular equations:

$$\psi_i = \sum_{\mu} c_{\mu i}\phi_{\mu}, \tag{2.22}$$

$$0 = \sum_{\nu} (F_{\mu\nu} - \delta_{\mu\nu}\epsilon_i)c_{\nu i}. \tag{2.23}$$

After assigning atomic orbitals (with index μ, ν, λ, σ) to atoms A or B, the NDDO Fock matrix elements $F_{\mu\nu}$ are given as:

$$\begin{aligned} F_{\mu^A\nu^A} = H_{\mu^A\nu^A} &+ \sum_{\lambda^A}\sum_{\sigma^A} P_{\lambda^A\sigma^A}[(\mu^A\nu^A,\lambda^A\sigma^A) - \frac{1}{2}(\mu^A\lambda^A,\nu^A\sigma^A)] \\ &+ \sum_{B}\sum_{\lambda^A}\sum_{\sigma^A} P_{\lambda^B\sigma^B}[(\mu^B\nu^B,\lambda^B\sigma^B), \end{aligned} \tag{2.24}$$

$$F_{\mu^A\nu^B} = H_{\mu^A\nu^B} - \sum_{\lambda^A}\sum_{\sigma^B} P_{\lambda^A\sigma^B}(\mu^A\lambda^A,\nu^B\sigma^B), \tag{2.25}$$

where $H_{\mu\nu}$ are elements of a one-electron core Hamiltonian, $P_{\lambda\sigma}$ is the density matrix and $(\mu\nu, \lambda\sigma)$ are two-electron integrals for the respective atoms A and B. The total energy E_{tot} of a molecule consists of the electronic energy E_{el} and the repulsion E_{AB}^{core} between the cores of atoms A and B:

$$E_{el} = \frac{1}{2} \sum_{\mu} \sum_{\nu} P_{\mu\nu}(H_{\mu\nu} + F_{\mu\nu}), \tag{2.26}$$

$$E_{tot} = E_{el} + \sum_{A} \sum_{B} E_{AB}^{core}. \tag{2.27}$$

Because MNDO includes only one-center and two-center terms, it is rather easy to compute, and therefore very fast. In newer methods there are many corrections for specific interactions like Si-Si, C-H or C=C [33, 34, 36–38], most of which are done to fit the experimental spectroscopic data. At some point, especially for transition metals, the parameters were derived from *ab-initio* calculations because of the lack of experimental data.

The formulas shown above are only the main ones. For a complete description, please refer to one of the review papers [22, 33, 34]. Concluding, both DFT and semi-empirical methods are based on the Hartree-Fock formalism, but the latter is restricted only to valence electrons. Semi-empirical calculations are much faster than the DFT but can be very wrong if the simulated system is different than those for which the parameters were optimized. It is worthwhile to study the optimization process for each used method and not only the final effect. These procedures are shown in the chapter on Methods.

2.3 *Cis* - *Trans* Isomerization

Isomers are molecules which have the same molecular formula, but are built differently. For example, if one considers a molecule built from 3 atoms A, B, and C, the molecular formula would be ABC, but in fact the molecule could be built A-B-C or A-C-B. In many cases even when a molecule is built with the same order of atoms, they can have a different spatial arrangement. Geometry (*cis-trans*) isomerism is one form of the so called stereoisomerism. Because of the different spatial arrangement, isomers differ in many physical and chemical properties arising from the electron density and interactions between functional groups within a molecule [39].

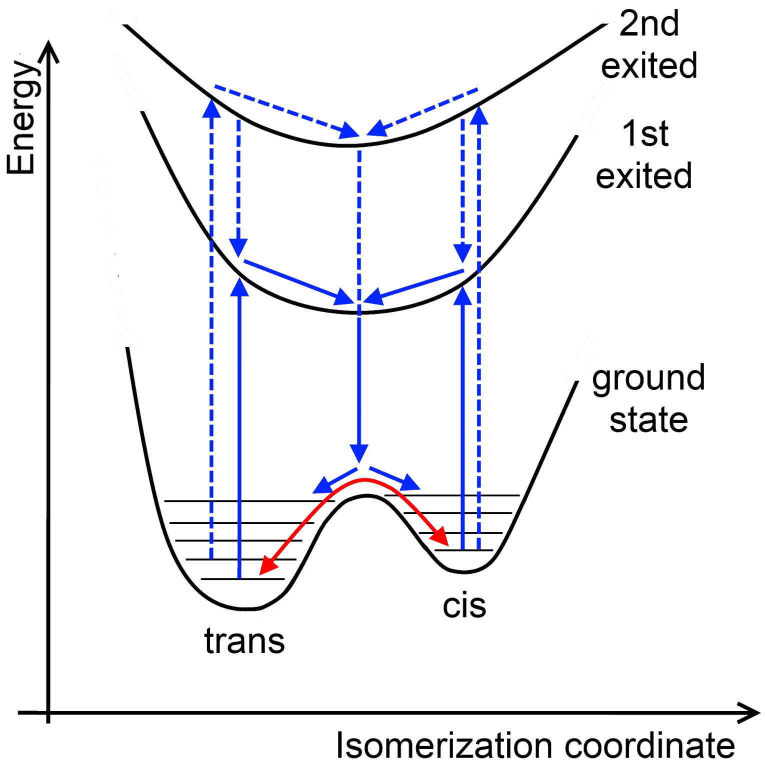

Figure 2.3: Energetic scheme of isomerization processes - In the color blue possible photoisomerization pathways are shown. Isomerization can be transferred by a first, second or any number of higher excited states. In red the adiabatic pathway is presented. Because it is usually heat driven, this pathway usually works in the direction from *cis* to *trans*.

In molecules, rotation around single bonds is usually unrestricted. This means it is a low energy consuming process. Therefore, molecules with single bonds overgo a configurational change and two configurations of the same molecule are not called isomers. A rotation around a double bond, which usually is a π bond, is restricted. This is because after a rotation, p orbitals of both atoms would not overlap anymore and therefore a π bond cannot exist anymore. In this case, rotation is connected with the breaking of a double bond and its new formation in the second conformation. Isomerization is a reaction in which one isomer is transformed into the second isomer. The energy necessary for the reaction may come from any known source e.g. the absorption of electro-magnetic radiation (photoisomerization), heat, the electric field, or inelastic processes with third party electrons [39, 40].

Figure 2.3 shows the schematics of isomerization processes' energetic structure. In general, there are two main pathways of isomerization. The transition through an excited state or an adiabatic transition over vibronic states from one energy minimum to the second one. Usually the transition involving excited states is connected with the absorption of a light photon, and the adiabatic transition is connected with heat. For photoisomerization itself, two different pathways are proposed which depend on the excitation of the $n\pi^\star$ state or $\pi\pi^\star$ state. The earlier leads to an in-plane inversion in at one of the atoms with a double bond and the later leads to a rotation around a double bond [41]. For the adiabatic pathway, because of the differences in activation energy, the transition is directed from the *cis* to *trans*, but on rare occasions when a molecule in the *trans* state is given the exact energy of molecular vibrations it can be transfered to one of the vibronic states and therefore lower the activation energy. In this case a *trans* to the *cis* transition is feasible [40].

Chapter 3

Methods

3.1 The Scanning Tunneling Microscope

The scanning tunneling microscope is an imaging technique capable of producing a real space 3D image of a surface with atomic resolution and, under specific conditions, even subatomic resolution. The STM uses a metallic, atomically sharp tip which is brought very close to the sample allowing the wave functions of the tip and sample to overlap. Typically, a small bias voltage is applied between the tip and sample causing a tunneling current flow. This current is exponentially dependent on the tip-sample distance, therefore STM is a very sensitive technique. The schematic of the STM is shown in Figure 3.1. The position of the tip in all three dimensions is accurately controlled by piezoelectric drivers. In imaging mode, the tip is scanned across the surface, essentially tracing out a shape of sample's surface. One has to keep in mind that the tunneling current (2.10) and tunneling conductivity (2.11) are dependent on the LDOS. This is essential while working with semiconductor surfaces and nanostructures where the LDOS is not constant, and therefore the obtained images will depend on the sign and value of the bias voltage e.g. a hole in the image can be a structure with very low or zero LDOS at a given energy, while a hill on the image could be a flat structure with a very high LDOS at a given energy.

In practice a tungsten chemically etched tip is mounted to the piezo-scanner - typically a piezoceramic tube with 4 outer and one inner electrodes. Applying high voltages up to 300V, the piezo-scanner bends, moving the tip over the sample. The tunneling current is constantly measured, converted to voltage in the I to V converter

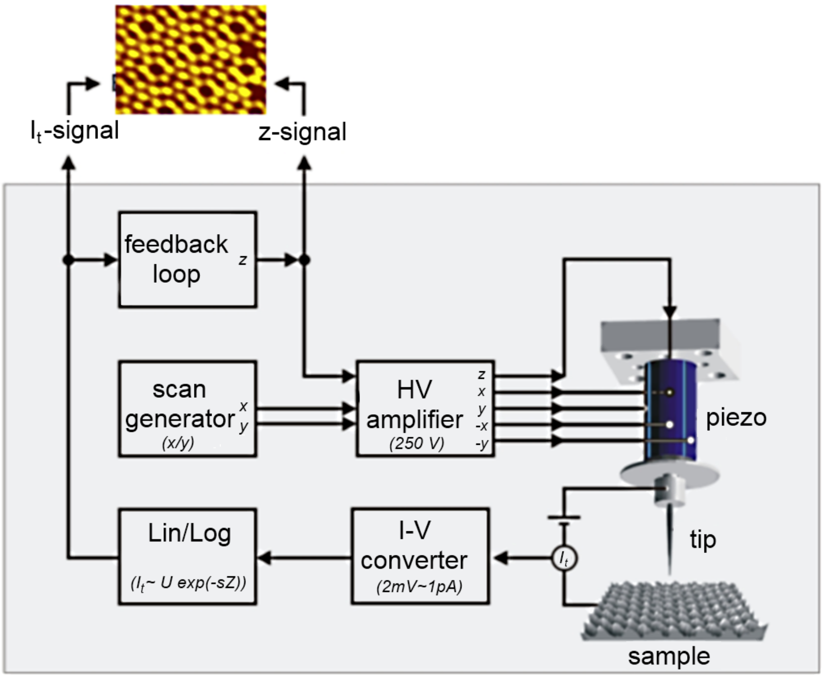

Figure 3.1: Schematics of the STM - Schematic representation of the STM setup including electronics modules.

(IVC), because voltage signals are easier to amplify and send without loss, and finally the signal is registered in the computer. In typical constant current imaging mode, a feedback loop is used to keep a constant value of the tunneling current by modifying the voltage applied to the piezo-scanner in order to correct the tip-sample distance and therefore the tunneling current. In imaging mode, the scan generator produces two separate voltage ramps for x and y which in total build a movement pattern over the sample. The feedback loop and scan generator typically give an output voltage in the range between 0 and 10 V. This is a typical output of a digital-analog converters (DACs) which is used for these tasks. One of the technical aspects of the STM is the quality and resolution of the digital-analog converters, typically on the level of 12 to 24 bits. This combined with the amplification of the voltage in the HV amplifier, piezo tubes dimensions and material, determine the lateral resolution of the STM typically on the level of a few pm. On the other hand the resolution in the z direction due to the comparably smaller piezo-scanners range in this direction does not depend so badly on the quality of the DAC but rather on the noise level of the tunneling junction.

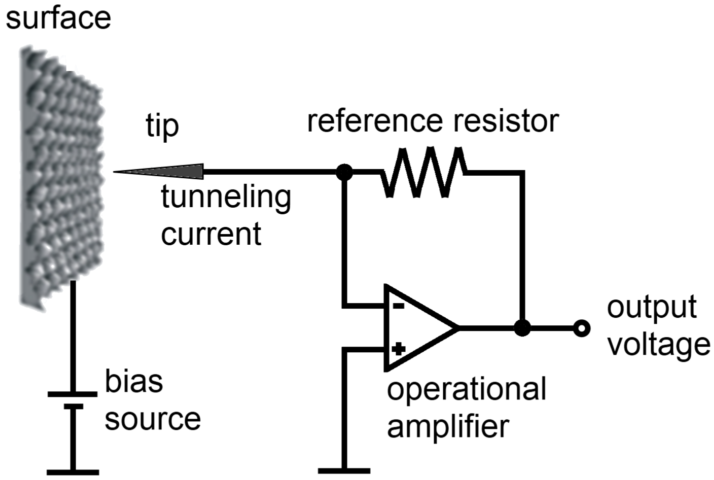

Figure 3.2: Schematics of the I to V converter - A simple IVC converter built from a reference resistor and a low noise operational amplifier, transforms the tunneling current into a voltage signal.

A simple form of the IVC is shown in Figure 3.2. It is built from a low noise operational amplifier and a reference resistor with an impedance (R_{fb}) on the level of 100MΩ. To obtain a maximum signal-to-noise ratio, the bandwidth should be maximized while the noise should be as small as possible. The bandwidth is limited by the resistors' parastatic capacitance and operational amplifiers' bandwidth. The Johnson noise density gives the main noise source for a resistor:

$$n_{R_{fb}} = \sqrt{4k_BTR_{fb}}, \tag{3.1}$$

where k_B is the Boltzman constant and T is the temperature of the resistor. At room temperature (RT) and with a reference resistor $R_{fb} = 100M\Omega$, the voltage noise in $n_{R_{fb}} \times \sqrt{B} = 40\mu V$ (at the typical acquisition bandwidth of STM $B = 1kHz$). This corresponds to a current noise level of 0.4 pA. For a typical experiment where tunneling currents are at the level of several pA or even hundreds of pA, the noise of the IVC is not critical. While analyzing the noise of the whole STM some more details have to be taken into account e.g. the impedances and capacitances of all the wires and especially the connections. While the exact source of noise is hard to point out, the noise itself is easy to measure and characteristic for a specific device and it surroundings.

3.1.1 Scanning tunneling spectroscopy

Because the tunneling current (2.10) and tunneling conductivity (2.11) are dependent on the local density of states, a STM can be used to probe the LDOS with high spacial and energetic resolution. Basing on (2.10) and assuming a featureless density of states (DOS) of the tip, one can write an approximate expression on the tunneling current as:

$$I \propto \int_0^{eV} \rho(E) e^{-2\kappa(E)z} \mathrm{d}E, \tag{3.2}$$

then the derivative of the current equals:

$$\mathrm{d}I/\mathrm{d}V \propto e\rho(eV) e^{-2\kappa(eV)z} \int_0^{eV} \rho(E) \frac{\mathrm{d}}{\mathrm{d}(eV)} e^{-2\kappa(E)z} \mathrm{d}E, \tag{3.3}$$

here $\kappa(E)$ is a the inverse decay length given by:

$$\kappa(E) = \sqrt{\frac{2m}{\hbar^2} \frac{(\phi_{tip} + \phi_{sub})}{2} - E + \frac{eV}{2}}. \tag{3.4}$$

and z is the tip-sample distance. While the current is a sum over all the active tunneling channels, the derivative of the current versus applied bias (V) namely, the differential conductivity measures the LDOS only for a given energy defined as eV.

In the scanning tunneling spectroscopy (STS) mode a tip is placed over a point of interest on the sample, the feedback loop is turned off and the bias is sweeped while the current is registered. There are two ways of obtaining differential conductivity curves, namely, numerical derivation from I-V curves gathered in STS mode, or a direct measurement using a lock-in technique. The latter is better because it is free of numerical artifacts; also it is capable of registering lower signals, and it is free from noise connected with the derivation of noise on the tunneling current signal.

The STS gives information not only about the LDOS but also about the vibrations of an adsorbate on the surface. An inelastic tunneling channel signal is very weak comparing to the elastic channel. The change in the current is almost impossible to notice, therefore in this case only the derivative of the current can be measured, as shown in Figure 3.3.

STS' are gathered using a lock-in technique with a sinusoidal modulation in the range of 300 to 500 Hz superimposed over the bias voltage (see Figure 3.4. Before a lock-in based STS experiment is started, the fast Fourier transform (FFT) of the

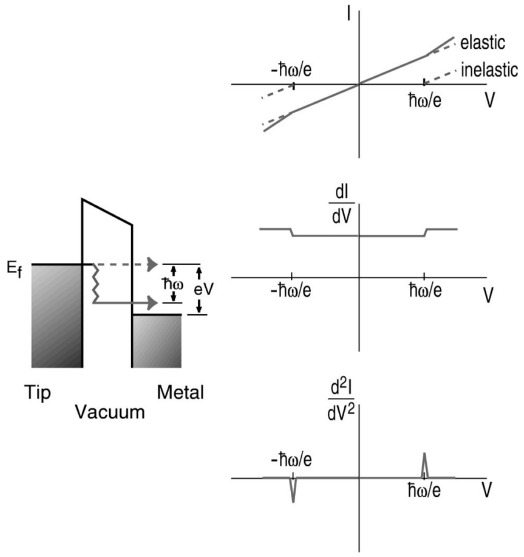

Figure 3.3: Schematic IET signal detection - The small change in the current connected to the inelastic channel can be seen as a step in the first derivative or as a peak in the second derivative of the tunneling current [42].

tunneling current signal is analyzed in order to choose a modulation frequency that differs from the frequencies of any electrical or mechanical vibrations of the system. The applied voltage is modulated with an amplitude in the range of 1 to 20 mV. The lower the amplitude of the modulation is, the sharper peaks are observed in the gathered spectra, but the signal-to-noise ratio is getting worse to the point where the lock-in cannot recognize the tunneling currents modulation any more. The spectroscopy measurement starts by acquiring an STM image. Then, the tip is placed above the point of interest. The feedback loop controlling the distance of the tip to the surface is turned off and the voltage between the tip and the substrate is slowly ramped in the range of interest at a velocity of 0.5 mV$\times s^{-1}$. Both the tunneling current and second derivative of the current gathered by a lock-in amplifier are recorded. After the spectroscopy, the feedback loop is turned on and a control STM image is taken to ensure that the spectroscopy did not alter the molecule. Always there are at least three spectra collected for validation purposes: one on the bare surface, one on the molecule, and another one again on the bare surface.

If the STS mode is used to measure the inelastic electron processes, it is called the IETS [42].

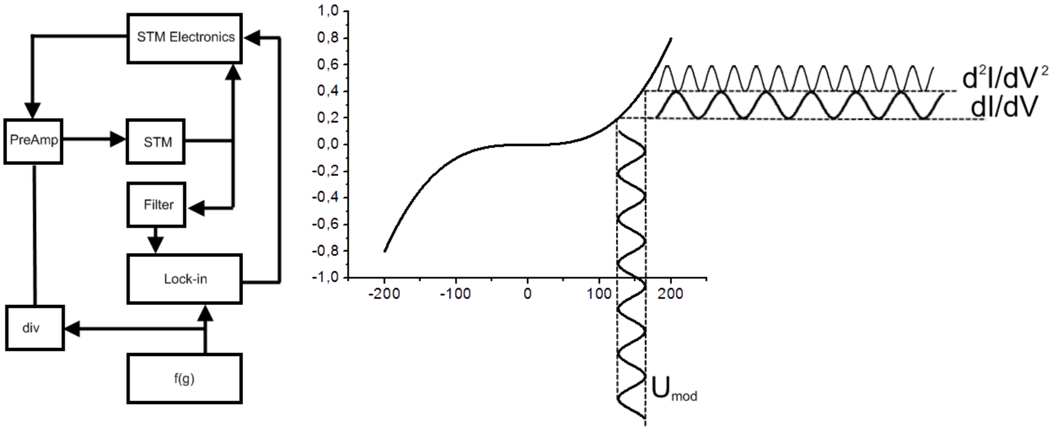

Figure 3.4: Lock-in connection schematics - A function generator gives a reference signal for the lock-in as well as a modulation signal which is weakened to the desired value and summed with the bias voltage. Such a signal is given to the tunneling junction, the response of the tunneling current is not linear and therefore in harmonics it gives information on the value of the derivative of the tunneling current over the bias voltage.

In the post measurement procedure, the surface spectra are scaled to the noise level of the molecule spectra and then subtracted from it. This procedure enables a comparison of spectra gathered at different points causing only minor changes in them. The IETS measurements are restricted to 100 mV, because the efficiency of the signal is for physisorbed molecules too small to be detected at higher energies [43].

3.1.2 Inelastic electron tunneling manipulation

When the inelastic channel of the tunneling current is opened, then the vibrator in the tunneling junction is excited. In this thesis the vibrators are molecules or their parts adsorbed on monocrystaline surfaces. These molecules can afterwards relax in many ways, one of which is isomerization. The inelastic electron tunneling (IET) manipulation procedure [42] is similar to the IETS. It differs in the voltage between the tip and the sample, which in this case is set to a constant value. During the manipulation, the current is measured as a function of time (see Figure 3.5). Changes in the tunneling current indicate that one of a number of possible processes happened. After the manipulation, the feedback loop is turned on and the effect of the manipulation is observed on a subsequent STM image. Integration of the current over the set time gives the number of electrons that tunneled trough the molecule. From this, the yield of the reaction is

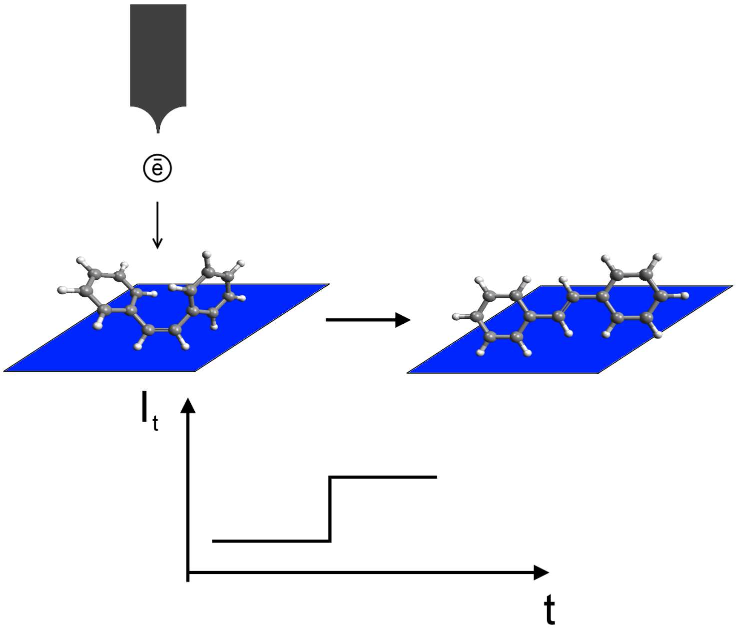

Figure 3.5: Inelastic electron tunneling manipulation - Electrons of the desired energy are injected into the system. The tunneling current is registered and it changes if the molecule undergoes an electron induced process.

calculated. I exposed the molecules to electrons with energies up to 600 meV for time intervals between 0.5 s to 120 s depending on the electron energies. The employed starting currents are smaller than 150 pA. Both IETS and IET manipulation are only performed on molecules that are well separated from surface defects, step edges, and other molecules.

3.1.3 Irradiation of the sample

The irradiation of the sample was carried out *in-situ* in the STM using a 100W mercury lamp. Mercury lamps have a very rich spectra in the range from 250 to 600 nm, thus, fully covering the range of absorption (connected with the *cis* to *trans* isomerization) of 4-anilino-4'-nitroazobenzene. The lamp is mounted outside the UHV system, and its light is directed through a sapphire window and an opening in the cryoshield onto the sample at an angle close to 85° to the surface normal. Figure 3.6 shows the principle of measurement. Before exposure to light, an STM image is taken of a spot with a characteristic feature, e.g. step edges. Then, the STM tip is retracted as far as

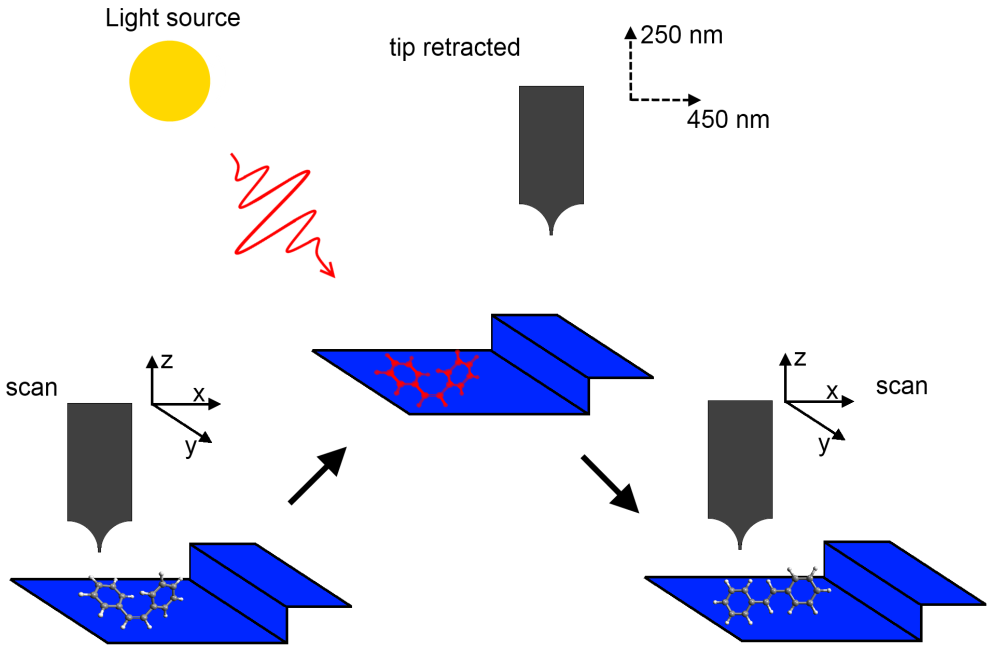

Figure 3.6: In-situ light irradiation - Schematic representation of measurement principles during light irradiation

possible from the sample and the incoming light (around 450 nm horizontally and 250 nm vertically) in order to minimize the shadowing effect of the tip. The same spot is imaged after irradiation as recognized by the characteristic feature.

3.1.4 Local high voltage/high current treatment

Local high voltage/high current treatment starts with establishing a tunneling contact in such a way that the scanner is almost totally elongated (90% of the maximal length). Next the tip is completely retracted and the STM preamplifier is replaced by a resistor. A voltage of 150V is applied between the tip and the sample. Then, the tip is manually approached to the sample while the current is constantly controlled. At the point at which a current of 1 mA is measured, the tip is held for 10 seconds and then retracted within 3 s to 6 s depending on the shape of the tip. After the STM preamplifier has been reconnected, the position of the tip is shifted a few microns away from the contact point and the result of the treatment is measured. A few low voltage pulses on clean spots of the sample are usually necessary to completely recover the tip after the procedure.

3.2 Optical spectroscopy

Although optical methods are in general averaging information on the number of molecules close to the Avogadro number, they are capable of giving a chemical fingerprint of chemical compounds, and information on the electronic structure, especially the highest occupied molecular orbital (HOMO) - lowest unoccupied molecular orbital (LUMO) transitions. The biggest disadvantage of all averaging methods is the incapability of controlling the exact chemical environment of the investigated molecules. In these methods we have a statistical distribution of neighbors and their influence on each other. Optical spectroscopy methods differ in operating energies and mostly the physical process used for probing the molecule. Three main physical processes can be used, namely, absorption, emission and scattering. The infrared spectroscopy (IR) is based on the absorption of IR radiation and the excitation of a molecule to a virtual vibrational level. The Raman spectroscopy is based on the inelastic light scattering, which also involves virtual vibrational levels. Flash photolysis is in fact a variation of ultraviolet-visible (UV-VIS) spectroscopy based on the absorption of light involving excitation to a excited state. Figure 3.7 shows the energetic schematics of all three processes.

3.2.1 Infrared Spectroscopy

At temperatures above 0 K all atoms are in continuous vibration with respect to each other. When the energy of a specific vibration is equal to the energy of the IR radiation directed on the molecule, the molecule absorbs the radiation. The 3D motion of each atom plus 3 possible directions of rotation of a whole molecule give $3n - 6$ fundamental vibrations (so called normal modes of vibration) for each molecule except for linear molecules. In this case, only two directions of rotation are enough to describe all the possible rotations of the molecule, therefore $3n - 5$ fundamental vibrations are possible. Among normal modes those that cause a change in the dipole momentum result in IR activity, while those that cause polarizability changes are Raman active modes. The total number of observed absorption bands is generally different from the total number of normal modes. It is reduced because some modes are not IR active and a single energy can cause more than one mode of motion to occur. Also, additional bands are generated by the appearance of overtones (integral multiples of the

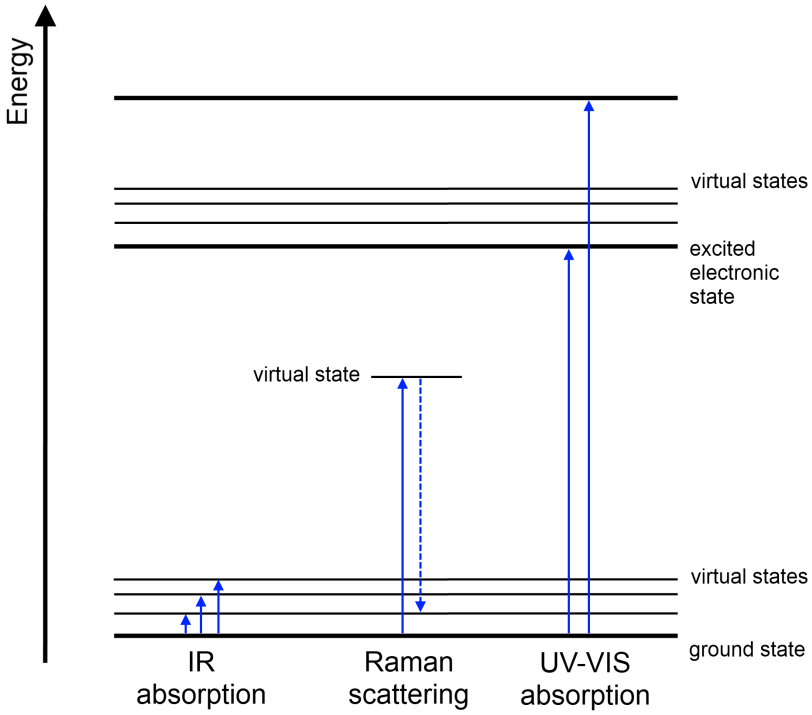

Figure 3.7: Energetic schematics of optical spectroscopies - Energetic transitions underlaying optical spectroscopies. The virtual state is a short-lived distortion of the electron distribution by the electric field of the incident radiation.

normal modes energies), combinations of normal modes energies, differences of normal modes energies, coupling interactions of two normal modes energies, and coupling interactions between fundamental vibrations and overtones or combination bands (Fermi resonance). The intensities of overtone, combination, and difference bands are lower than those of the fundamental bands. The combination and blending of all the factors thus create a unique IR spectrum for each compound [44]. Absorption of IR radiation causes two main types of vibrations, namely, stretching and bending. These vibrations have discreet quantized energy levels, but individual vibrational motions are usually accompanied by other rotational motions. The combination of both leads to adsorption bands rather than discreet lines [44].

The IR spectra are obtained by measuring changes in the absorption or transmittance intensities as a function of energy. Nowadays most IR spectrometers are based on Fourier transform spectrometers, enhancing the measurements' energy resolution.

3.2.2 Raman Spectroscopy

Raman spectroscopy measures the wavelength and intensity of inelastically scattered light from molecules. The Raman scattered light occurs at wavelengths that are shifted from the incident light by the energies of molecular vibrations. If the final vibrational state of the molecule is more energetic than the initial state, then the emitted photon will be shifted to lower energies in order for the total energy of the system to remain balanced. This shift in energy is called a Stokes shift. If the final vibrational state is less energetic than the initial state, then the emitted photon will be shifted to higher energies, and this is called an Anti-Stokes shift. The mechanism of Raman scattering is different from that of infrared absorption, so Raman and IR spectra provide complementary information. Typical applications are in structure determination, multicomponent qualitative analysis, and quantitative analysis.

The Raman scattering transition moment is:

$$R =< X_i|a|X_j >, \tag{3.5}$$

where X_i and X_j are the initial and final states, respectively and a is the polarizability of the molecule:

$$a = a_0 + (r - r_e)\frac{\mathrm{d}a}{\mathrm{d}r} + ..., \tag{3.6}$$

where r is the distance between atoms and a_0 is the polarizability at the equilibrium bond length (r_e). Polarizability can be defined as the ease of which an electron cloud can be distorted by an external electric field. Since a_0 is constant and $< X_i|X_j >= 0$, R simplifies to:

$$R =< X_i|(r - r_e)\frac{\mathrm{d}a}{\mathrm{d}r}|X_j >, \tag{3.7}$$

As a consequence there must be a change in polarizability during the vibration for that vibration to inelastically scatter radiation.

The polarizability depends on how tightly the electrons are bound to the nuclei. In the symmetric stretch the strength of electron binding is different between the minimum and maximum internuclear distances. Therefore, the polarizability changes during the vibration and this vibrational mode is active in the Raman spectroscopy. In the asymmetric stretch the electrons are more easily polarized in the bond that expands but are less easily polarized in the bond that compresses. There is no overall change in polarizability and therefore the asymmetric stretch is Raman inactive.

The Raman line intensities are proportional to:

$$I_R \propto IC\nu^4\sigma(\nu)\exp\frac{-E_i}{kT}, \tag{3.8}$$

where I is the radiation intensity, C is the concentration, ν is the frequency of the incident radiation, $\sigma(\nu)$ is the Raman cross section (typically 10^{-29} cm^2), and $\exp\frac{-E_i}{kT}$ is the Boltzmann factor for state i.

Usually Anti-Stokes lines have higher intensity and therefore they are used for most measurements. A laser is usually used as the light source. In modern Raman systems, a confocal microscope is applied to deliver the light from the laser to the sample and to gather the scattered light. A set of filters cuts the Rayleigh line and enables the detection of lines as close as 50 cm^{-1} from the Rayleigh line. CCD detectors are usually used for quantitative investigations.

3.2.3 Flash Photolysis

Chemical reactions proceed often through a sequence of instable intermediates like excited molecules, molecular fragments, or ionised molecules, before a stable end product is formed. In the case of isomerization which is the topic of this thesis the only important intermediates are excited molecules. The lifetimes of excited molecules are usually very short, on the level of piko- or nanoseconds. Therefore, they cannot be extracted and analyzed, but they can be investigated during the photochemical reaction by flash photolysis, a method developed by G. Porter and R.G.W. Norrish [45, 46].

Figure 3.8 depicts the experimental principles. Light from a pulse laser is focused onto a probe and causes a relatively high concentration of optically excited molecules. A set-up for adsorption analysis is working, constantly monitoring changes in absorption spectra at a chosen wavelength, recorded using a very fast detector. A computer is recording signals after a laser pulse. The excited molecules are unstable and decay either to a lower excited state, undergo an intersystem transition from a singlet to triplet state or undergo an isomerization reaction. The absorption spectra is different for each of such states and monitoring it one is able to conclude on the reactions stages.

First an UV-VIS spectrum is gathered before a flash photolysis experiment. To begin this, information about the absorption of light is essential to choose a proper light source. Next, if the spectra from before the experiment and the one made after the whole series of time dependent measurements are the same, then we are sure that

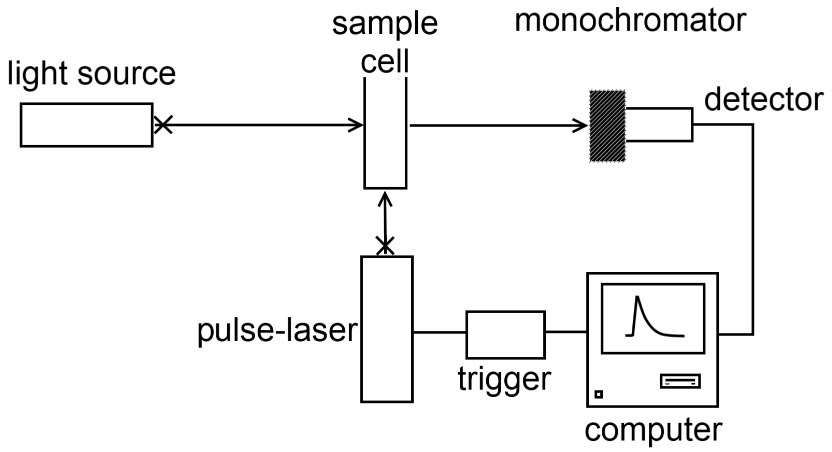

Figure 3.8: Flash photolysis experimental set-up - Schematic representation of the experimental set-up. A light source, monochromator and detector are used for detection of absorbance, while a pulse-laser is used to excite molecules in the sample cell. The laser pulse is triggered by a computer which at the same time starts the acquisition of data.

molecules were not destroyed during the experiment. Following this, a light source is chosen to fit the desired energetic transition and a series of experiments is conducted. Each of the experiments is done with the detection of changes taking place on a designated absorption line.

The change of absorbance in time can be described as:

$$\ln(A_\infty - A_t) = -kt + \ln(A_\infty - A_0), \tag{3.9}$$

here k is the kinetic constant of the reaction, A_∞ is the absorbance before the experiment, A_t is the absorbance during the experiment, and A_0 is the absorbance just after the laser pulse. From k we can conclude if the reaction involves direct transition between singlet states, or an intersystem transition to a triplet. The faster the isomerization reaction is in solutions, the more probable that on surfaces this reaction will occur at all, with many other possible relaxation processes involving energy transfers with the surface [45, 46].

3.3 Computer Simulations

For the best accuracy and purity of calculations the *ab-initio* methods should be used. However, in practice *ab-initio* methods can be effectively used only for very small systems as the computational costs increase drastically with the complexity of the simulated system. DFT can cover much bigger systems but usually using periodicity boundaries in all three dimensions. Semi-empirical methods are used for big (as big as 5000 atoms) isolated systems. Therefore in this thesis the DFT methods and semi-empirical methods were used.

There are two main tasks for software using DFT or semi-empirical codes, namely, single point energy and geometry optimization. The first is used to obtain information on the energy of formation, the energy of adsorption, molecular orbitals or density of states. The user assumes a certain arrangement of atoms in 3D space, and the program calculates the energy for such a system. Both the DFT and semi-empirical methods are self consistent field (SCF) methods, that is, an effective potential from atomic cores (and core electrons for semi-empirical methods) is assumed, the equations are solved for such potential and if it is good, then the assumed potential is the result, whilst if not, the potential is changed and the next iteration starts. Usually 20 to a 1000 iterations are necessary for the SCF to be self-consistent. These potentials are then used for calculations of various physical and chemical properties. The geometry optimization starts just as the single point energy operation, but after the SCF self-consistency is achieved, the configuration of the atoms' arrangement is varied according to one of many algorithms and the single point energy operation is conducted again. The achieved total energies are then compared. The configuration of atoms which has the lowest total energy is the result of such an operation. Figure 3.9 shows a diagram of the calculation procedure.

Throughout the thesis three programs were used: ArgusLab for semi-empirical calculations, Abinit for DFT calculations of a free molecule and Fireball for DFT calculations of molecules adsorbed at the silicon surface. Semi-empirical methods are very useful in the case of physisorption, as the pseudopotentials used in the DFT codes cannot reconstruct the physisorption of molecules.

3.3.1 ArgusLab

ArgusLab is a freely licensed molecular modeling, graphics, and drug design program [47]. It has a few useful functions implemented such as Austin Model 1 (AM1), Parametric Method Number 3 (PM3) codes with point energy and geometry optimization calculations. The PM3 code is especially useful as it is quite accurate for

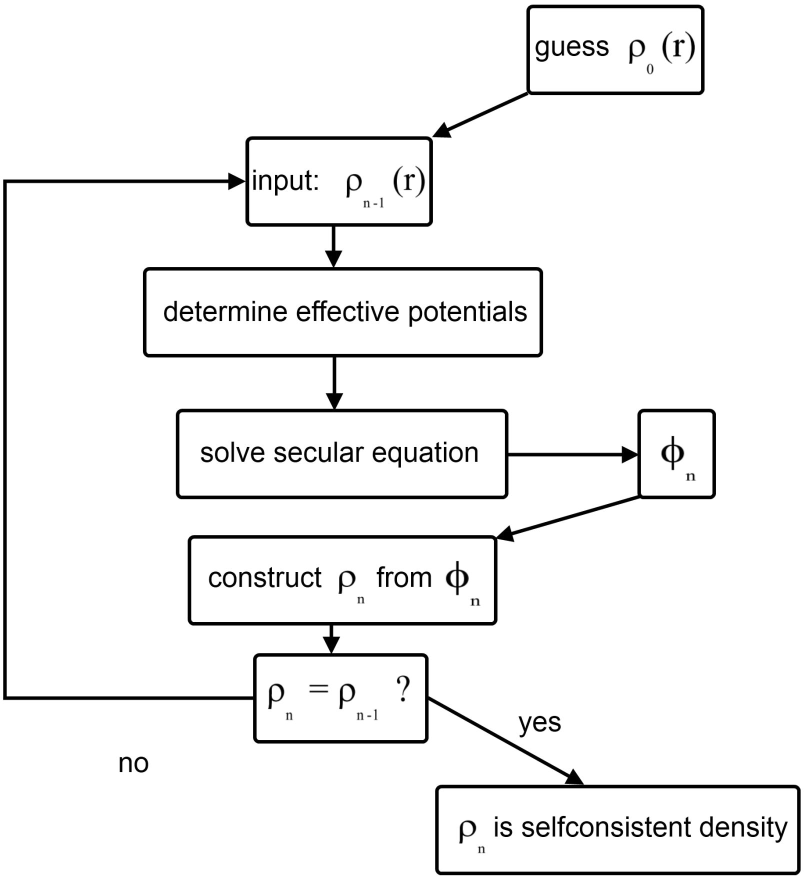

Figure 3.9: SCF iterations - Schematic representation of n-th iteration.

azobenzene derivatives and provides an electrostatic potential (ESP) mapped onto isoelectron density. For physisorbed molecules which are imaged at low bias voltages far from HOMO or LUMO, ESP maps give quite a nice resemblance of STM images. This is because a physisorbed molecule out of definition should not change the LDOS of the surface. Therefore, a physisorbed molecule should be fairly transparent for the tunneling electrons as long as the bias voltage lies within the HOMO-LUMO gap. Thus, the only effects of the molecule are to change the dielectricity as compared to vacuum dielectricity and to provide an inelastic tunneling channel. The inelastic tunneling channel is too small to be seen in the imaging mode of the STM. On the contrary, a large dielectric constant means that the dielectricum is easily polarisable, i.e. its charges are easily displaced. The electrophilic reactivity of the molecule also depends on the displacement of electrons (towards the other reactant). Thus, regions with high negative density in ESP, where the reactivity is high, correspond to a large dielectric constant. In fact, from a point of view of the ESP maps, a molecule can be regarded as an inhomogeneous dielectricum. Its apparent height is larger for more negative ESP. The most outer contour of the ESP is of interest, because in the STM experiments the tip is at a distance of around 1 nm from the surface [48].

3.3.2 ABINIT

ABINIT is a DFT package using pseudopotentials and a planewave basis capable of finding the total energy, charge density and electronic structure. Moreover, it can be used for a geometry optimization according to DFT forces and stresses. In this thesis the ABINIT package was used under the GGA approximation using pseudopotentials from the FHI code to determine the geometry, and a reference electronic structure of isolated molecules for further calculations. Although precise and easy to use, ABINIT was computationally too expensive for the DFT calculations of adsorbed molecules. Therefore, a more approximate method was tuned to the ABINIT calculations in order to calculate bigger systems.

3.3.3 Fireball

Fireball is a Tight-Binding DFT code which has a balanced accuracy and efficiency. It cuts off atomic potentials at certain distances which are defined by the user. Therefore, each potential has to be tested before it can be used for further calculations. The advantage of such an approach is the efficiency in calculations. This code is capable of handling a system as big as a thousand atoms. The potentials used for calculations were tested against VASP calculations of a clean silicon (4x2) surface and ABINIT calculations of isolated molecules in the *cis* and *trans* conformation.

Chapter 4

Experimental Setups

4.1 Room Temperature Ultra-high Vacuum Chamber

In order to fully characterize silicon (001) and metal surfaces, a new ultra-high vacuum (UHV) chamber had to be built. A system set-up I have designed and built is based on several principles:

- a three stage sample introduction system,
- the separation of preparation and analysis chambers,
- ultimate pressure in the analysis chamber,
- compatibility with organic molecules experiments.

Figures 4.1 and 4.2 show the new experimental set-up with some main features pointed out. Technical drawings of the chambers are placed in Appendix 1. When talking about the UHV system it's more convenient to say what can be done using it, than how it's built. Therefore, there are 3 main aspects of UHV systems: analysis capabilities, preparation capabilities and the pumping system (ultimate achievable pressure).

4.1.1 Analysis

The main analysis tool is the Omicron UHV RT STM/AFM hybrid. The STM is suspended on springs with an eddy-current damping system. It is heavy and therefore mechanically stable. The electronics are quite old but using low-pass filters and some star-like grounding with very thick cables, measurements at a 5 pA tunneling current

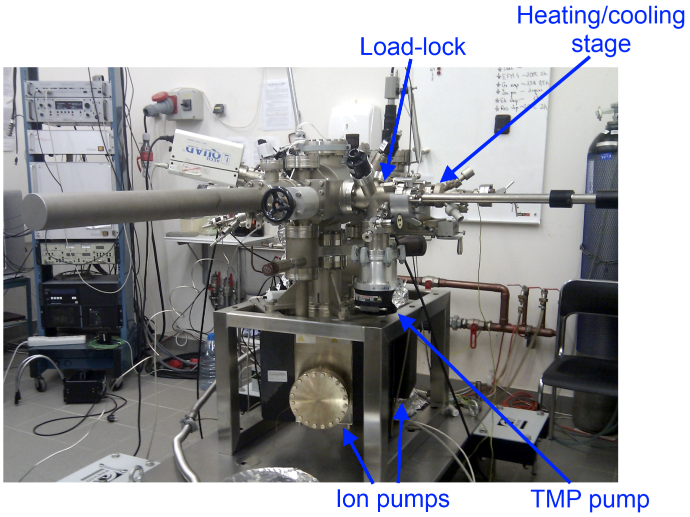

Figure 4.1: Photography of RT UHV system - front view - Marked on picture: load-lock, heating/cooling stage and pumping system.

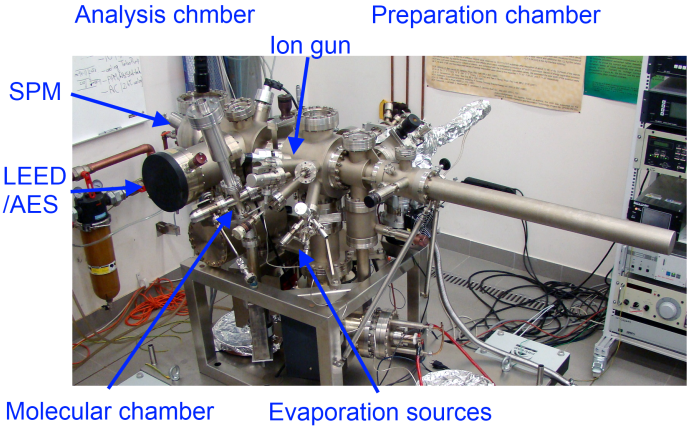

Figure 4.2: Photography of RT UHV system - back view - Marked on picture: analysis, preparation and molecular chambers, SPM head, LEED/AES spectroscope, evaporation sources, heating/cooling and ion gun.

are possible. In this microscope the scanner is on the sample side. In effect only lower scanning speeds are feasible, on the level of 1-3 Hz per line. The second analytic tool is the OCI LEED/AES spectrometer. It is used to determine the surface reconstruction and cleanliness of the sample. The mass-spectrometer is used for control of residual gases in a UHV system as well as for control of the molecules' purity during their degas and evaporation. Four cold-cathode gauges are used for continuous pressure control in every chamber of the system.

4.1.2 Preparation

Samples are introduced into the vacuum system via a load-lock chamber. Afterwards, the samples are placed in a heating/cooling stage for thermal preparation. The samples can be cooled down by a liquid nitrogen cold finger to 100K and heated up to over 1600K by means of a direct current treatment, electron beam or by a sample stage heater. An ion gun, and 3 evaporation sources are directed at the center of the preparation chamber. The heating/cooling stage can be used to adjust the position of the sample so that it is in the right position. Therefore, evaporation on the cooled or heated samples is feasible. Two evaporation sources are electron beam sources (one Omicron EFM-4 and one home-built) and one slot is dedicated for a molecular chamber. The molecular chamber is mounted through a gate valve. It has a separate pumping system based on a turbo pump, a home-built evaporation source and a dedicated mass spectrometer.

4.1.3 Pumping system

A Varian rotary pump is used as a fore pump. It is connected either to the turbo pump in a load-lock or to the turbo pump in the molecular chamber. The turbo pump installed in the load-lock is used as a main turbo pump during the initial pump down. The desired pressure of the initial pumping of the system is on the level of $1 \cdot 10^{-7}$ mbar. At this point baking of the chamber starts at a temperature of 400K for at least 48 h. The bake out is carried out in a tent using two integrated heaters and an electronic system for the temperature control. We use a 2 stage control, one for a precise control of the temperature by adjusting the power of the heaters and a second emergency stage which cuts the power to the main bake out control unit in case of a serious overheat. After the pump down, the vacuum is generated and maintained by two ion pumps: one mounted (100 l/s Diod) under the analysis chamber and one (300 l/s Nobel Diod) under the preparation chamber. A titanium sublimation pump (TSP) with a cryo shield can be mounted in either of the chambers, usually in the preparation chamber. Technical details are in Appendix 1. The base pressure in both chambers oscillates around $2.5 \cdot 10^{-10}$ mbar.

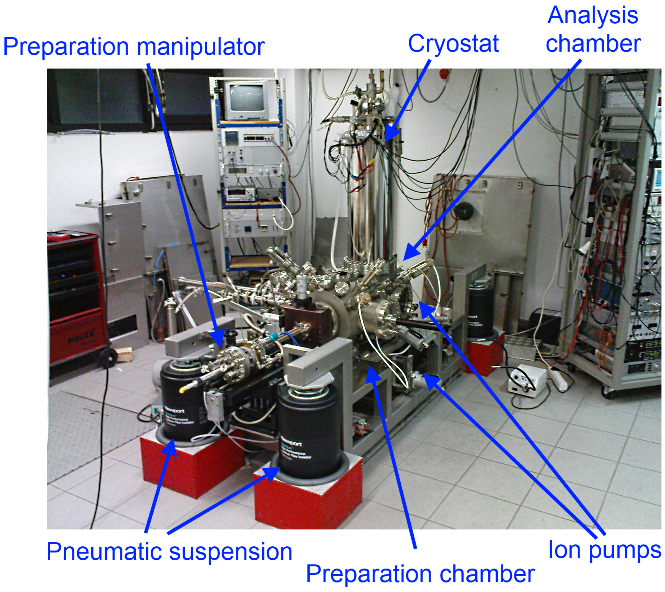

Figure 4.3: Photography of the LT UHV system - front view - Marked on picture: analysis and preparation chambers, the heating/cooling manipulator, ion pumps, cryostat, and the pneumatic suspension.

4.2 Low Temperature Ultra-high Vacuum Chamber

In order to perform single molecule experiments, a low temperature (LT) UHV STM was necessary. Because at the Institute of Physics we do not possess such a system I made my low temperature measurements the laboratory of prof. Karina Morgensters from ATMOS, Leibniz University Hannover, Germany.

4.2.1 Analysis

This system is equipped with a Createc LT UHV STM. The microscope is mounted in a separate chamber with a liquid helium cryostat. The noise level on this system enables measurement on metallic substrates with tunneling currents as low as 2 pA, and 6 pA on a silicon substrate. The z direction stability is on the level of 5-7 pm and the thermal drift is lower than 1 nm·h^{-1}. The helium based cryostat guarantees temperatures of the sample lower than 6K at all times. A Zener diode enabled counter heating of the STM stage, also enabling variable temperature operations. A sapphire window in the chamber enables *in-situ* sample irradiation. The system is equipped with

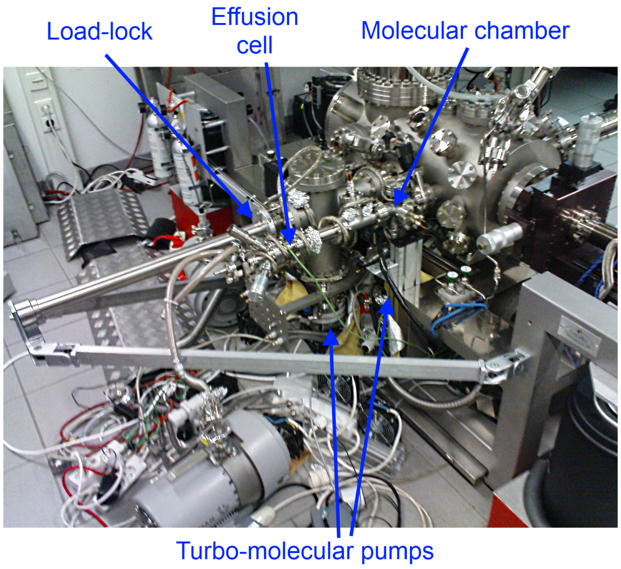

Figure 4.4: Photography of LT UHV system - back view - Marked on picture: the load-lock, molecular chamber, effusion cell, and turbo-molecular pumps.

two mass spectrometers, one mounted in the molecular chamber used for control of the molecules' purity and one in preparation chamber for the residual gas analysis. The whole system is standing on 4 pneumatic legs, which provide damping of any external vibrations.

4.2.2 Preparation

Samples are introduced through a load-lock chamber and placed in a manipulator with heating and cooling capabilities. The highest achievable temperature by direct current heating is 1500 K, while the lowest possible with liquid helium cooling is lower than 25 K. The manipulator has 4 degrees of freedom and therefore a sample can be placed in front of an electron beam for heating, ion gun for cleaning, hydrogen gun for modification or in front of a molecular chamber. The molecular chamber is similar to the one in Poznan. It is mounted via a gate valve, it has its own pumping system based on a turbo-molecular pump, cold cathode gauge for pressure control and q mass spectrometer for molecule cleansing control. A commercial effusion cell is mounted in front of the valve.

4.2.3 Pumping system

Two Varian scroll pumps are used as fore pumps. They are connected to the turbo-molecular pump in the load-lock and to the turbo-molecular pump in the molecular chamber. The turbo-molecular pump installed in the load-lock is used as a main turbo pump during the initial pump down. The desired pressure of the initial pumping of the system is at the level of $5 \cdot 10^{-7}$ mbar. At this point, baking of the chamber starts at a temperature of 390K for at least 48 h. The bake out is carried on in the heating box using several integrated heaters and an electronic system for the temperature control. After the pump down, the vacuum is generated and maintained by two ion pumps: one mounted (120 l/s Diod) under the analysis chamber, and the second one (300 l/s Nobel Diod) under the preparation chamber. A TSP with a cryo shield is mounted in the preparation chamber. The base pressure in the preparation chamber oscillates around $7.5 \cdot 10^{-10}$ mbar and in the analysis chamber around $5 \cdot 10^{-10}$ mbar. For a short period of time with the TSP and manipulator cooled down, a pressure below $1 \cdot 10^{-10}$ mbar can be achieved. Inside the cryosheld of the STM, a pressure below $1 \cdot 10^{-11}$ mbar is guaranteed thanks to the freezing of all the residual gases on the walls of the shield and cryostat.

Chapter 5

Materials

5.1 Monocrystalline Substrates

5.1.1 Copper(111)

Copper is a metal from group 11 (the same as gold and silver). It crystallizes in a faced-centreed cubic (fcc) lattice. In terms of electronic structure it has s-orbital electrons on top of a filled d-orbital. Contrary to the gold or silver (metals from the same group), copper is chemically reactive. Its (111) surface has a 3-fold symmetry (apparently 6-fold, hexagonal), which causes the most packed configuration of atoms in fcc crystals. Copper does not show any surface reconstructions but a surface relaxation, which means that the distance between the first and the second layer is a little smaller than the bulk one and the distance between second and third layer is a little bigger. Figure 5.1 shows the STM image of the Cu(111) surface atomic structure. Apart from the atomic structure electron density standing waves are visible. These waves have their origin in surface defects, adsorbed molecules like CO or H_2O or finally in step edges.

The Cu(111) surface has a surface state at -435 meV from the Fermi level which exists in the gap along the gamma-L line in the bulk band gap. This surface state constitutes a quasi-two dimensional (2D) nearly-free electron gas with around 0.04 electrons per surface atom. This surface state makes a big contribution to the chemical reactivity of the Cu(111) surface. Figure 5.2 shows the LDOS structure of the copper(111) surface which is dominated by the d-band with a lower density near the Fermi level consisting of the s-band.

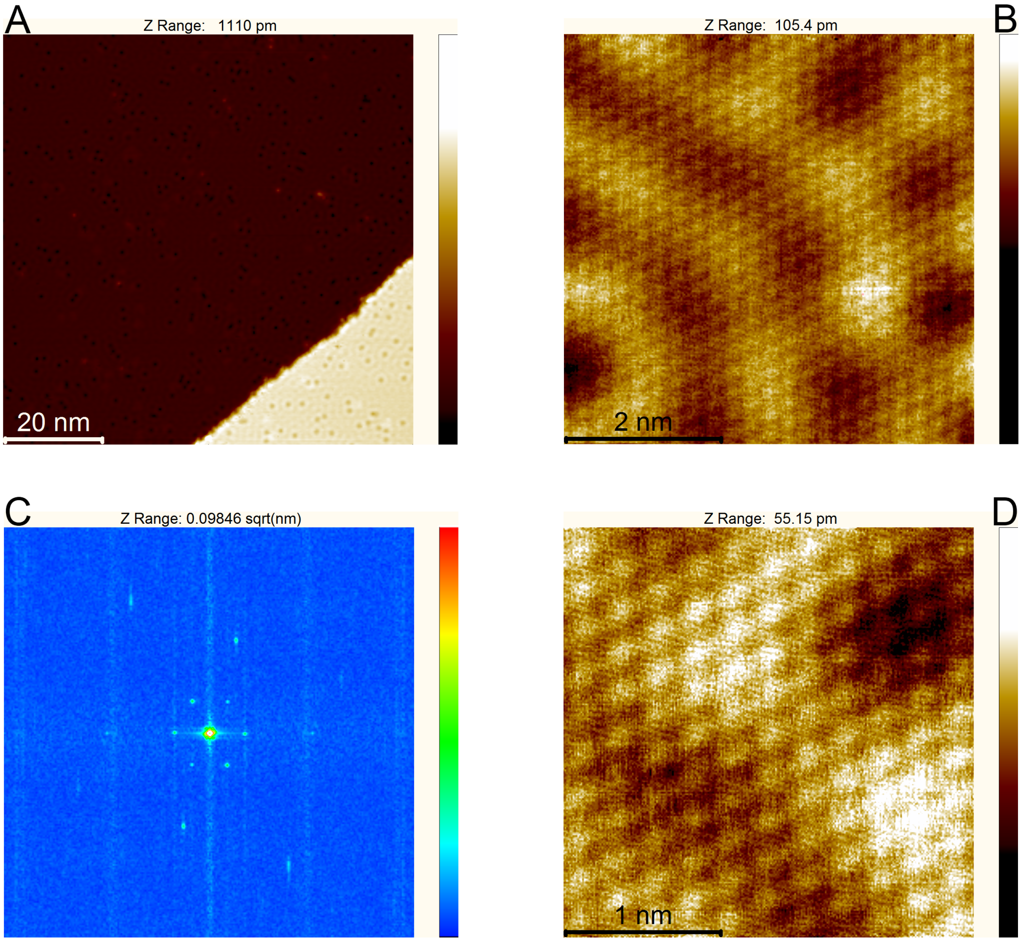

Figure 5.1: STM images clean Cu(111) surface - A - Cu(111) surface, dark dots represent adsorbed CO molecules, B - clean surface, apart from the atomic resolution standing waves pattern is being visible, C - FFT of image B, hexagonal lattice is represented by first order points, D - atomic resolution image of Cu(111) surface. Tunneling parameters: A - I_t=59 pA, U_t=50 mV, B - I_t=7.4 nA, U_t=5 mV, D - I_t=7.4 nA, U_t=5 mV

In UHV conditions Cu(111) monocrystal is easily cleaned by sputtering and annealing cycles. A monocrystal is exposed to a noble gas ion beam at energies about 1 keV for at least an hour and afterward annealed at 950 K for a time equal to the sputtering time. When the crystal is introduced to the UHV system, several cycles are needed to obtain a clean, atomically flat surface. Afterwards, if the system was not vented in the meantime, usually one cycle is enough.

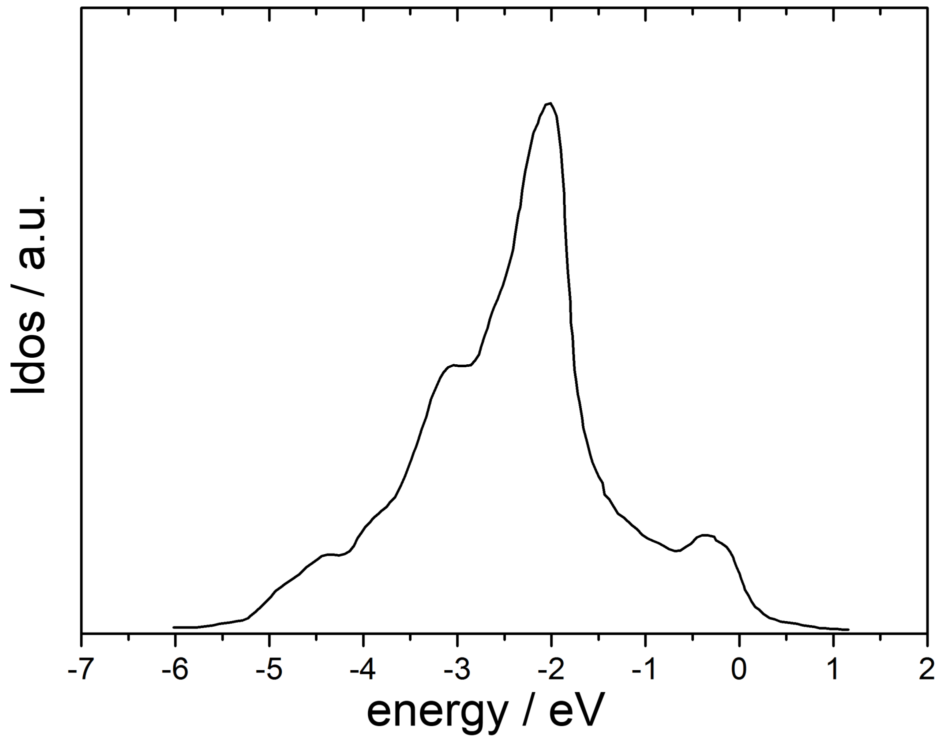

Figure 5.2: LDOS of the Cu(111) surface - local density of states (LDOS) measured by means of photoemission spectroscopy [49].

5.1.2 Silicon(100)

Silicone is a semiconductor with a bulk band gap of 1.14 eV. It has many phases from crystal to the amorphous, each having its applications in industry. Crystalline silicon has a diamond like structure. Si and especially its (100) surface (100 is the same as 010 or 001 in this case) is a material of major technological importance since it forms the basis of many electronic devices such as transistors, microprocessors or photovoltaic cells. Most new electronic devices tend to be incorporated into silicon technology and therefore silicon will be used in such new technologies as atomic scale devices, ultra dense storage devices, quantum computers, or last but certainly not least important molecular electronic devices. The silicon surfaces are the most extensively studied semiconductor surfaces and there are several known surface reconstructions specific for each silicon surface.

The (100) surface shows 3 surface reconstructions: (2x1), p(2x2) and c(4x2). For

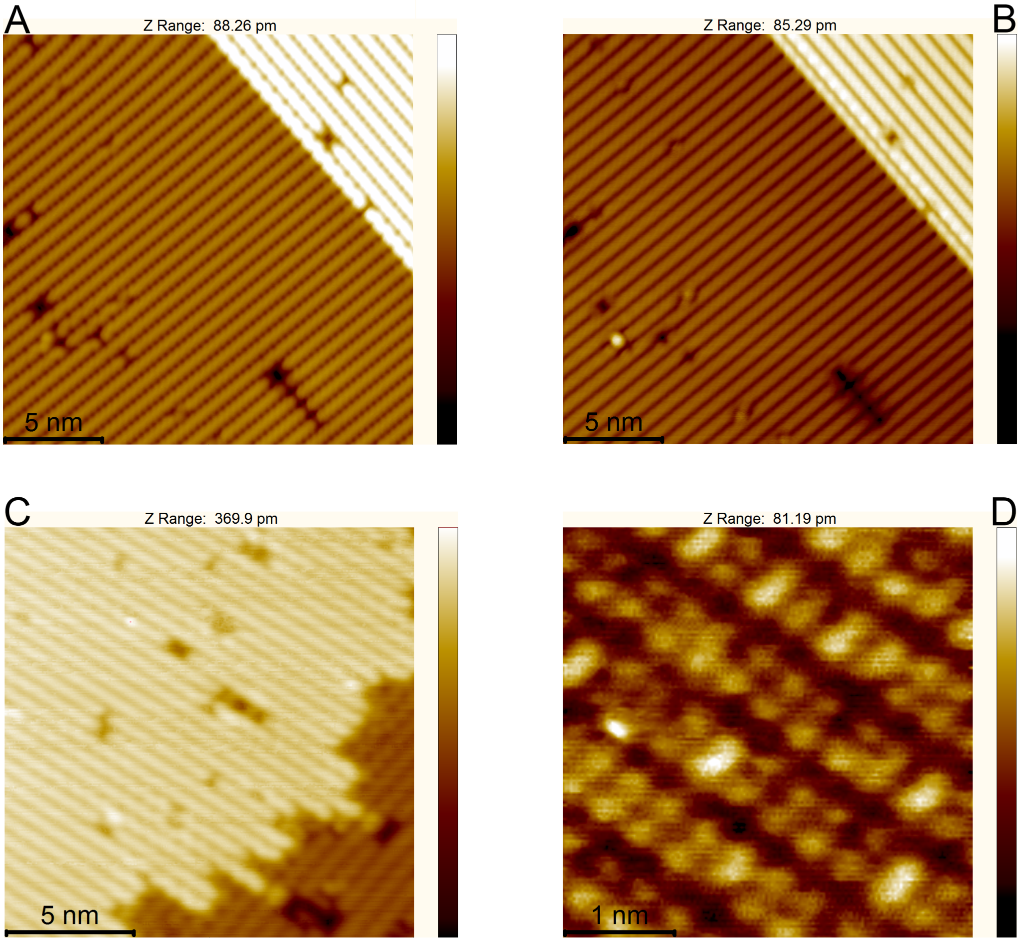

Figure 5.3: STM images of clean Si(100) surface - A - Si(100) surface, occupied states image at 5 K, B - unoccupied states image at 5 K, C - unoccupied states image at RT, D - atomic resolution image of Si(100) surface at RT presenting the 2×1 reconstruction due to flip-flop motion. Tunneling parameters: A - I_t=159 pA, U_t=-2.2 V, B - I_t=159 pA, U_t=2.2 V, C - I_t=40 pA, U_t=-2.5 V, D - I_t=89 pA, U_t=2.2 V,

each of the two types of doping different reconstruction is the ground state one. Namely, for n-type p(2x2) is the ground state, while for p-type the c(4x2) is the ground state. The (2x1) is an apparent reconstruction which is the effect of the so called flip-flop phenomena. At RT the (2x1) reconstruction is the dominant one as the thermal energy is inducing the flip-flop effect. Only at a near proximity of defects or adsorption sites are c(4x2) or p(2x2) observed. At LT the flip-flop is believed to be frozen and the (2x1) reconstruction is improbable. Two groups [50, 51] have reported a reemergence of the

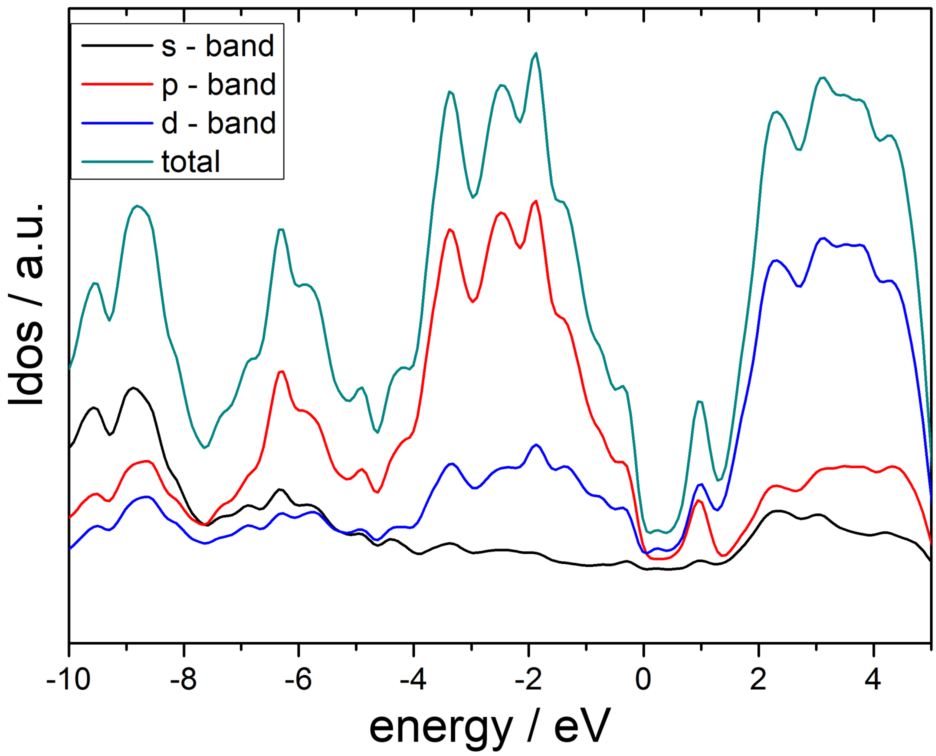

Figure 5.4: Calculated LDOS of Si(100) surface - The calculated LDOS is projected onto surface atoms, and curves from different bands show that near Fermi level the p-band is the dominant one.

(2x1) symmetric dimers at 10 K and each interpreted the result differently. Yokoyama and Takayanagi [50] argued that the reemergence of the (2x1) symmetric dimers is due to an anomalous flip-flop motion. In contrast, Kondo et al. [51] claimed that the (2x1) symmetric dimers at 10 K are static and posed a question regarding the ground state [52]. A very systematic study for different substrate types, temperatures and tunneling conditions made by Hata et al. show that at temperatures below 40 K the (2x1) reconstruction is induced by a strong interaction of the scanning tip with the substrate [52]. At higher temperatures (around 80 K) this effect can be seen only at extremely high tunneling currents [52]. This kind of strong interaction is caused by a very strong decrease in substrate conductance at the LT and therefore a close proximity of the tip with the surface. Therefore all images made at the LT show mainly (2x1) surface reconstruction. Figure 5.5 shows STS spectra obtained at 6 K and at RT of

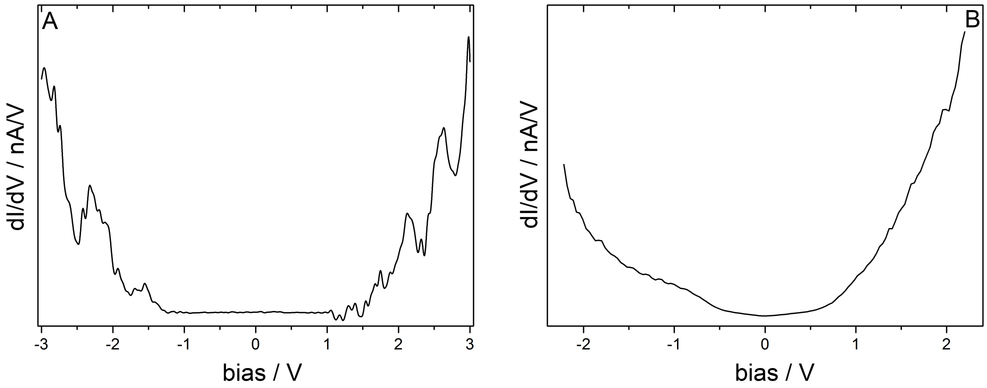

Figure 5.5: STS of Si(100) at LT and RT - A - spectroscopy gathered at 6 K, data resolution 1mV, smoothed for clarity, the lock-in parameters:f=479Hz, A=2mV, t=30ms, B - spectroscopy gathered at RT, the curve calculated out of I-V curves, averaged over 10000 measurements.

two pieces of the same Si(100) p-type with a resistivity of 0.01 $\Omega \cdot$ cm. These curves show clearly that at LT the low conductivity of substrate causes an apparent bigger energy gap, because electrons from surface states cannot relax further into the bulk of the silicone.

Due to the surface reconstruction the electronic structure of the Si(100) surface is much more complex. Firstly, the calculated LDOS does not present any gap near the Fermi level (see Figure 5.4). The p-band is the dominant one at the surface at the occupied states while the d-band is dominant in the unoccupied states. The s-band is almost invisible in the occupied states and nearly negligible in the unoccupied states. There are surface states localized strictly on the silicon dimers. Such differences in the dominance of bands for occupied and unoccupied states causes very different STM images of adsorbates at this surface at different signs of polarization voltage.

5.2 4-anilino-4'nitroazobenzene

Azobenzene and its derivatives has attracted much attention due to its potential applications in optoelectronic and molecular nanoelectronic devices. First, I will show the main physical and chemical properties of azobenzene and its derivatives, then I will give a review of the state of the art, and finally I will point out what is missing in the understanding of the topic and what I have done to solve this.

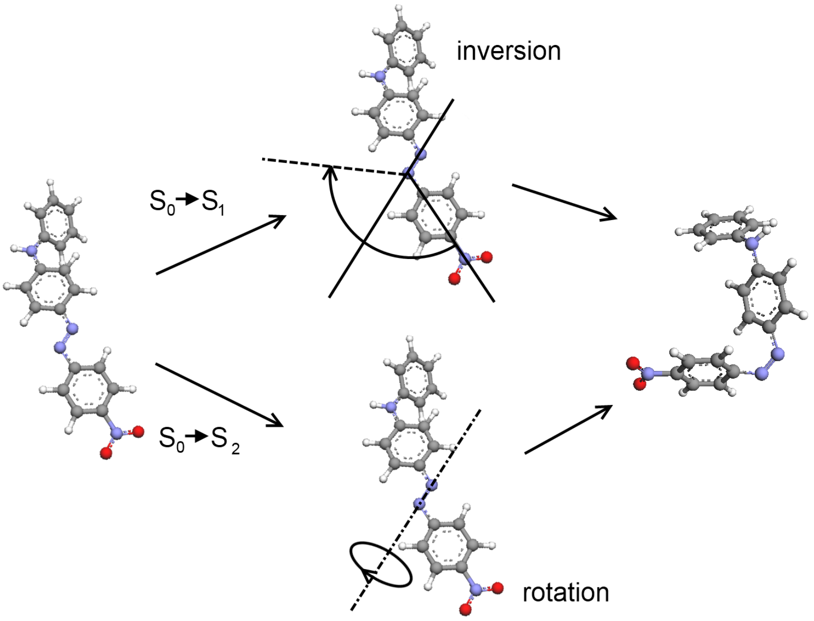

Figure 5.6: Possible isomerization pathways for 4-anilino-4'-nitroazobenzene - Rotation and inversion pathways are shown; the inducing transitions are marked in the figure.

The azobenzene molecule is built from two aromatic carbon rings connected via an -N=N- (azo) bridge. After the substitution of hydrogens in the farthest opposite positions in azobenzene with -NO_2 (nitro) and C_6H_5NH- (anilino), groups one gets the 4-anilino-4'-nitroazobenzene molecule. At RT it is an orange powder with a melting point at around 160°C. Its molar mass equals to 318.33 g/mol and it is easily soluble in most solvents. The substituted groups effectively increase the energy of the azo group π bonding orbital and lower the energy of the π^* antibonding orbital, thus lowering the energy of the $\pi - \pi^*$ transition. Apart from the $\pi - \pi^*$ transition a $\mathrm{n} - \pi^*$ transition is also observed, because of the lone pair electrons on the azo group nitrogen atoms.

The azobenzene derivatives have very similar properties, because as long as carbon rings are aromatic, the azo bridge is intact, and the only differences arise from the additional groups, their electronic properties and chemical functions. It is obvious that for an isolated molecule side groups do not modify the isomerization process unless these groups interact with each other. This is not true for solutions, solids and molecules adsorbed on surfaces. Here, side groups modify the isomerization process via interactions not only with other groups in the molecule itself but also with the direct chemical surroundings (solution molecules, other molecules in solids or surfaces). The chemical surroundings of the molecule have the biggest impact on the dynamics and probability of isomerization reactions i.e. when an azobenzene derivative with long chains as side groups is undergoing an isomerization in solution, the chains interact with a lot of solution molecules, giving rise to a strong energetic barrier for the fast transitions and as an effect only slow transitions are possible. These slow transitions are less probable, however, because of the alternative relaxation processes such as light emission or energy transfer.

The isomerization reaction of azobenzene and its derivatives are one of the most studied of light-induced molecular processes. The $\mathrm{n}-\pi^*$ transition of *trans*-azobenzene is centered at 440 nm and formally symmetry forbidden with an molar extinction coefficient (ϵ) of around 400 M^{-1} cm^{-1}. This value is relatively large for the forbidden transition, which is interpreted in terms of vibronic coupling between the $\mathrm{n}-\pi^*$ and $\pi-\pi^*$ states [53]. On the other hand, the $\mathrm{n}-\pi^*$ absorption of *cis*-azobenzene is an allowed transition with an $\epsilon \approx 1500$ M^{-1} cm^{-1} at 440 nm. The $\pi-\pi^*$ transition of *trans*-azobenzene is centered at 320-350 nm with the $\epsilon \approx 2-3 \cdot 10^4$ M^{-1} cm^{-1}, and the $\pi-\pi^*$ transition of the *cis* form has a peak shorter than that of the *trans* form ($\epsilon \approx 10^3$ M^{-1} cm^{-1} at 260-300 nm) [41]. It has been proposed that the photoisomerization of azobenzene depends on the excitation wavelength as shown in Figure 5.6 [53] The *trans* to *cis* isomerization proceeds through an inversion mechanism under $\mathrm{n}-\pi^*$ excitation, whereas the rotational mechanism operates under an $\pi-\pi^*$ excitation similar to the isomerization of stilbene. In the inversion mechanism, a linear geometry in the transition state is not involved because it is higher in energy than a semilinear geometry as given in Figure 5.6. In addition, no influence of oxygen or heavy atoms was observed in the photoisomerization reaction of the azobenzene [54], suggesting a singlet pathway of photoisomerization. In *trans*-azobenzene and its derivatives without any restrictions, the quantum yields of the *trans* to *cis* isomerization for $\pi-\pi^*$ excitation are always smaller (≈0.1) by a factor of 2 [54–58], indicating the violation of Kasha's rule. This may be an indication of a rotational mechanism operating for the *trans* to *cis* isomerization of azobenzene for $\pi-\pi^*$ excitation, which is supported by the molecular orbital calculations [53, 59]. On the other hand, for the *trans* to *cis* thermal isomerization of diazene, *ab-initio* molecular orbital calculations based on the CIPSI algorithm (6-331

+ G (3df,2p) basis set) have been carried out to estimate the isomerization mechanism [60] The inversion transition state is a little smaller (6-7 kcal/mol) in energy than the rotation, which indicates the competition of inversion and rotation in azo compounds derived from diazene.

Femtosecond spectroscopic studies and the analysis of resonance Raman excitation profiles have been performed to estimate the photoisomerization mechanism of azobenzene for both $n - \pi^*$ and $\pi - \pi^*$ excitation conditions [61–67]. From a historical point of view, Morgante and Struve reported the fluorescence dynamics of *trans*-azobenzene from the $\pi - \pi^*$ (S_2) state by a picosecond Nd:glass laser and an optical Kerr gate method, and estimated the lifetime to be ≈5 ps [68] although they have not reported the fluorescence spectrum. The fluorescence spectrum from the S_2 state of *trans*-azobenzene derivatives and their quantum yields were examined by Hamai and Hirayama [69]. They reported that the fluorescence spectrum from the S_2 state has a maximum at 385 nm with quantum yield $\approx 1.7 \cdot 10^{-5}$ for *trans*-azobenzene and a maximum at ≈410 nm with quantum yield $\approx 0.9 \cdot 10^{-5}$ for 1-methoxy trans-azobenzene. The S_2 lifetime of *trans*-azobenzene was also estimated to be ca. 60 fs using the Strickler-Berg equation. On the other hand, an S_2 lifetime of ≈250 fs was evaluated from the quantum yield $\approx 1 \cdot 10^{-4}$ by Monti et al. [59]. The experimental data for *trans*-BMAB with a fluorescence maximum at ≈400 nm and a lifetime of ≈250 fs [64] are in good agreement with the reported and estimated values of the S_2 fluorescence of *trans*-azobenzene [41].

The observation of the S_2 fluorescence of azobenzene derivatives is direct evidence of the violation of Kasha's rule. In addition to the radiative transition, the nonradiative process from the S_2 to S_0 state may also exist as a competitive process with internal conversion from the S_2 to S_1 states. These radiative and nonradiative transitions from the $\pi - \pi^*$ (S_2) to the ground states result rather in the lower quantum yield of *trans* to *cis* isomerization from the $\pi - \pi^*$ (S_2) state than that from the $n - \pi^*$ (S_1) state, even if we only consider the isomerization of azobenzene in the S_1 manifold [41].

Apart from studies made on solutions or liquid crystals, recently a lot of interest is being focused on the molecules adsorbed at surfaces. The isomerization of native azobenzene [70] and amino-nitroazobenzene [71, 72] on Au(111) was successfully induced by inelastically tunneling electrons from the STM tip. The electric field of the STM tip [73], light [74–78] and thermal activation [75, 76] induce the isomerization of tetra-tert-butylazobenzene (TBA) adsorbed on Au(111). In contrast, the STM-induced isomerization of di-cyano-azobenzene on Cu(100) is irreversible [79], and of TBA adsorbed on Cu(111) and Au(100) completely suppressed [73]. Thus, the weak interaction with an inert surface like the Au(111) surface seems to be crucial for preserving the switching ability of the azobenzene molecules upon adsorption though even on the noble Au(111) surface 4-dimethylamino-azobenzene-40-sulfonic acid is found to isomerize irreversibly [72, 80].

There are only a few reports on the adsorption and isomerization of molecules on silicon surfaces [81, 82].

In order to lower the interactions of molecules with the surface, one of several approaches to the decoupling is used. First and most obvious is using the inert surface as Au(111) [73, 74, 76, 77, 80, 83]. It is the most extensively used but also insufficient for most light induced processes [84]. Altering the molecule with spacer groups like in TBA although it leads to the isomerization, results that the mechanism of the switch is surface mediated and not direct [77]. The next approach is to adsorb molecules on thin insulating layers, which in some cases has been shown to work, but other groups claim that a 2 monolayers thick insulator such as NaCl does not decouple the molecule from the surface completely and on the other hand a thicker layer would prevent the electrons from tunneling. The least used option is to physisorbe the molecule. It was shown that certain molecules that chemisorb to the surface can be trapped in a physisorption state [85] via a low temperature adsorption.

Unfortunately, when weak molecule–surface interactions are achieved, the diffusion of isolated molecules is a competing process to their isomerization [71, 72]. Diffusion is suppressed when the molecules are assembled into larger islands [73, 86] or anchored to special adsorption sites [70]. The isomerization of these immobilized azobenzene molecules lifts one part of the molecules away from the surface [70, 73, 86] which complicates a possible incorporation into electronic circuits [80].

Isolated molecules of amino-nitroazobenzene remain flat in both configurations [71, 72], but the *cis* configuration of the molecule becomes also 3D upon anchoring to other molecules to suppress the diffusion [71].

Bonding to (many) molecules of the same type leads to the formation of supramolecular assemblies [87–90]. Recently, investigations of azobenzene-based supramolecular assemblies were reported [80, 91–93]. But the switching inside these assemblies was achieved only in the case of amino-nitroazobenzene supramolecular assemblies on a Au(111) surface [80].

Although many successful attempts of isomerization have been reported, most of them were done on an inert Au(111) surface. Metallic substrates are useless from the application point of view, because devices would be in constant shortcut. Still the Au(111) surface is the easiest to conduct experiments. Therefore, there is a need to determine the influence of different substrates on the molecules adsorption configurations and switching possibilities. This knowledge should help in choosing the right molecules for incorporation with Si(100) or Ge(100) surfaces. This thesis is dedicated to this task.

Chapter 6

Results and Discussion

6.1 Calculated Molecules Structure in Gas Phase

The calculations of gas phase structures of 4-anilino-4'nitroazobenzene are essential for further analyzis of the experimental data and also for fine tuning of the Fireball software for the DFT calculations of adsorbed structures. The optimization of geometry was done via the ABINIT software, with a general gradient approximation (PBE - Perdew, Burke, and Ernzerhof) approach using the Fritz-Haber-Institute pseudopotentials. Figure 6.1 A and B shows the structure of both isomers. In *trans* form the nitro group is placed in the plane of the carbon ring, marked as 3, and the bond length between the N atom and C atom is 144 pm. As usual for nitro groups, the bond between N and O atoms is covalent and there is a common orbital bonding both the O atoms. The carbon ring is barely perturbated from the benzene molecule with the distance between opposite C atoms being 274 pm. The bond between the carbon ring number 3 and the azo bridge is deviated from the axis of the carbon ring by 3.1° and it is 139 pm long. The double bond in the azo bridge is 126 pm long. The azo bridge is connected to the carbon ring number 2, by a 137 pm long single bond. Ring number 2 is twisted counterclockwise from the plane of the ring number 3. Still the angle is small 3.5°. Ring number 3 is 278 pm long. It is connected by a single bond with an -NH- (amine) group. This bond is 136 pm long. The amine group together with the carbon ring number 1 are parts of the anilino group. The angle between single bonds to carbon rings in the amine group is 124.1°. The distance between the O atom and the furthest H atom is 1642 pm. All of the above makes the *trans* isomer appear as

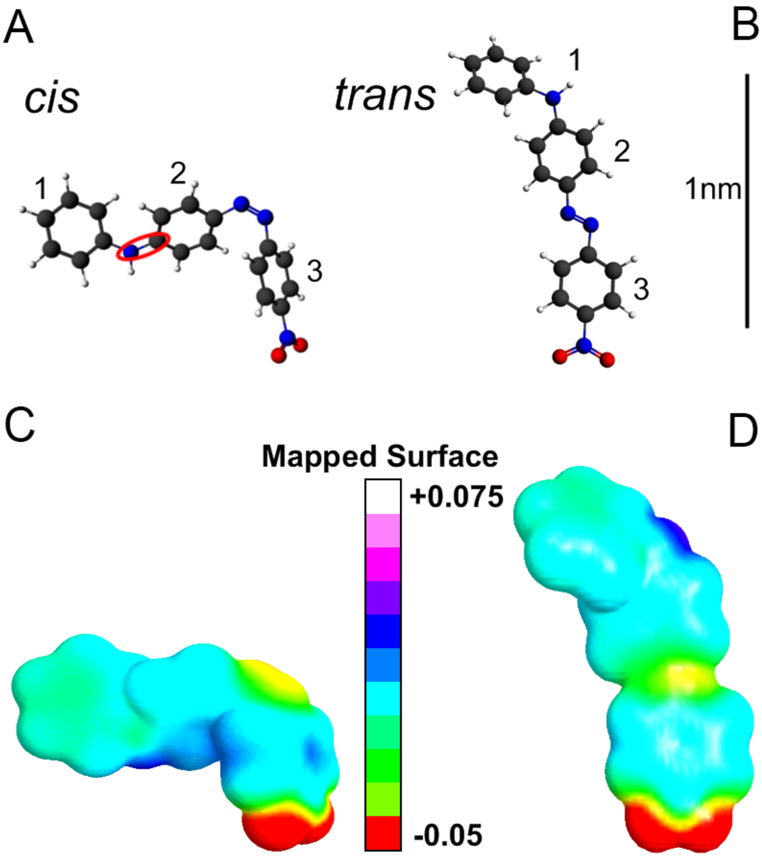

Figure 6.1: Calculated structures of *cis* and *trans* 4-anilino-4'-nitroazobenzene - A and B - the gas phase structure of the *cis* and *trans* isomers respectively, with an easily rotatable single bond marked on A, C and D - ESP mapped over the constant contour of states density for the above structures.

a flat elongated molecule. In the *cis* form all groups stay the same within 1 pm and 0.5° precision. The only difference as regards geometry lies in the azo bridge and in the placement of carbon rings numbers 2 and 3 with respect to each other. The torque angle with respect to the azo bridge of both carbon rings is 21° compared to 173.2° for the *trans* isomer. In the *cis* form the molecule is much more compact and the distance between O atom and H atom at the furthest ends of the molecule is 1412 pm. As a consequence, the *cis* isomer appears more as a 3D object than the *trans* conformer.

The single bond between the carbon ring number 2 and the anilino group is easily rotatable. The difference in energy as a function of the angle is never bigger than 1 eV,

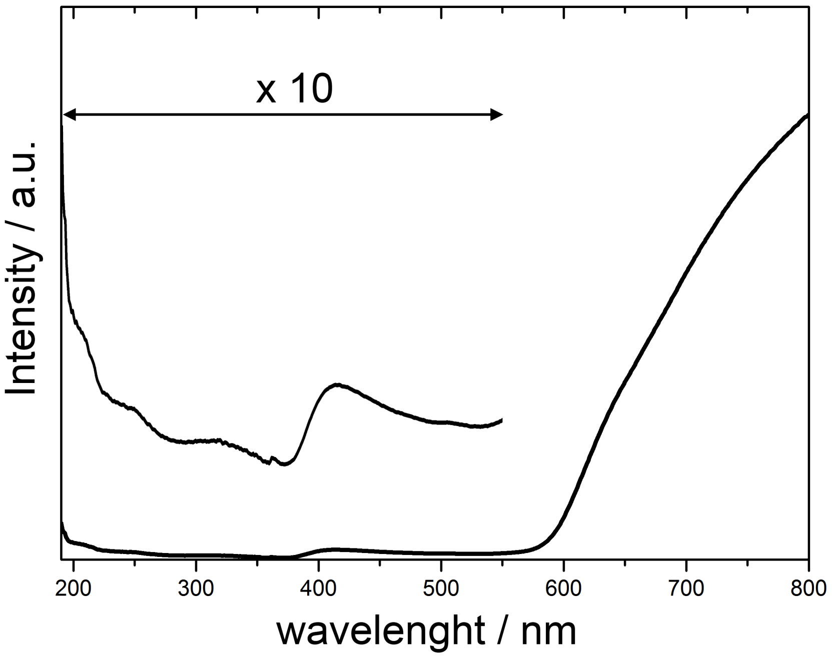

Figure 6.2: UV-VIS spectroscopy of solid 4-anilino-4'-nitroazobenzene - Spectroscopy made on a solid state sample, the $< 180\text{nm}, 550\text{nm} >$ part of the spectra is multiplied to show the detailed structure.

and for some configurations goes down to about 0.4 eV. Therefore, the anilino group can rotate due to the interaction with substrate during the adsorption.

6.2 Optical Spectroscopy

A spectroscopic characterization of molecules before isomerization experiments is essential in choosing correct conditions for the reaction. A UV-VIS spectroscopy of molecules in solid state gives the best approximation of how the absorption of light might look for molecules adsorbed on surfaces. 4-anilino-4'-nitroazobenzene absorbs light at four wide bands with the maxima at 250 nm, 318 nm, 414 nm and 508 nm. There is a huge absorption peak with its maxima above 800 nm but it is not connected with any isomerization processes. The 250 nm band is the $S_0 \rightarrow S_2$ transition of trans *trans* isomer, the 318 nm band is the $S_0 \rightarrow S_2$ of the *cis* isomer, and 414 nm and 508 nm are the

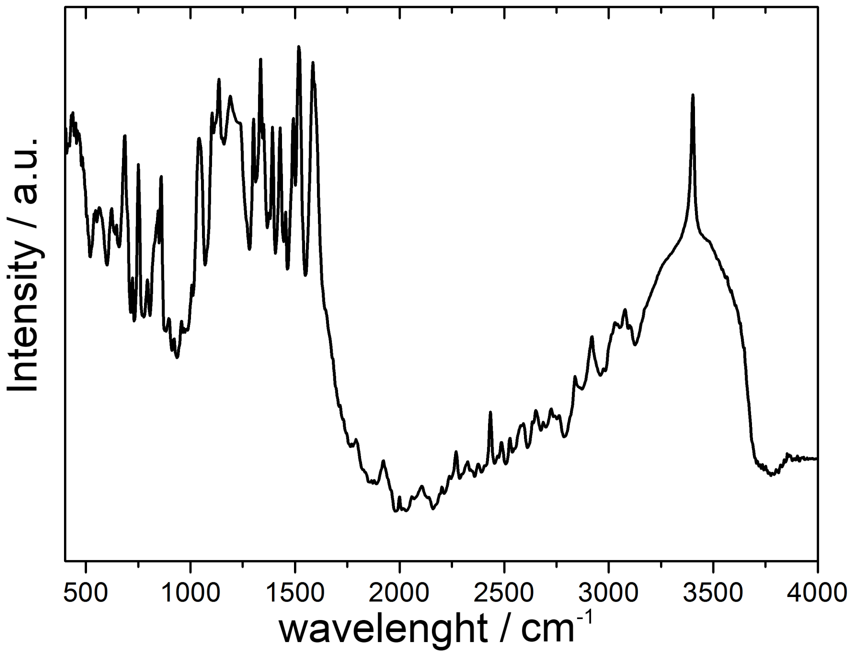

Figure 6.3: IR spectroscopy of solid 4-anilino-4'-nitroazobenzene - The strong peak at around 3400 cm^{-1} is caused by C-C bonds in the molecule; other important peaks are described in table 6.1.

$S_0 \rightarrow S_1$ transitions of the *cis* and *trans* isomers respectively. The width of the bands is about 50 nm. Those values change if molecules are dissolved in solutions or examined in the gas phase.

The IR and Raman spectroscopies were performed in order to identify possible vibrational modes for further use in IETS. Two different lasers were used in the Raman spectroscopy to cover all the possible vibrations. A fluorescent peak which affects the whole energy range was subtracted from the gathered spectra. Also, to gain the resolution and intensity of the peaks the Raman spectra were gathered 3 times and added. The IR spectrum was gathered using a fourier transform infrared spectroscopy (FTIR) device with a liquid nitrogen (LN) cooling of both the sample and detector. Figures 6.3 and 6.4 show the gathered spectra and all the peaks from spectroscopies are compared with the results of the calculations for nitroazobenzene made by Biswas et al. [94] in table 6.1. Not all the peaks find their representation in these calculations as the molecule is more complex than the calculated one.

Mode[94]	FTIR	Raman 785 nm	Raman 488 nm	Calculated[94]
ip(C-C), t(C-C)		412		428
t(C-C),oop(C-H)	505			503
ip(C-N),ip(N-O),s(C-C)				510
ip(C-N),ip(C-C)	546			557
t(C-C),oop(C-H)	565			561
ip(C-C),ip(C-H)	623			607
ip(C-C)	646			646
ip(C-C)	687			662
t(C-C),oop(C-H)	723			714
ip(C-C),ip(C-N)				716
t(C-C),oop(C-H)	750			768
t(C-C),oop(C-H)	795			811
oop(C-H)	845			883
oop(C-H)	860			887
	899			
t(C-C)	922	922		921
s(C-C)	957			940
	968			
	1007			
t(C-C)				1034
ip(C-C)	1039			1039
s(C-C)	1103		1099	1123
s(C-C)	1136	1138	1132	1141
			1172	
s(C-N)	1190	1191	1188	1181
s(C-C)				1205
s(C-C)	1238			1226
s(C-N)			1289	1272
s(N-O)	1302	1302	1299	1288
		1312		
	1336	1340	1330	
ip(C-H)	1350			1353
s(C-C)	1375		1373	1373
s(C-C)	1392	1396	1390	1396
s(C-C)	1429		1426	1438
s(N=N)	1456	1443	1453	1462
	1493		1484	
s(C-C)	1518			1536
s(C-C)				1541
	1585	1591		
s(C-C)		1608	1603	1642
s(C-C)				1652
s(C-C)				1659
s(C-H)			2874	
s(C-H)	3402			

Table 6.1: Vibration modes of solid 4-anilino-4'-nitroazobenzene obtained via various methods. In mode names: ip stands for in-plane, oop stands for out-of-plane bending, s stands for stretch, and t stands for torsion.

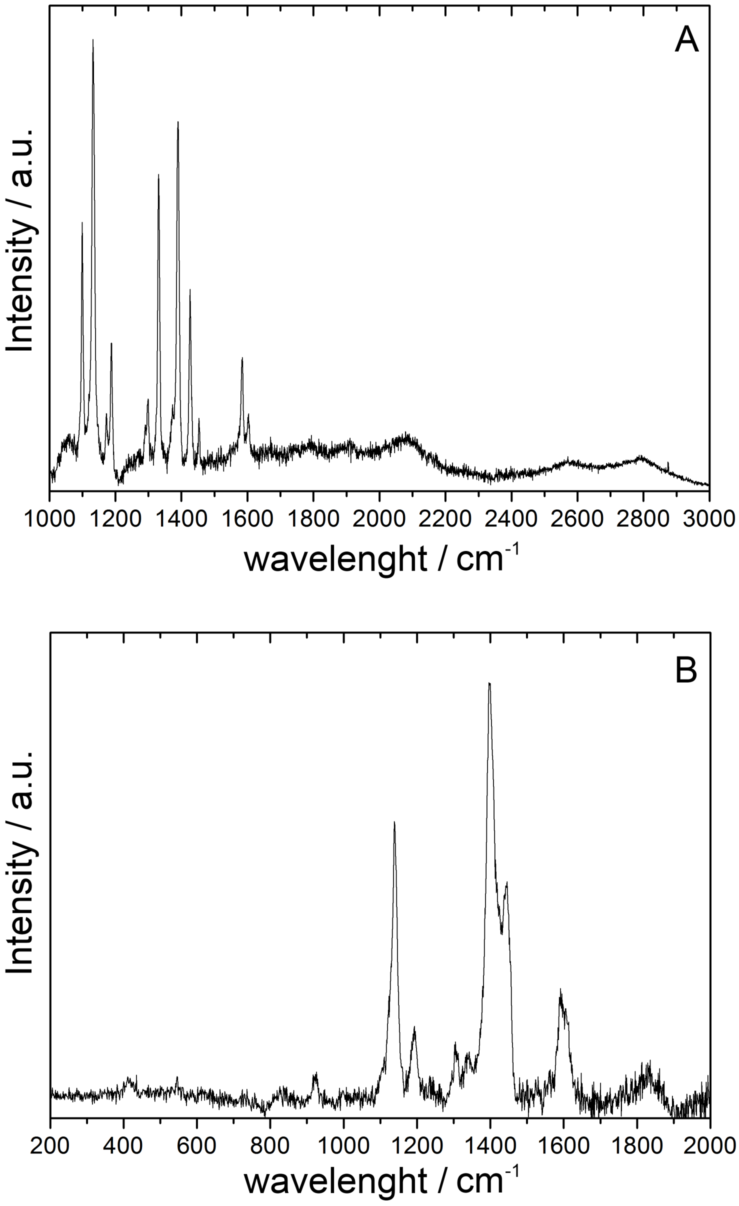

Figure 6.4: Raman spectroscopy of solid 4-anilino-4'-nitroazobenzene - A - spectroscopy gathered while exciting with a 785 nm laser, B - spectroscopy gathered while exciting with a 488 nm laser; all the peaks are described in table 6.1.

Because vibrational modes are necessary for the identification of adsorbed molecules, the most interesting ones are those in the energetic range of IETS that is up to a 100 meV (805 cm^{-1}). In this energetic range I measured 11 vibrations, 10 of which were by means of FTIR. All these peaks were predicted by calculations and correspond to the vibrations of the azobenzene part of the molecule. The out-of-plane vibrations are those at 62.7 meV (505 cm^{-1}), 70 meV (565 cm^{-1}), 90 meV (723 cm^{-1}), 93 meV (750 cm^{-1}) and 99 meV (795 cm^{-1}). The in-plane modes are those at 51 meV (412 cm^{-1}), 63.3 meV (510 cm^{-1}), 68 meV (546 cm^{-1}), 77 meV (623 cm^{-1}), 80 meV (646 cm^{-1}), and 82 meV (662 cm^{-1}). Despite the different character of the vibrations they are not Raman active. Therefore, these 10 vibrations do not change the polarizability of the molecule. This in fact might suggest that they also do not change the conductance of the molecule, and as such would be inactive in IETS. In fact most in-plane modes are inactive in the IETS and Raman.

Analyzing table 6.1 one comes to a conclusion that the assignment of the ip(C-C) calculated to be at 428 cm^{-1} to the 412 cm^{-1} Raman peak, is wrong. Mostly the stretch and torsion vibrations of 4-anilino-4'-nitroazobenzene are active in the Raman spectroscopy. Also all stretch modes are much higher energetically, therefore this peak should be assigned to a torsion vibration in the carbon rings which is suggested in the supporting information of [94]. Actually, looking at the results of the calculations given in supplementary information for pure 4-nitroazobenzene one finds only t(C-C) at 428 cm^{-1}, t(C-C) at 439 cm^{-1}, t(C-C), oop(C-H), and oop(C-N) at 692 cm^{-1} and finally ip(C-C), s(C-C), and s(C-N) at 815 cm^{-1}. Although the reasons for such unintegrity of information between publication and its supporting material is unclear, the assignment of the t(C-C) mode to the 412 cm^{-1} vibration seams reasonable.

6.3 Flash Photolysis

From the UV-VIS made for solids, the band responsible for the rotation pathway of isomerization lies at 250 nm. It is obvious that this value will change when the molecule is diluted or adsorbed on the surface. Nevertheless, this is a good starting point. Before I tried to adsorb molecules at the surface and isomerize single adsorbed molecules I checked the dynamics of the isomerization using the flash photolysis method. For these experiments I dissolved the molecules in acetonitrile (ACN). Figure 6.5 shows the spectra gathered before and after the flash photolysis experiment. Both have similar and the difference is negligible as comes from many apparatus aspects such as the slightly different position of the sample in the machine. This proves that the molecules

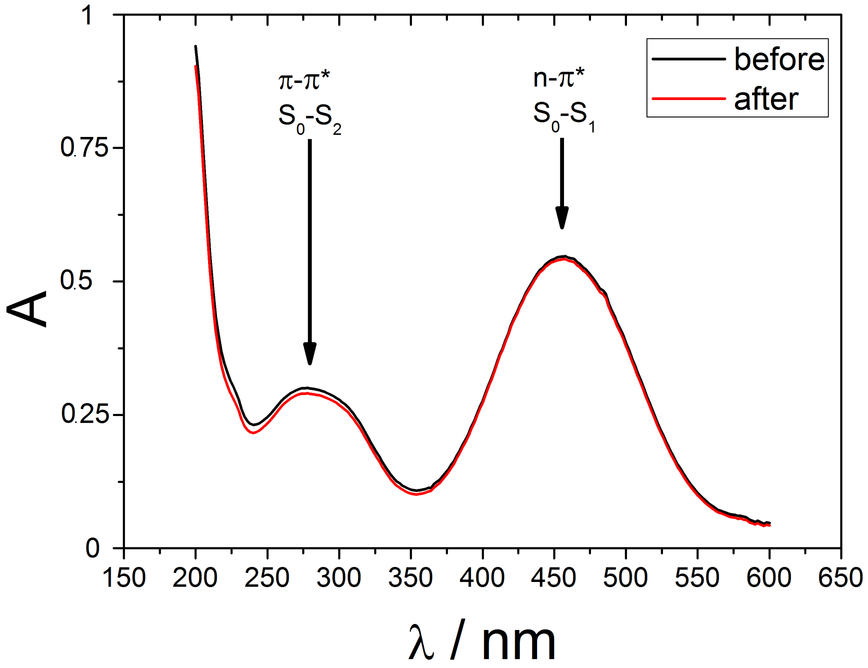

Figure 6.5: UV-VIS spectroscopy of 4-anilino-4'-nitroazobenzene in ACN - The spectra show the energy shift of bands into the lower energy bracket in comparison to Figure 6.2 .

in the solution survived the experiment and that the lasers light intensity was properly chosen not to destroy them. Secondly comparing the spectra in Figure 6.5 to the one in Figure 6.2, it is obvious that there is a shift of bands to the lower energy range. The reason for this are the weaker next neighbor interactions in the liquid solution as compared to the solid state.

For the experiment, I choose a 266 nm pulse laser which is in the range of the bands for both solid and dissolved absorption bands responsible for the rotation pathway of isomerization. The measurement time resolution was 1 ns and the probing time was 1 μs. The laser pulse lasted for 1 ns. Figure 6.6 A shows the A(t) curve registered for absorption at 400 nm. At certain time intervals, data points were taken from the curves registered for each wavelength - giving rise to differential absorbance spectra at different time intervals, as shown in Figure 6.6 B. Fitting exponential decay to the A(t) curves and averaging the results, we see that the lifetime for the excited state is 218 ns ±12 ns. The green line in the differential spectra shows the difference in

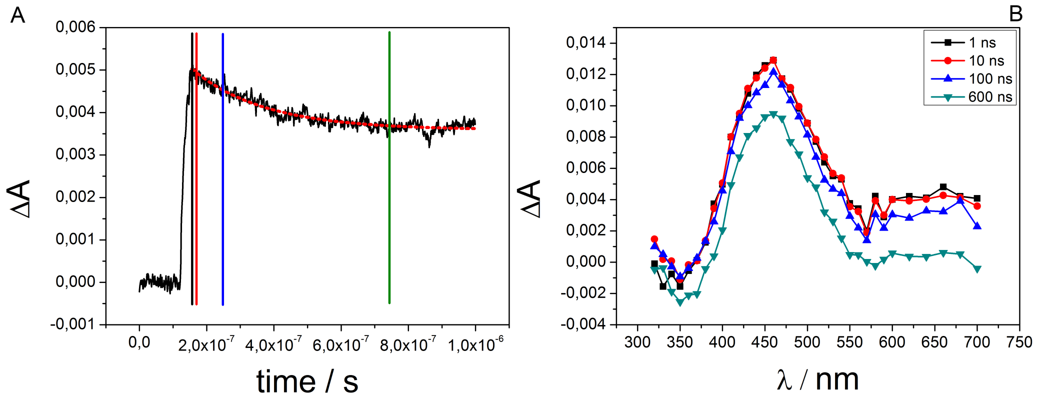

Figure 6.6: Differential absorbance spectroscopy of 4-anilino-4'-nitroazobenzene in ACN - A - shows the time resolved absorbance spectroscopy curve registered at 400 nm, with vertical color lines pointing to time intervals, B - differential spectroscopy at selected time intervals after the laser pulse.

absorbance between the *trans* and *cis* isomers. The band at 350 nm decays, while the band at 460 nm rises. This proves that the isomerization indeed was induced by the 266 nm laser, through a S_2 excited state with a lifetime of 218 nm. The lifetime of the *cis* isomer is much bigger at the level of 20' [46].

The long lifetime of the excited state gives rise to two possibilities for molecules adsorbed at surfaces. First, the excited state lives long enough to enable isomerization, because there are no alternative relaxation processes for molecules in solution. If this would be the case for adsorbed molecules, then we would observe photoisomerization in further experiments. The second possibility is less satisfactory. The isomerization reaction is very slow, and there are a number of much faster processes such as Dexter or Förster energy transfers to the surface[95, 96].

6.4 Adsorption Geometries at Monocrystalline Surfaces

6.4.1 4-anilino-4'nitroazobenzene on Cu(111)

Part of the following results have already been published[97]. A clean Cu(111) surface prepared as described in the Materials chapter was exposed to the molecules sublimated from the Knudsen cell. The molecules were deposited onto a substrate held at different temperatures starting from the 180 K typical for adsorption of molecules at the Au(111) surface down to 100 K with 20K steps. At temperatures higher than 120 K, molecules

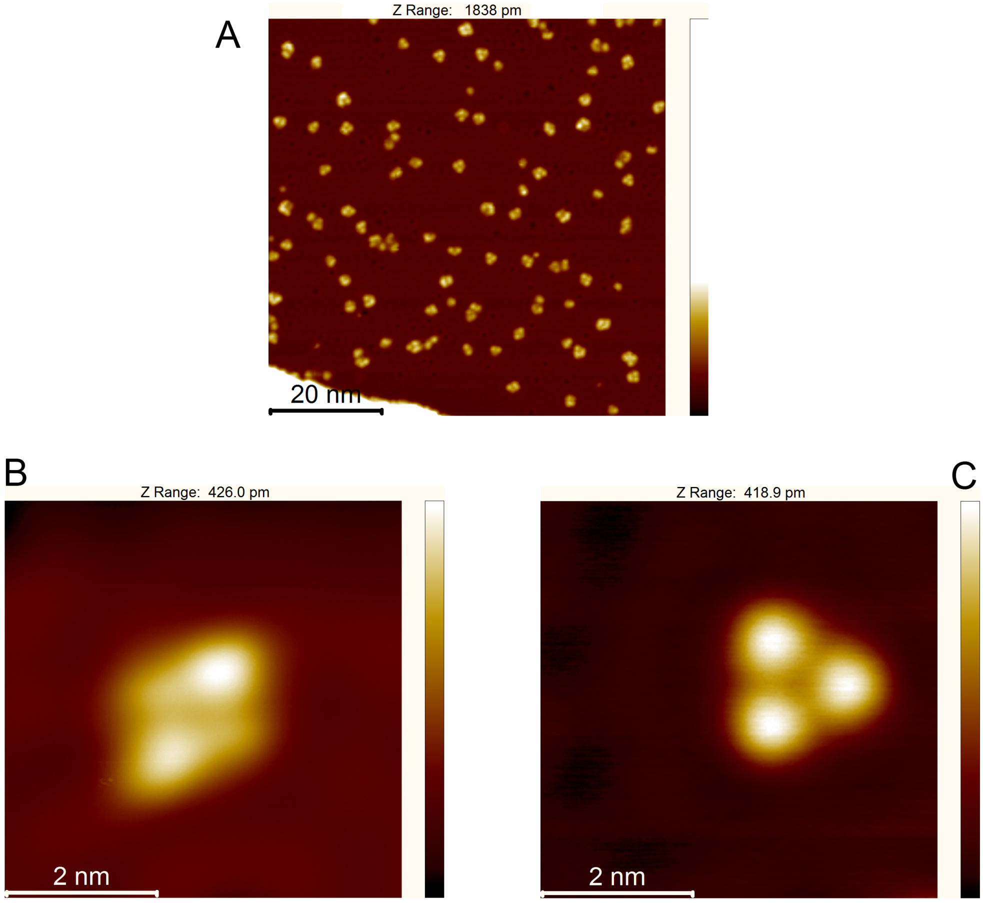

Figure 6.7: STM images of 4-anilino-4'nitroazobenzene adsorbed at the Cu(111) surface - A - Overview image of the surface, B - high resolution image of the 2-dot-form, C - high resolution image of the 3-dot-form. Tunneling parameters: A - I_t=89 pA, U_t=100 mV, B - I_t=57 pA, U_t=100 mV, C - I_t=29 pA, U_t=100 mV.

did not stick to the Cu(111) surface. The first successful deposition was achieved for substrate held at 100 K.

I start here by identifying the adsorbed molecules in the STM images. One must keep in mind that the STM is not a profilometer and that the images strongly depend on the LDOS of the sample. Therefore, when analyzing the images only the apparent height is discussed and not the real height as in Van der Waals volume. After adsorption at 100 K, two predominant shapes consistent with the size of the simulated molecules are observed (Figure 6.7 A). One of them consists of two protrusions that are connected via a broader reduced protrusion with 75% of the apparent height (referred to as the

2-dot-form, Figure 6.7 B). Profiles with Gaussians fits reveal that the two protrusions have a slightly different apparent height by 50 pm on average. The distance between the maxima of the Gaussians is (1.23 ± 0.02) nm. The second form consists of three spots forming an equal-sided triangle (called the 3-dot-form, Figure 6.7 C). The profiles indicate that for this form there is no apparent height difference between the protrusions. The distances between the fitted Gaussians are very similar (1.03 ± 0.02) nm on average. This 3-dot-form appears at only $n \times 60°$ configurations. This is due to the 6-fold dymetry of the surface. $(36.6 \pm 9.8)\%$ of the population of observed species show the 3-dot-form and $(7.3 \pm 1.5)\%$ the 2-dot-form. All other that is nearly 60% of the adsorbed species are much smaller than expected and do not present any regularities. Dissociative adsorption of the molecules induced by the Cu(111) substrate at 100 K could be a possible explanation.

To check this hypothesis, I evaporated 4-anilino-4'-nitroazobenzene onto a substrate held at 20K. Indeed, the majority of the objects found on the surface was of similar sizes to the 3-dot- and the 2-dot-forms. However, this low temperature does not allow all molecules to accommodate into an energetically favorable position, as they might stick with the molecular part that first touches the sample. This causes the presence of many different forms of 4-anilino-4'-nitroazobenzene on the Cu(111) surface. We still observe the 3-dot-form and 2-dot-form, but the population of both species is below 5%. Actually 80% of all the species on the sample transform into one of two stable forms during the IET manipulation. Thus, the higher adsorption temperature of 100 K provides the energy for the isomers to accommodate into their stable adsorption geometry but also for dissociation.

Based on earlier measurements of 4-anilino-4'-nitroazobenzene adsorbed on Au(111) held at 250K, we would expect a chemisorbed form of the molecule to be imaged by the STM as an elongated shape with 3 protrusions, one above each phenyl ring [80]. The structures obtained via adsorption on a Cu(111) held at a temperature below 100K differ from those obtained on Au(111) adsorbed at 250 K, which is close to the desorption temperature for gold substrate. This indicates a different adsorption state, possibly physisorption on Cu(111) and chemisorption on Au(111). Because of the dissociative adsorption on Cu(111) at temperatures higher than 100K, it is not possible to validate this assumption by simple adsorption of molecules at higher temperatures. I thus employed the local high voltage procedure described in the Methods chapter in order

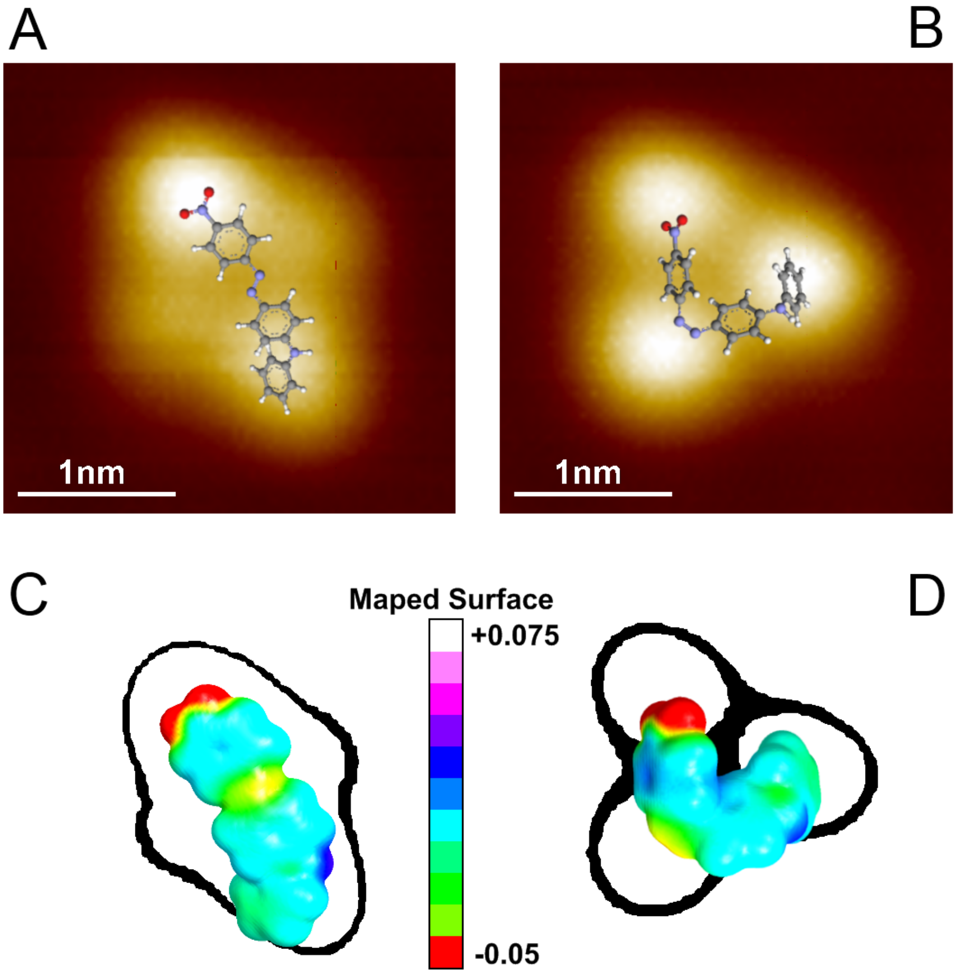

Figure 6.8: Assignment of calculated models - A - Ball-stick model of the *trans* isomer superimposed over the STM image of the 2-dot-form, B - ball-stick model of the *cis* isomer superimposed over the STM image of the 3-dot-form, C and D - ESP maps for the above models superimposed for the izoheight line taken from above the STM images. Tunneling parameters: A - I_t=69 pA, U_t=100 mV, B - I_t=69 pA, U_t=100 mV.

to induce the chemisorption of the molecules. The treatment affects an area of about a 500 μm radius. In the middle of this area all molecules are desorbed. Near its border, molecules have converted into linear shape, with three protrusions, two very closely bounded and one which looks slightly detached (see Figure 6.9). The same shape of the 4-anilino-4'-nitroazobezneze was observed on the Au(111) surface [80]. Thus,

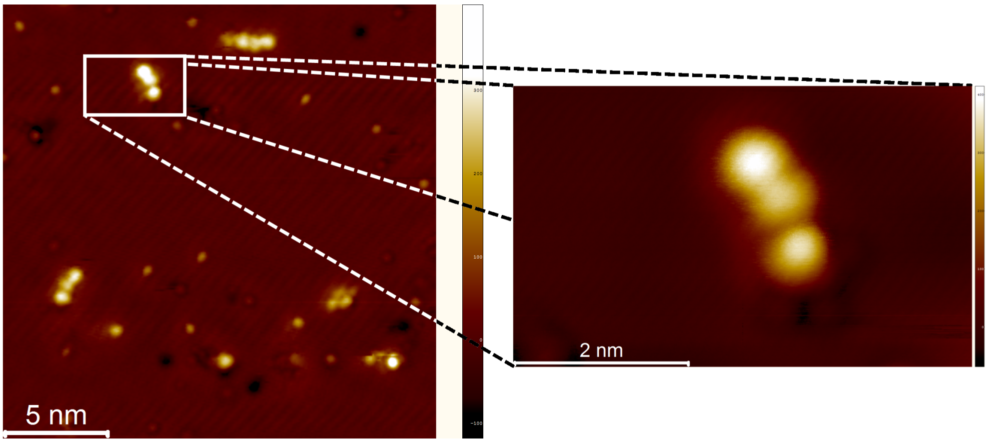

Figure 6.9: STM image of 4-anilino-4'-nitroazobenzene on Cu(111) after local high voltage/high current treatment - A - overview image, B - magnification of a single molecule. Tunneling parameters: I_t=69 pA, U_t=100 mV.

this proves that the molecules are indeed trapped in a physisorption well by the low temperature adsorption. Having established that the two STM images presented in Figure 6.7 are the two most stable forms of physisorbed 4-anilino-4'-nitroazobenzene, there arises a question, which structure is the *cis* and which is the *trans* isomer. At first sight, the two structures calculated in the gas phase fit only poorly to the STM images (Figure 6.1 and 6.8). Because the DFT does not reproduce physisorption, a different method of STM images recognition was necessary. The electrostatic potential of the molecule mapped onto the surface of the electron density (for a ground state) shows where the frontier electron density for the molecule is greatest (or least) relative to the nuclei. It has been shown before that negative values of the ESP maps reflect regions of high conductance for physisorbed molecules imaged within the HOMO-LUMO gap [48], thus giving the regions of the molecule which should be visible as maxima in the STM image. The calculated *trans* structure reveals three charge maxima in the ESP map located on the amine, azo and nitro groups (see Figure 6.8) with small, medium, and large intensivity, respectively. This suggests that the nitro group should show a higher apparent height in the STM images than the azo or amine groups. The distance in the calculated model between the nitrogen atoms in the amine and nitro group is 1.16 nm. Because the maximum of the ESP map is not localized on the N atom of the nitro group but is shifted into the direction of oxygen atoms, the structure fits quite nicely with the 2-dot-form.

The ESP map calculated for the *cis* form does not fit to the STM image of the 3-dot-form. To check the flexibility of the molecule, I looked for local energy minima in the geometry optimization of the molecule in the gas phase. The -C-N-C- bonds in the anilino group are all single bonds and as such easily rotatable. A local minimum for a structure obtained by flipping the first ring around the C-N bond axis (marked in Figure 6.1 A) by about 180 degrees was calculated using the PM3 method. The obtained structure varied mostly with the -C-N-C- angle by about 4.5°. Distances between the azo and amine groups in the structure of DO1 slightly changed by less than 7.5 pm and the overall energy as calculated by the ZINDO method increased by 59.29 kcal/mol (approximately 0.47eV). Finally, there is the structure shown in Figure 6.8 D. I calculated the ESP map for this structure obtaining a reasonable coherence between the STM image and the model of the molecule. The 3-dot-form is most likely the *cis* isomer. Note that on the surface the *cis* form is the dominant species, as opposed to the gas phase.

6.4.2 4-anilino-4'nitroazobenzene on Si(100)

On a Si(100) surface molecules were deposited only on a substrate held at a temperature of 20 K. The reasoning was as follows, most experiments show that adsorption at higher temperatures leads to chemical decomposition of molecules in the process of dissociative adsorption. Also, a low temperature can induce physisorption of molecules if an energetic physisorption well exists for such a system.

After the deposition of 4-anilino-4'nitroazobenzene, three main features on the sample are obtained. Again I start with identifying the adsorbed molecules in the STM images. All the species found on the surface look different in the occupied and unoccupied states. Figure 6.10 depicts both occupied and unoccupied states STM images of the three main forms. The dominant form of the adsorbed molecule consists of 75% of the species found on the surface. In occupied states it apears as a depresion in the first silicon dimer's row; this depresion takes the place of two dimers in width and has an apparent depth of arond 65 pm. Next, there is a protrusion one and a half silicon dimer's rows long and two dimers wide that has an apparent height of 70 pm and ends with another depresion, which is half silicon dimers row long and two dimers wide. In total it is three silicon dimers rows long, linear and symetric, and two dimers wide. In the unoccupied states this form appears as a double protrusion starting at half the

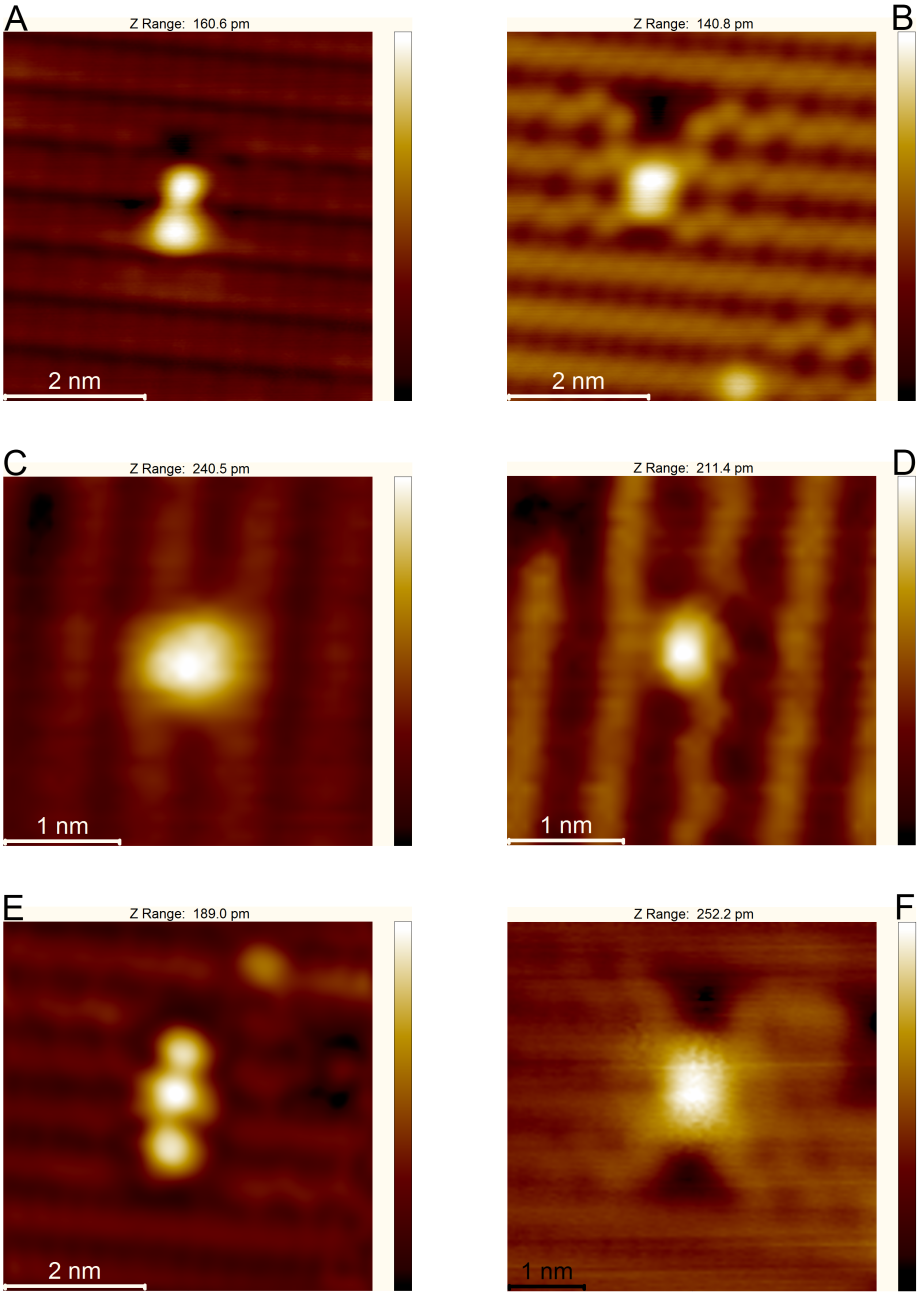

Figure 6.10: STM images of 4-anilino-4'nitroazobenzenes main adsorption configurations at Si(100) - On the left the unoccupied states images, on the right the occupied states images. A-B shows the *trans*-flat configuration, C-D shows the standing configuration and E-F shows the dimer configuration. For details see description in text. Tunneling parameters: A, C, E - I_t=19 pA, U_t=2.2 V, B, D, F - I_t=19 pA, U_t=-2.2 V.

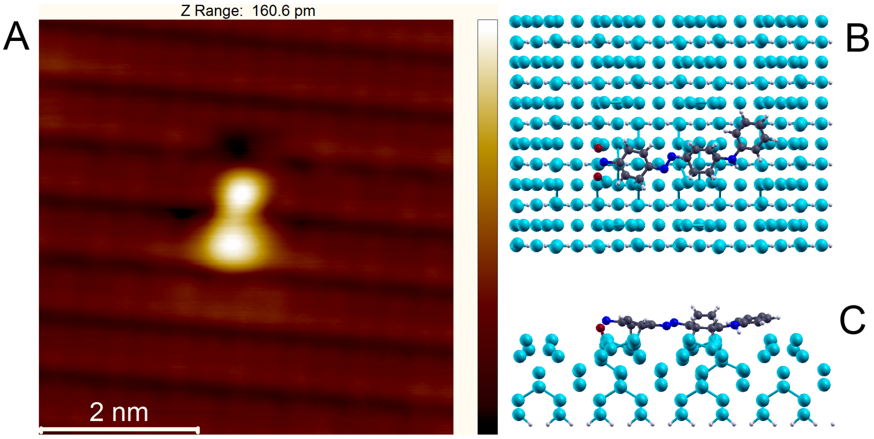

Figure 6.11: STM image and calculated model of the *trans*-flat configuration - A - STM image, B - top view of model, C - side view of model. Tunneling parameters: A - I_t=19 pA, U_t=2.2 V.

first silicon dimers row and ends in the half of the third row. The first protrusion has an apparent height of 90 pm and the second one 175 pm. The distance between the maximas of gausioans fitted into the line profiles is 800 pm. Because the overall length of this form is simillar to the length of the whole molecule, the *trans* isomer in the gas phase and its linear character, this form is later refered to as *trans*-flat. The second form of the molecule on the surface is presented by 11% of the species. In occupied states this form appears as a single protrusion inbetween two silicon dimers rows and two depresions half of a dimer's row long. Again, this form also is two silicon dimers wide. The apparent height of the protrusion is 50 pm. In unoccupied states it appears as a single round protrusion in between silicon dimers rows. No effect on the nearby silicon atoms is observed. The exact shape of the protrusion and its apparent height in unoccupied states has two possible variants suggesting two subforms of this adsorption configuration. The first is more round and almost 200 pm high and the second is more elipsoidal and only 110 pm high. This group of molecules I refer to as standing molecules. The third adsorption configuration is presented by 10% of species on the surface. In occupied states it appears as a depresion in the first silicon dimer's row of an apparent depth of around 65 pm. Next, there is a protrusion of two silicon dimer's rows lenght and 110 pm high. This form ends with another one silicon row long depression. In total, this gives four silicon dimers rows. Again the whole form is two dimers wide. In unoccupied states this form appears as three connected protrusions taking in total

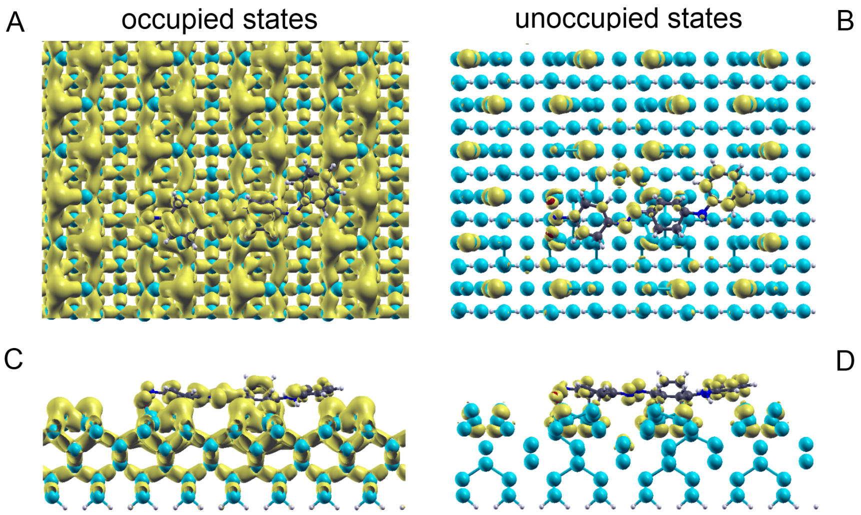

Figure 6.12: Calculated densities izocontours of the *trans*-flat configuration - A - STM image, B - top view of model, C - side view of model.

four silicon dimer's rows having an apparent height of 150 pm. The stucture is shifted between occupied and unoccupied states by a single silicon dimer row. The total length of this form (over 3 nm) is too long to be a single molecule. The STS data shows the complete symmetry of this structure against its middle point, which is in contradiction to the shift in the image of the occupied and unoccupied states. Therefore, it is not a simple dimer of the molecule. Nevertheless, as it is by no means a single molecule it therefore is disregarded in the further analyzis.

In order to identify the adsorption configurations, a DFT study was performed. First the *trans*-flat configuration is discussed. The lower symmetry of the Si(100) surface gives hundreds of adsorption geometries one can think of. But the STM images show that the molecule is laying flat, across silicon dimers rows and takes 3 dimer's rows. This is even more than the molecule itself, but it is a reasonable assumption that a molecule can change the whole dimer by only interacting with one of its atoms. It is symmetric versus its own axis, therefore only the most linear forms of adsorption configurations were taken into account. From the work of Hofer et al.[98] the energetically best configurations of carbon rings were taken into consideration, limiting the number of adsorption configurations for the *trans*-flat form to only several. Out of those selected, the configuration presented in Figure 6.11 is the energetically favored one.

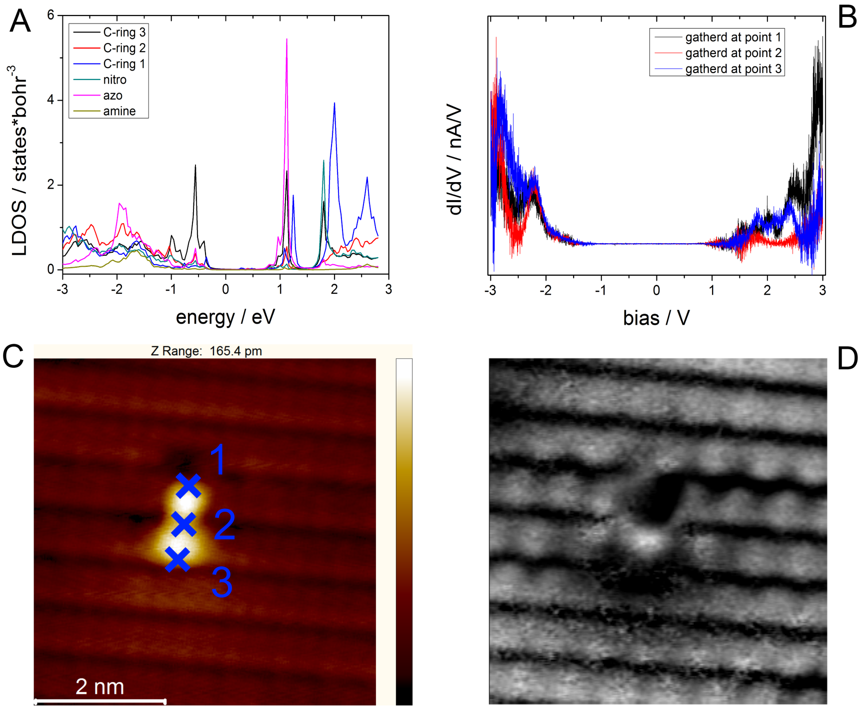

Figure 6.13: Electronic structure of the *trans*-flat configuration - A - calculated LDOS, B - STS curves gathered over points marked in C, C - STM image of occupied states at 1.7 V, D - differential conductance map gathered simultaneously with C. Tunneling parameters: C - I_t=49 pA, U_t=2.2 V, Lock-in parameters B - f=479Hz, A=2mV, t=30ms, D - f=477Hz, A=5mV, t=10ms.

In this configuration the carbon ring number 2 is in a so called tight-bridge configuration above two silicon dimers. Carbon ring number 1 stays free mostly because it is placed above the empty space between the silicon dimer's rows. This carbon ring is intact by the surface with its 280 pm distance between opposite C atoms. The bonds between the carbon rings and amine group are longer, with 144 pm and 152 pm, but the angle is almost the same as in the free molecule 120.2°. A carbon ring in a tight-bridge configuration is no longer aromatic with 4 bonds to Si atoms that are 194 pm, 197 pm, 199 pm, and 206 pm long and 2 remaining C atoms standing up. Still, the ring is 279 pm long which is the same as in a free molecule. The azo bridge is stretched but otherwise intact. The double bond is 141 pm long and single bonds to the C atoms are 147 pm long. The last carbon ring is connected to the surface with 2 Si atoms each from a separate dimer. These bonds are 194 pm and 197 pm long. C atoms that are bound to Si atoms are attracted to the surface while the rest are repulsed and therefore the carbon ring is twisted. The bond between the C atom and the nitro group is 151 pm long. O atoms are bound to Si atoms in dimers already modified by bonds with C atoms from the carbon ring 3. All silicon dimers under the molecule became symmetric and are pulled away from other dimers in their rows. Because of this, the next closest Si dimer is shorer than usual by 4 pm. The second layer of substrate is also slightly deformed by the adsorption. The total bonding energy of the molecule is 9 eV. The calculated density of these states are shown in Figure 6.13 A. Apart from the amine group which has only states at around -1.7 eV all other groups have states in both occupied and unoccupied states. According the theory of Tersoff and Hamann the tunneling current is a sum of all the tunneling channels from the Fermi level to the chosen energy. Therefore, scanning with ±2.2 V, apart from the amine group the molecule should be visible in the STM images assuming that the transport from the molecule to the surface is good and equal for whole molecule. With this assumption I checked the spacial distribution of the LDOS because it could be that due to a charge transfer in the molecule some of the states would be localized not entirely on the origin group. Figure 6.12 shows izocontours of the densities calculated for occupied and unoccupied states and plotted for a constant value of 0.05 state/Bohr^3. The images differ in the energy range of the states taken into account during the calculation. These energy ranges are for occupied states $< -3\ \mathrm{eV}, \mathrm{E_F} >$ and for unoccupied states $(\mathrm{E_F}, 2.8\ \mathrm{eV} >$. The unoccupied states are strongly localized while the occupied states are comparably delocalized. This is not entirely in agreement with the STM images. Also the STS performed over several points on the molecule (see Figure 6.13) or maps of differential conductance do not confirm the calculated LDOS. All this means that the calculated *trans*-flat model is not correct, but still it is the best I can propose at this time. Fortunately, the *trans*-flat configuration is not the most important one.

The standing configuration is much more interesting. Figure 6.14 shows the STM image and the calculated model of this configuration. This is the *trans*-standing configuration. The molecule is bound to the surface by carbon ring number 1 in the tight-bridge configuration. The azobenzene part is standing perpendicular to the surface, screened from its influence by the amine group. The bonds between C atoms and Si atoms are 195 pm, 196 pm, 196 pm, and 198 pm long. The two dimers are symmetric, and closer to each other than in the case of clean silicon. Again the nearest

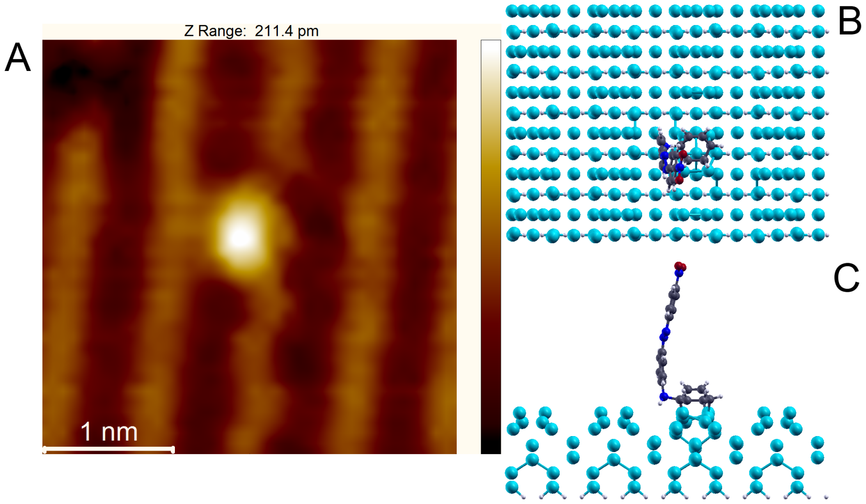

Figure 6.14: STM image and calculated model of the ***trans*****-standing configuration** - A - STM image, B - top view of model, C - side view of model. Tunneling parameters: A - I_t=19 pA, U_t=2.2 V.

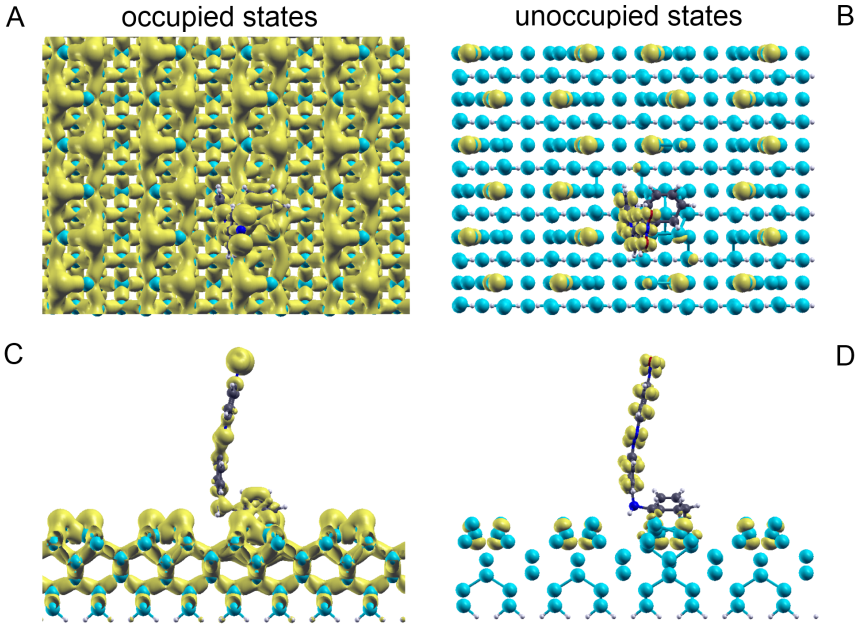

Figure 6.15: Calculated densities izocontours of the ***trans*****-standing configuration** - A - STM image, B - top view of model, C - side view of model.

neighboring dimers are shorter than the unperturbed ones with distances between Si atoms of 230 pm and 231 pm. The bond between zcarbon ring 1 and the amine group

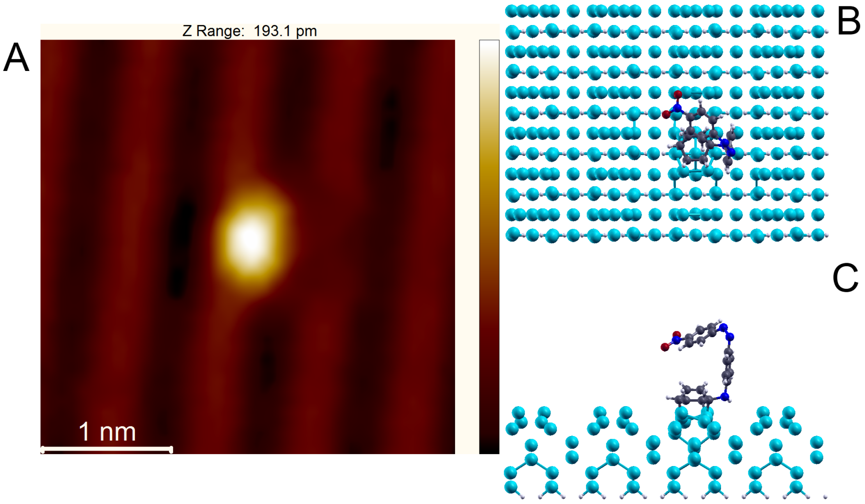

Figure 6.16: STM image and calculated model of the *cis*-standing configuration - A - STM image, B - top view of model, C - side view of model. Tunneling parameters: C - I_t=19 pA, U_t=2.2 V.

is stretched to 155 pm, and from the amine group to carbon ring 2 to 147 pm. The rest of the molecule is unchanged, up to 2 pm precision. The angle between carbon ring 1 and the carbon ring 2 is 95.8°. The adsorption energy is around 1 eV. Oxygen atoms are over 1400 pm over the Si surface. The calculated spatial distribution of the LDOS shows that the molecule has states on all of it but with a strong localization on the nitro group (see Figure 6.15), and therefore arises a question why the apparent height of the *trans*-standing molecule is only 200 pm? The answer lies in the weak transport along the molecule. This causes a small tunneling current signal and in effect the small apparent height of the molecule. Still while scanning with very small tunneling currents on the level of 10-20 pA, the tip does not hit the molecule.

There is a second version of the standing molecule with ab apparent height of 100 pm. Figure 6.16 shows the STM image and the calculated model of this so called *cis*-standing configuration. The same as in the case of the *trans*-standing configuration the molecule is bound to the surface by carbon ring number 1 in the tight-bridge configuration. The adsorption and its consequences on the surface's structure are the same. Also, the amine group and its bonding to the rest of the molecule are the same. The big difference is the conformational change of the azo bridge and as a consequence the position of carbon rings numbers 2 and 3 with respect to each other. The torque

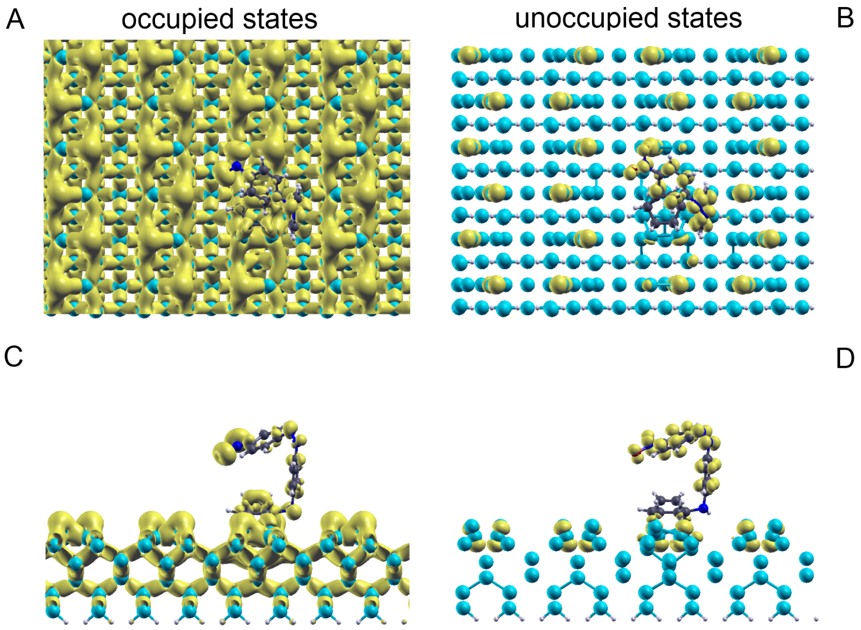

Figure 6.17: Calculated densities izocontours of the *cis*-standing configuration - A - STM image, B - top view of model, C - side view of model.

angle with respect to the azo bridge of both carbon rings is 18.5° compared to 21° for the gas phase *cis* isomer and 173.8° for the *trans*-standing isomer. The highest point of the molecule with respect to the silicon surface is the N atom in the azo bridge. The adsorption energy for this configuration of the molecule is 0.9 eV. Figure 6.17 shows the calculated spatial distribution of LDOS. The states are placed over the same atoms as in the *trans*-standing conformer, and therefore the difference in the apparent height in STM images is without doubt corresponding to the difference in the structure between *cis*-standing and *trans*-standing isomers.

In contradiction to the Cu(111) surface on Si(100) most molecules seem to be in *trans* conformation standing or lying flat.

6.5 The IETS of Single Molecules

As an assignment of 4-anilino-4'-nitroazobenzene models to STM images of molecules adsorbed on Cu(111) was done with a not well established method, I used STM-IETS measurements[42] in order to analyze the vibrational structure of the two forms. Because of the different configuration of the molecular groups with respect to the direction of the tunneling current, I expected different efficiencies of the modes. The IET spectroscopy over the physisorbed *cis* and *trans* forms show two peaks at around 20 meV and at around 40-50 meV in the measured energy range. A position dependent IETS gave results very similar with differences in the exact position of the peak at 40-50 meV and in their intensity. Figure 6.18 depicts spectra gathered above the center of both isomers as they are representative spectra showing both peaks with mean values and therefore can be used to compare both species. In order to recognize the vibrations, I cross correlated the obtained data with the data from other techniques and calculations (see table 6.1). The peak at 20 meV (161 cm^{-1}) is not in the table and therefore is not an internal but an external vibration. It represents the vibration of the whole molecule with respect to the Cu(111) surface. The peak at 50 meV (402 cm^{-1}) represents an internal vibration of the molecule. There are several possible vibrations such as ring C-C torsion 51 meV (412 cm^{-1}), ring C-C torsion, or out-of-plane C-H bending 63 meV(505 cm^{-1}). All three possibilities deform the carbon ring in an out-of-plane direction. This peak is present in the spectra gathered in almost any spot on the molecule, but its intensity is highest in the center of the molecule. Because the peak has its biggest intensity in the middle of the molecule, this confirms that in fact it results from the ring deformation.

The spectra of the *cis* and *trans* isomers differ in the width of the 20 meV peak (full width at half of the maxima: 20 meV on *cis* vs 14 meV on *trans*), in the change of the intensity of the 40-50 meV peak by 60%, and finally in the exact position of the 40-50 meV peak. The broader 20 meV peak measured with the same modulation parameters indicates that there are more energetically very similar vibrations. The *cis* form is indeed more complicated, with additional possibilities of external modes, while the *trans* 2D linear isomer has less possibilities of motion against the surface. To explain the 60% difference in intensity of the peak between the *cis* and *trans* forms I employ the propensity rules for the IETS proposed by Troisi and Ratner [19] saying that the most intense IET modes are associated with the vibrations that most effectively modulate the overall coupling among orbitals in contact with the electrodes (in this case the surface and the tip). Therefore, vibrations that occur in the z direction are those that modulate the transmition of the electrons through the molecule. The structural model presents differences in the angle between the carbon rings and the surface in both

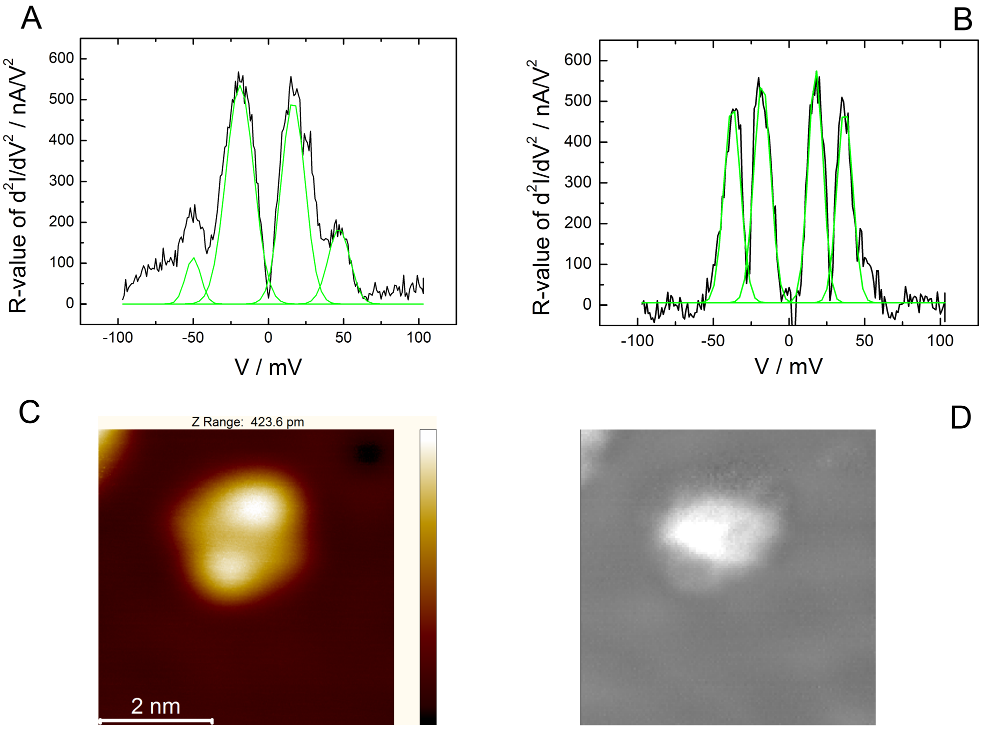

Figure 6.18: IETS of 4-anilino-4'-nitroazobenzene adsorbed on Cu(111) - A - IETS gathered over the center of the *cis* isomer, B - IETS gathered over the center of the *trans* isomer, C - STM image of the *trans* isomer, D - d^2I/dV^2 map gathered simultaneously with C at 21 meV. Tunneling parameters: C - I_t=69 pA, U_t=21 mV, lock-in parameters A, B, D - f=467Hz, A=20mV, t=30ms.

isomers. Thus, the change in the angle between the plane of the carbon ring and the normal to the surface, changes the z component of the out-of-plane ring deformation vibration, and as such the influence of this vibration on the modulation of the electron transition through the molecule reduces for the *cis* form.

The change in the IETS spectra based on geometry considerations thus confirms the interpretation of the STM images. I have thus established that two isomers of 4-anilino-4'-nitroazobenzene physisorb on the Cu(111) surface, if adsorbed at a low temperature. Thus, the molecules are weakly bonded to the substrate and the excitation induced by light might live long enough to trigger isomerization.

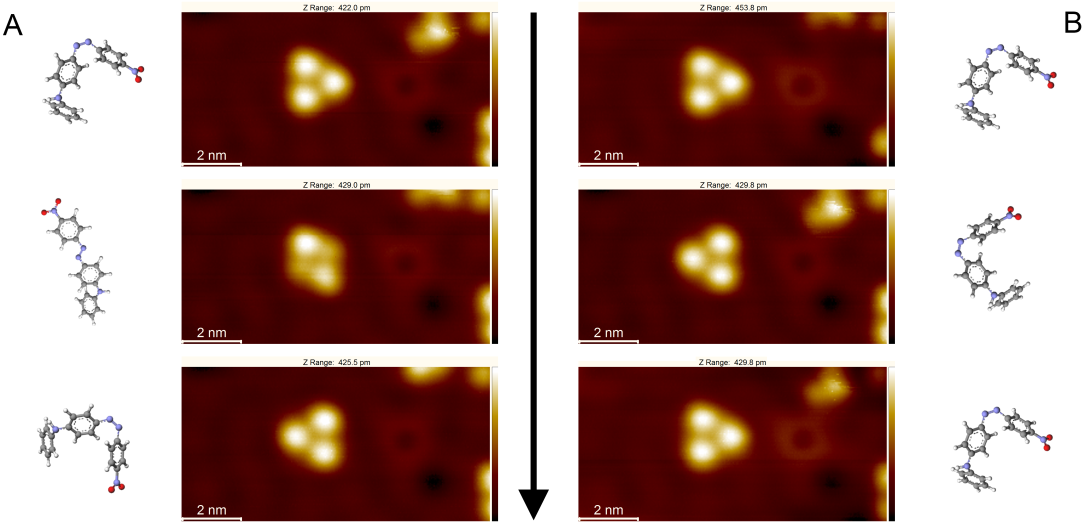

Figure 6.19: IET Manipulation - A - isomerization, B - rotation. Manipulation parameters: t=0.5 s U_M=230 mV, tunneling parameters: I_t=69 pA, U_t=100 mV

6.6 *Cis-Trans* Isomerization Induced by Light and Electrons

6.6.1 IET induced surface processes on Cu(111)

Now that it is clear how the molecules adsorb on the surface, it is time to check the possibility of the isomerization of single molecules. I used IET manipulation to check the possibility of electron induced isomerization. The energies used for these experiments ware in the energy range of < 150 meV,600 meV$>$. At first, the impulses were done over different parts of the molecule. As this does not influence the result in later experiments, impulses were done over the center of the molecule to minimize the effect of drift. Figure 6.19 depicts two series out of nearly 300 successful IET manipulations. Series A depicts the isomerization process, while series B depicts the apparent rotation of the molecule around its central point by 60 degrees. In fact, only angles of multiples of 60° are observed for this process. In isomerization reaction the molecule goes from a *cis* isomer to a *trans* isomer and back. In the I(t) curves, the current changes several times but the change is of the same order for the isomerization as for the apparent rotation. Comparing the first and last image of series A to the first and second image of series B suggests that the apparent rotation is in fact a

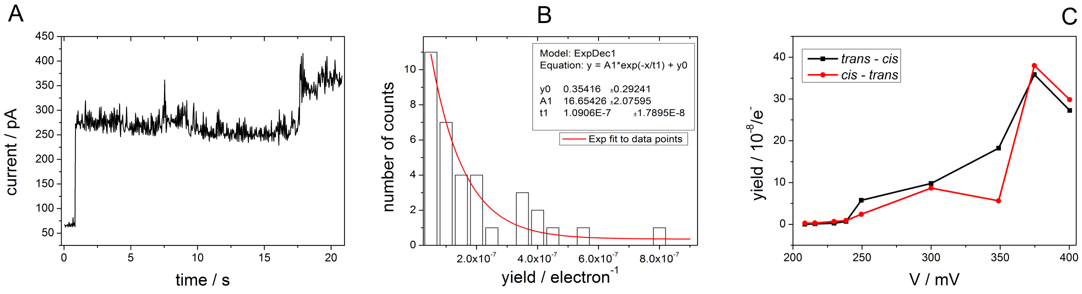

Figure 6.20: Yield - A - typical I(t) curve registered during manipulation, B - exponential fit determining the yield for selected bias, C - yield of electron induced isomerization

multiple isomerization. It is worth noticing that a reversible IET induced isomerization of azobenzene derivative has not yet been achieved on surfaces more reactive than Au(111). Looking at both series, it is obvious that isomerization is always accompanied by low range diffusion. Therefore, the 4-anilino-4'-nitroazobenzene physisorbed at the Cu(111) surface is not strictly bistable.

Figure 6.20 A depicts a typical I(t) curve for a single isomerization process. At a certain point there is a sudden change in the current indicating a reaction of a molecule. Integrating the current in the borders from the time of the start of the impulse to the time of change in the tunneling current, a cumulative charge is obtained and from this the number of electrons that tunneled before the process occurred. The yield of a process is reciprocal of the number of electrons necessary for one process. Figure 6.20 B shows the statistics for one energy. The value of yield for this one energy is deduced from the exponential decay of the number of observed processes with a certain yield. Doing this for each measured energy, I could plot the yield versus energy of the electrons' curve for the *cis* to *trans* isomerization process and back (see Figure 6.20 C). Analyzing those dependencies, I came to three conclusions. First, the *trans* to *cis* isomerization is more efficient and therefore the *cis* isomer is the more stable of the two at the Cu(111) surface. Second, there is no sharp threshold energy for the isomerization process. Third, the electron energies necessary to induce the process are much smaller than the energies of the photons. The first conclusion is consistent with the number of *cis* and *trans* isomers observed on the surface. The second and third together show that the isomerization process is not as well defined as in the gas phase. The first possibility here is that the IET induces isomerization at the surface and is a multi-electron process in which the necessary energy for the transition is gathered by pumping the molecules' energy through vibrational levels up to excited states. The second possibility is that the process is adiabatic and undergoes using only vibrational levels. In this case, a single electron could trigger the isomerization with a certain probability. This could be checked by performing IET manipulation at various starting tunneling currents. The difference in currents should cover at least 3 orders of magnitude i.e. 10 pA, 100 pA and 1 nA. The two first were used in the experiment, but scanning with tunneling currents above 100 pA was impossible as molecules diffused or dissociated from the surface because of the proximity of the STM tip. Therefore, there is no direct evidence of the isomerization pathway induced by the IET.

I also report that besides the two stable forms induced by IET manipulation several intermediate forms similar to the ones observed after adsorption at 25K are observed. They are not stable and change to one of the stable forms even during scanning within the typical parameters I_t=69 pA and V_t=100 mV. Furthermore, diffusion might be induced. However, single isomerization with a yield on the order of 10^{-7} $\bar{e}^{-1}$ is the dominating process in the energy range of 375-500 meV. This yield is comparatively one order of magnitude higher than the yield achieved on Au(111) [80]. This is a final indication of a weak coupling of the molecule to the Cu(111), i.e. physisorption.

6.6.2 IET induced surface processes on Si(100)

Although strong interactions with the substrate suggested that isomerization of the *trans*-flat configuration would be impossible, I tried IET manipulation method on both flat and standing molecular configurations. Choosing the energy of the manipulation, I was restricted to the polarization enabling detection of the tunneling current flow that is above the energy gap of the silicon. In principles there is no reason why I could not tunnel electrons to the molecule at lower energies; in fact, the electron that would tunnel to a molecule would be trapped there for a longer time and therefore the probability of isomerization would be much bigger, but the drawback would be that without the I(t) curves gathered (no tunneling current signal) I would be unable to say anything about the process. It would be probable that the STM tip would touch the molecule and alter its configuration by pure mechanical interaction. Therefore, I restricted the experiment to energies higher than the standard scanning bias. The molecules were exposed to electrons with energies as high as 5 eV. Apart from single unrepeatable events such as

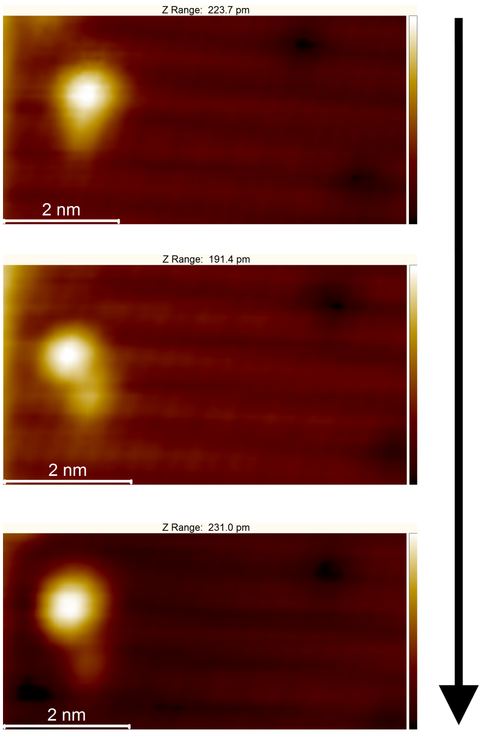

Figure 6.21: IET manipulation of 4-anilino-4'-nitroazobenzene on Si(100) - The series shows one of a few successful IET manipulations. Tunneling parameters: I_t=36 pA, U_t=2.5 V

the one presented in Figure 6.21 the 4-anilino-4'-nitroazobenzene did not react to the tunneling electrons otherwise than what looked like a chemical decomposition of the molecule.

In the case of the *trans*-flat configuration, the above decomposition is not surprising because the adsorption energy of this configuration is 9 eV, that is, much higher than the energy of any single bond in the molecule. Therefore, it is expected that the molecule would first break into pieces and only then would rearrange itself on the surface. However, in the case of the standing configuration of the molecule I expected to see the effect of the IET manipulation. In this case the azo bridge is intact and the molecule can isomerize between the *cis* and *trans* conformers without any external interactions. One explanation would be that the energetic electron does not stay on the molecule for long enough to induce the isomerization, but that would mean good conductance along the molecule and, in effect, a much bigger apparent height in the

STM images. Another explanation may be found in the geometry of the molecular orbitals responsible for the isomerization reaction. In all the reported isomerization reactions induced by IET, the molecules were laying almost flat. As a consequence, the π orbitals at the azo group were localized perpendicular to the surface, and in the γ direction of the DOS. In the standing forms of the molecule, the π orbitals at the azo group are parallel to the surface (see Figure 6.17 D); and this means that the band responsible for isomerization is dispersive. In consequence, the probability of electrons tunneling to this band is very low and the IET is ineffective.

6.6.3 Photoisomerization at the Cu(111) surface

After the IET induced isomerization experiments, I came to very challenging experiments with *in-situ* photoisomerization of single molecules adsorbed on Cu(111). The large-scale images in Figure 6.22 clearly show the same region of the surface before and after irradiation. In the small-scale images, a molecule is seen to reversibly switch from the *cis* isomer to the *trans* isomer and back again as a result of the irradiation. In this particular case, only one molecule was seen to isomerize in the observed area.

Overall, more than 600 molecules were exposed to the full spectrum of the lamp (1.1 W/cm^2 on the sample) for 20 minutes. This corresponds to a photon dose of 1×10^{20} cm^{-2}. 23 molecules (4% of the population) on the surface isomerize, and 3 (0.5% of the population) undergos multiple isomerization - observed as an apparent rotation.

As discussed in the introduction, there are several possibilities of adsorbed molecules isomerization. The first is direct photoisomerization in which the molecule absorbs the photon. This induces a transition from S_0 to S_N and in the relaxation process the molecule isomerizes by one of the known pathways. Second, the light heats up the surface and the adsorbed molecules. Heat is here the trigger for adiabatic transition from the *cis* to *trans*. In some cases when the *cis* is the ground state of the adsorbed molecule, the direction of heat driven isomerization can be the opposite. Finally, there is a surface mediated light-induced isomerization process. In this case there are still some different possibilities such as surface plasmon induced processes, or as in the case of TBA molecules on Au(111) [77], processes involving the photo-excitation of d-band electrons.

A simple annealing experiment prooves that the isomerization observed in my experiments is not heat driven. Referring to the conditions of the creation of surface

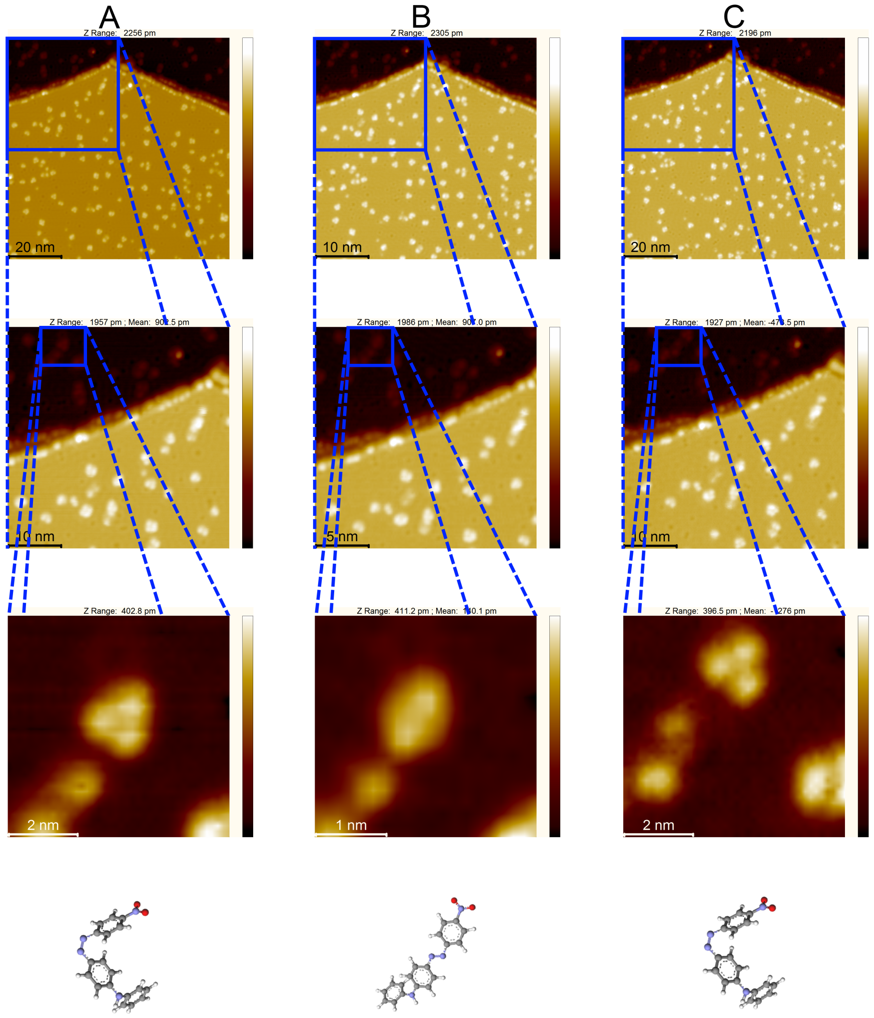

Figure 6.22: Photoisomerization of 4-anilino-4'-nitroazobenzene on the Cu(111) surface - STM images of molecules physisorbed on the Cu(111) surface A - before, B - after first, C - after second irradiation. Tunneling parameters: A, B, C - I_t=57 pA, U_t=100 mV, irradiation parameters: t=20', full spectrum of Hg lamp.

plasmons, ion saying that the light needs to be introduced to a metal surface via a material with relatively high refraction index [99–102] and knowing that a vacuum is not such a material, surface plasmon induced ismoerization is excluded. Finally, to determine if the process is surface mediated or direct, I used a BG-39 filter in a series of experiments. This filter transmits photons in the energy range from 330 nm to 600 nm, only. The Hg lamp emits lines of a width of ≈ 2 nm at the wavelengths around

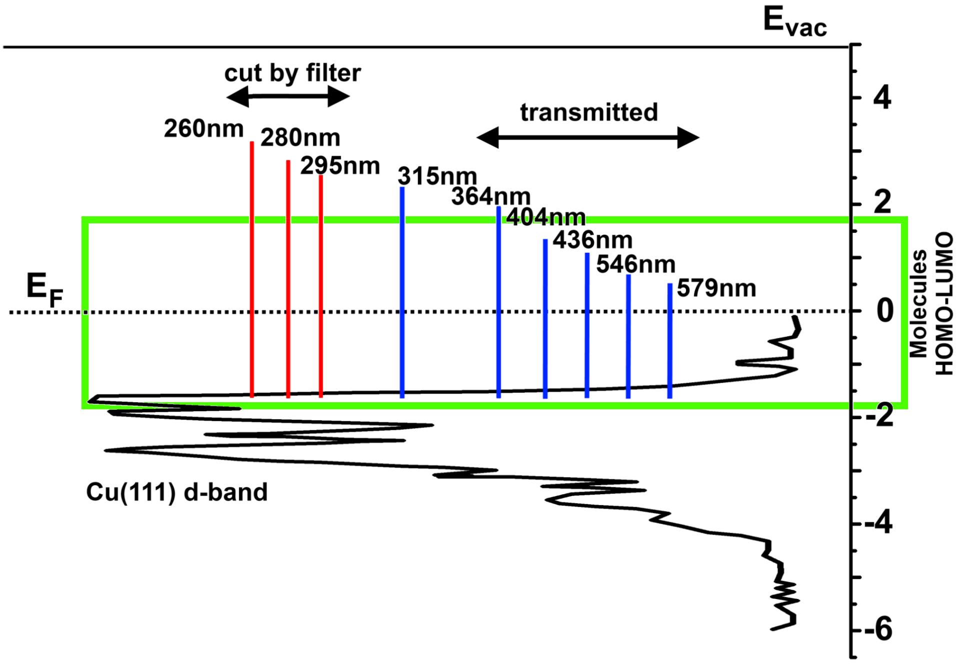

Figure 6.23: Photoisomerization energetic diagram - Schematic representation of the energy overlap of the Cu(111) d-band, the mercury lamp emission, the BG-39 filter transmittance, and the 4-anilino-4'-nitroazobenzene HOMO-LUMO gap

260 nm, 280 nm, 290-300 nm, 315 nm, 363 nm, 404 nm, 436 nm, 546 nm, and 579 nm, sketched in Figure 6.23. The filter blocks the lines at 260 nm, 280 nm and 290-300 nm completely, and the intensity of the line around 315 nm is reduced to 40%. All other lines are transmitted by 90%. Using the filter, no isomerization or rotation is observed even at elongated exposure tiimes. This excludes all wavelengths above 315 nm from being responsible for the isomerization shown in Figure 6.22. As the position of the d-bands of the Cu(111) is less than 2 eV below the Fermi energy (Figure 6.23), a substrate mediated process is excluded as it should be possible also with wavelengths transmitted by the filter that have energies between 3.76 eV and 2.07 eV.

In the gas phase, photoisomerization is induced by the transition of an electron either from the HOMO or the HOMO-1 orbital to the LUMO orbital corresponding to a $n - \pi^\star$ and a $\pi - \pi^\star$ transition, respectively. For 4-anilino-4'-nitroazobenzene the band related to the $n - \pi^\star$ has its absorption maximum at 435.5 nm (2.85 eV) and the $\pi - \pi^\star$ transition at 332 nm (3.73 eV). My filter experiment shows that isomerization

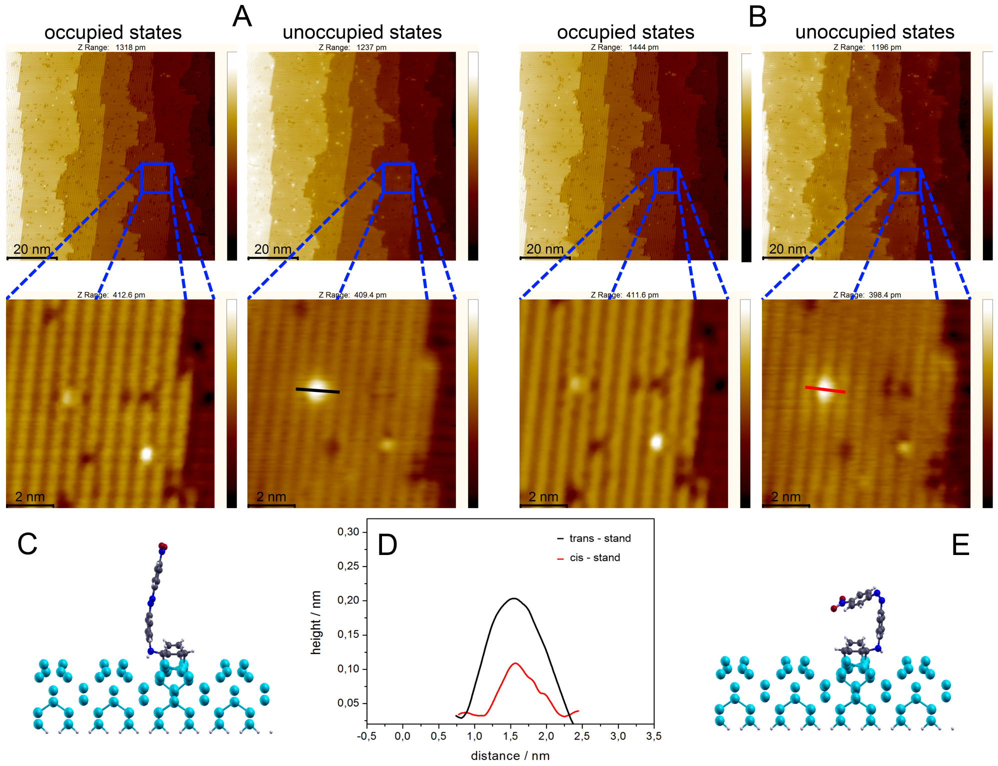

Figure 6.24: Photoisomerization of 4-anilino-4'-nitroazobenzene on the Si(100) surface - STM images of molecules chemisorbed on the Si(100) surface A - before, B - after irradiation, C and E show side view of the calculated model, D shows the profile lines taken from the STM images. Tunneling parameters: C - I_t=19 pA, $U_t = \pm 2.2$ V.

based on the $n - \pi^\star$ transition is quenched on the surface. The photoisomerization is thus initiated by the absorption of light in the absorption band covering 220 nm up to 350 nm and connected to the $\pi - \pi^\star$ transition. Note that this transition is followed by the rotation pathway of the isomerization around the double N bond of the azo group. Counting the apparent rotation as a double isomerization and considering that those photons that are transmitted by the BG-39 filter do not contribute to this isomerization, I calculate that the total effective cross section is 6×10^{-20} cm^{-2}. This is an order of magnitude higher than for a surface mediated isomerization of TBA adsorbed on Au(111) [103], but still two orders of magnitude lower than for isomerizations in liquid solutions.

6.6.4 Photoisomerization at the Si(100) surface

Finally, last but not least, we come to the *in-situ* photoisomerization of single molecules adsorbed on the Si(100) surface. According to the DFT calculation, the *trans*-flat configuration is too strongly bound to the substrate to be able to isomerize. This is also true in the experiments. The standing configurations were much more promising but failed in the IET manipulation experiment. In the photoisomerization experiments, however, standing configurations do isomerize. To know the influence of the surface, the experiments have to be made on single, well separated molecules. Remembering that standing configurations are only 11% of the population in the mesurement window, there were on average 20 molecules. I used three time periods of irradiation 180', 300' and 600'. In the case of 180' and 600', only the *trans* to *cis* isomerization occured; while in the case of the 300' irradiation the isomerization ratio of *trans* to *cis* and *cis* to *trans* were equal. 27 out of 160 irradiated molecules isomerized, giving the total effective cross section for the isomerization of 1.6×10^{-21} cm^{-2}. Standing configurations have the azobenzene part of the molecule intact, both geometricaly and electronicaly, and therefore the same possibilities of pathways as for the gas phase molecules are valid. The effective cross section is smaller than for the molecules physisorbed on Cu(111), similarly as for the molecules chemisorbed on gold [80] and bigger than for molecules adsorbed on thin insulating film [104].

Concluding the isomerization attempts a few main points arise. First, the geometry of the surface is drastically different. Both the interatomic distances and symmetry are vary between the samples. Therefore, any balance between molecular function groups established on metal substrate will most probably change, or completely diminish on silicon or germanium surfaces. Second, the LDOS of surfaces is also different. Cu(111) just like Au(111) is a d-electron system (as regards the dominance of bands in the proximity of the Fermi level) while Si(100) is a p-electron system. As a consequence, there is the probability of chemisorption changes - p-electron systems such as azobenzene derivatives will chemisorb on a p-electron surface such as Si(100). Also, isomerization reaction mechanisms varies depending on the overlap of molecule's HOMO-LUMO gap with the surface's d-band. The geometry of adsorption configuration determines the probability of IET induced isomerization. The in-plane configurations are IET active if the bonding to the substrate is weak enough. The out-of-plane configurations are IET inactive.

Chapter 7

Conclusions

Concluding the thesis. All five tasks were accomplished. Namely:

- A new UHV system was designed and built in Poznan. This system is capable of clean metal and semiconductor surfaces investigation. The system is equipped with an ion gun and different methods of samples annealing necessary for various materials preparation. The chosen pumping system configuration enables work in a 1×10^{-10} mbar range. The system is built in such a way that the stability of the STM is maximized.

- 4-anilino-4'nitroazobenzene molecules were throughout characterized using macroscopic methods. Vibration modes of the molecule were measured using IR and Raman spectroscopies. The absorption spectra in the solid state as well as in solution were measured, and S_0 to S_1 and S_0 to S_2 transitions were recognized. The reaction speed and the lifetime of excited states were measured by means of flash photolysis.

- Clean Si(100) and Cu(111) surfaces were characterized by means of the STM and DFT.

- Single molecules were deposited onto Si(100) and Cu(111) surfaces. Adsorption configurations were recognized using the STM, calculations, IETS, and STS. A Cu(111) surface, being mainly a d-electron system, induced physisorption of a mainly p-electron system, which is the 4-anilino-4'-nitroazobenzene. A Si(100) surface being mainly a p-electron system, induced chemisorption of the molecule.

Nevertheless, on both surfaces there are configurations with an azo group intact, capable of isomerization.

- Isomerization reactions were induced on both surfaces. On Cu(111) the IET induced isomerization was very effective in the low energy range. Direct photoisomerization was also achieved with comparably high cross sections. The isomerization is accompanied by a low range diffusion, therefore the switch is not strictly bistable. On the Si(100) only standing configurations were capable of switching. The photoisomerization was achieved with a cross section lower by an order of magnitude than for molecules adsorbed on the Cu(111) surface. The advantage of isomerization on Si(100) is that the molecules are strongly bound to the surface and therefore do not diffuse during the isomerization. The photoswitch on the Si(100) surface is therefore bistable.

Transferring molecules from metals to semiconductors, two main aspects must be accounted for:

- differences in surface geometry,
- differences in surface's LDOS.

Apprendix 1

Here are the details of the UHV chamber construction. A system setup I have designed and built is based on several principles:

- three stage sample introduction system,
- separation of preparation and analysis chambers,
- ultimate pressure in analysis chamber,
- compatibility with organic molecules experiments.

The design was also limited by some technical parameters of equipment adapted from the old system, namely:

- length of main transfer manipulator,
- SPM chamber dimensions,
- sample carrier dimensions,
- sizes and pumping efficiency of vacuum pumps.

The evaporators are placed in such a way that crucibles can also be used for evaporation. The bakeout of the system is carried out using the automated heaters under the tent and a two stage control. First stage is controlling the temperature and providing the power to the heaters, second stage is a emergency switch off of the bakeout unit.

Ra 0.02

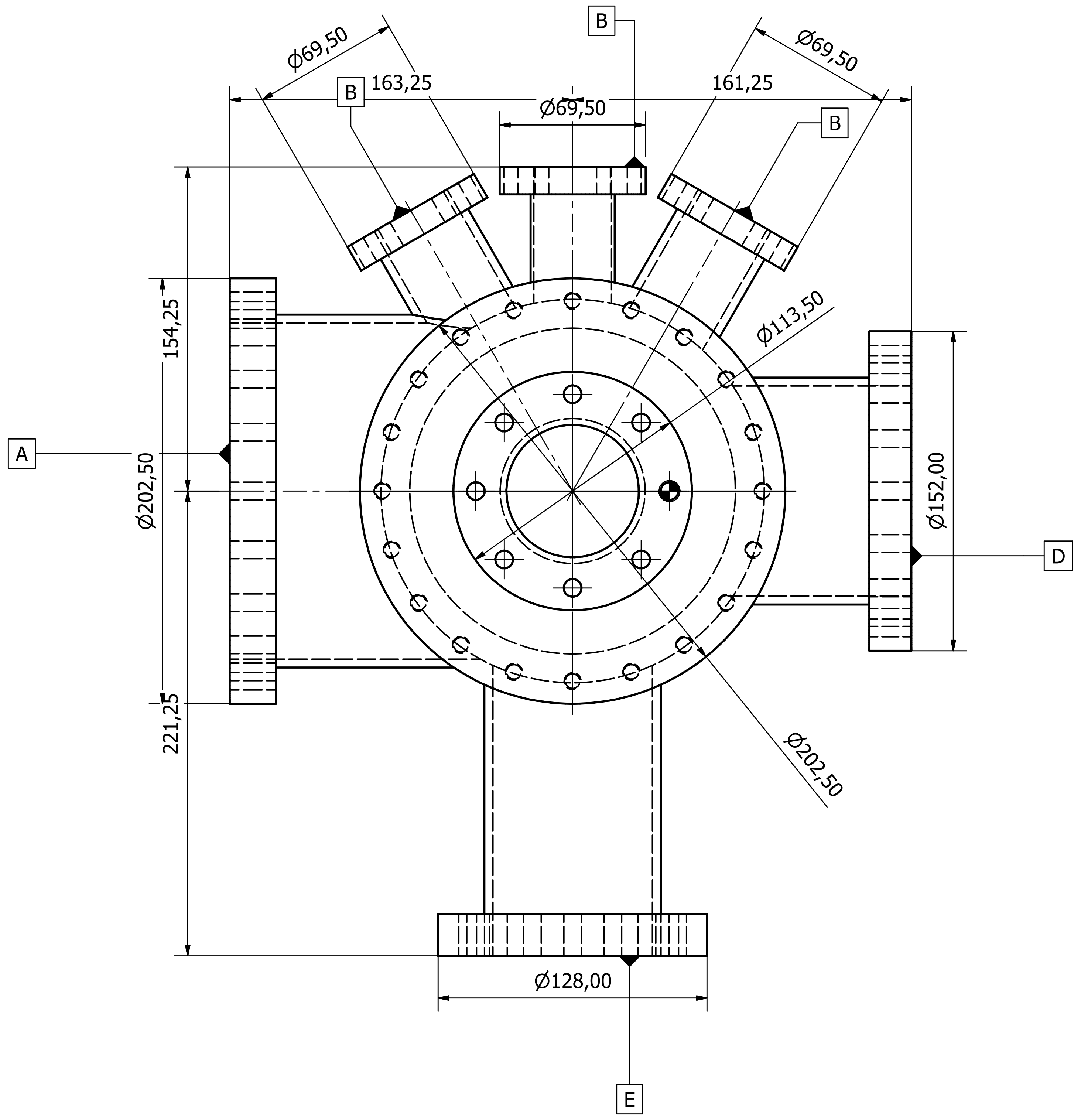

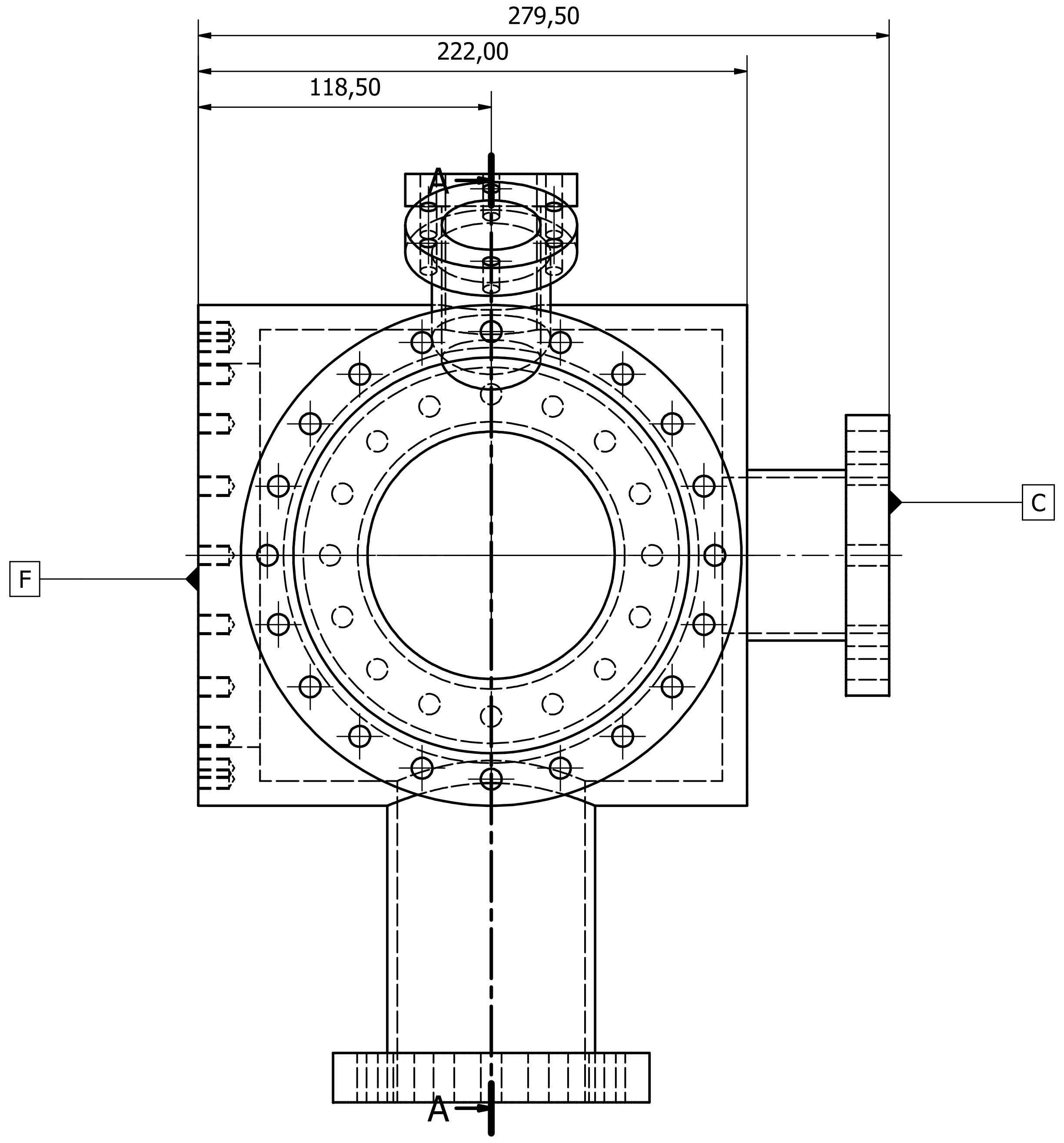

A-A (1 : 2)

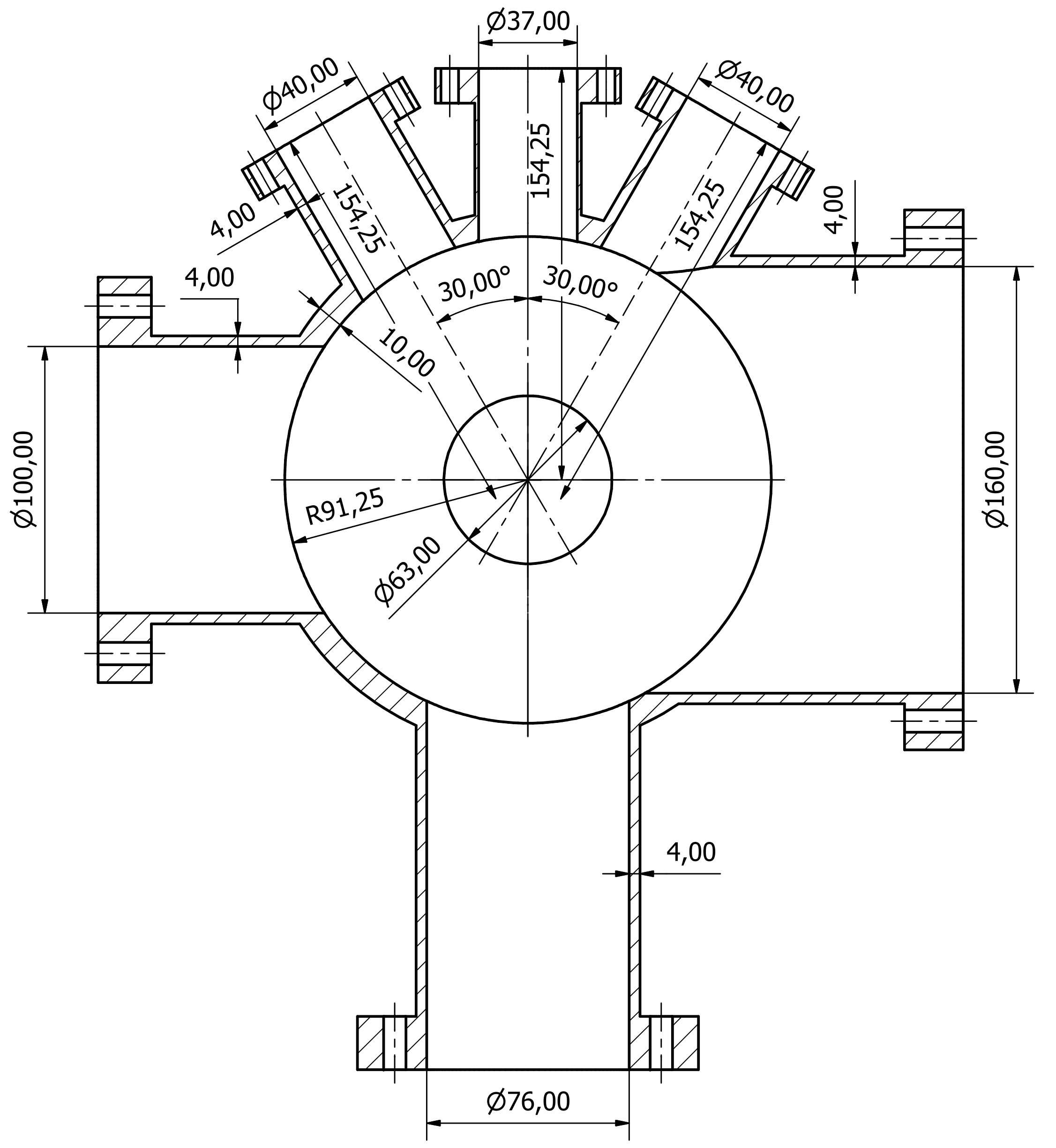

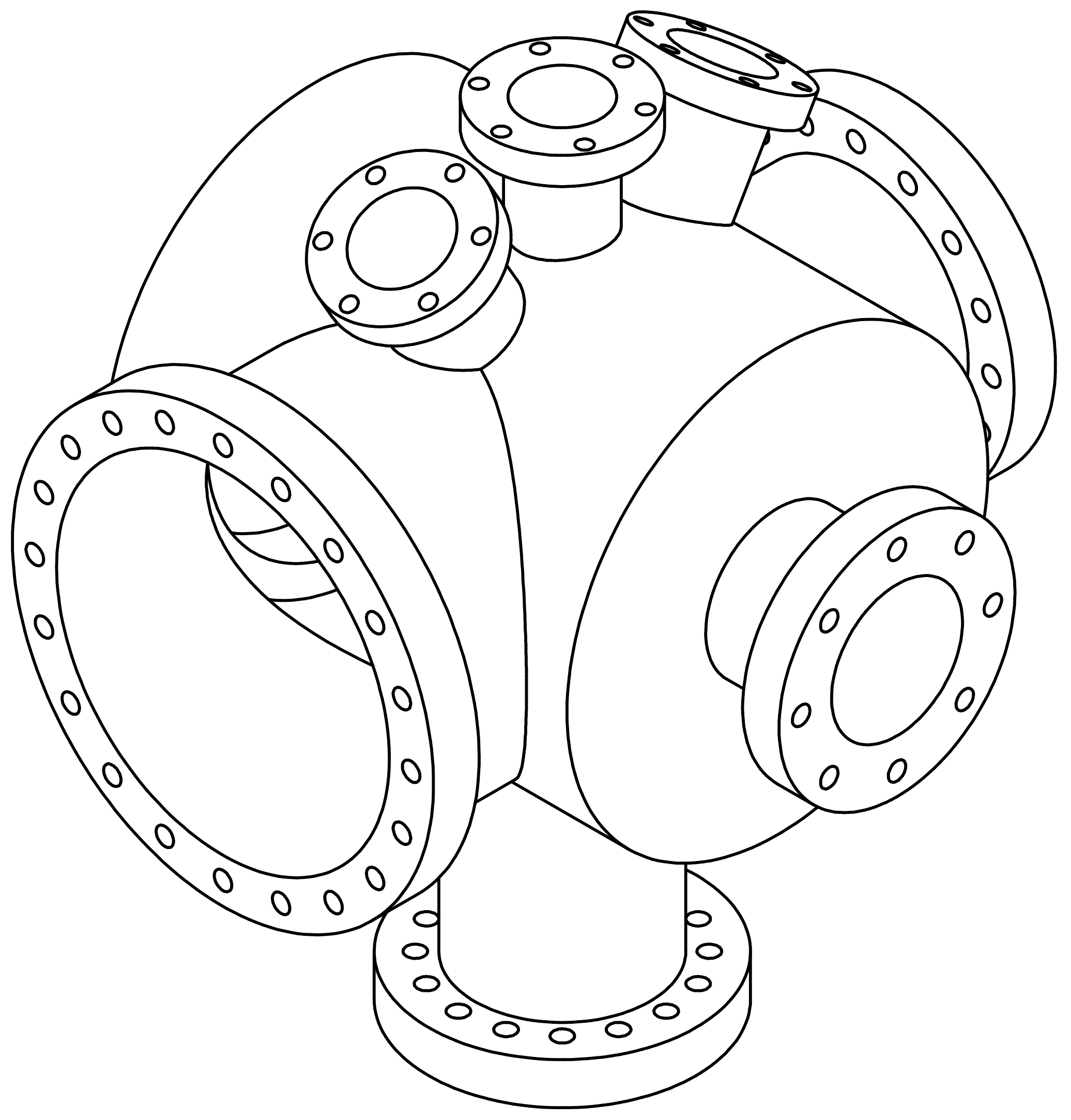

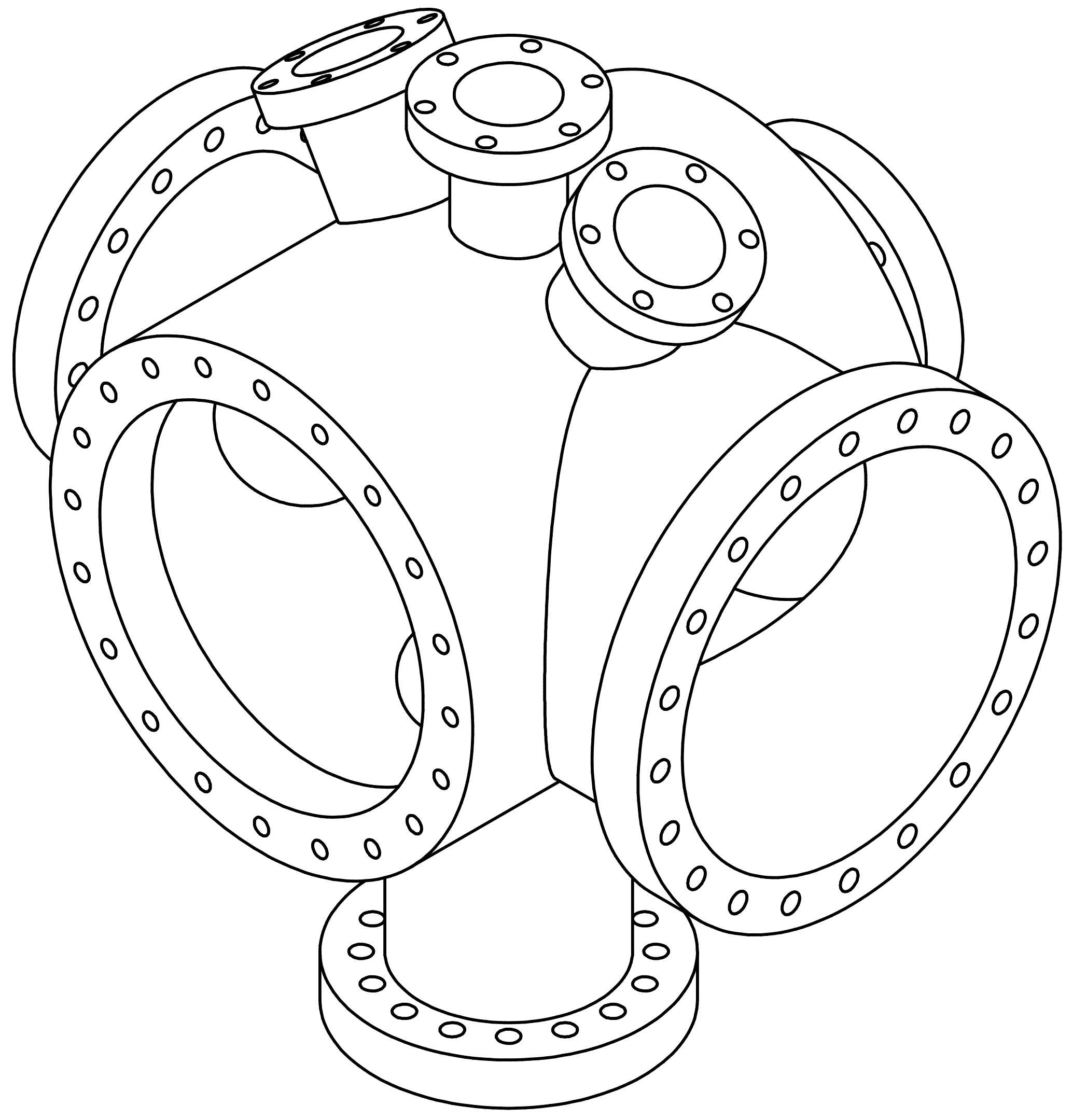

TABELA		
Id.	Quantity	Name
A	1	DN - 160CF
B	3	DN - 40CF
C	1	DN - 63CF
D	1	DN - 100CF
E	1	DN - 76CF
F	1	DN - 160CF inside

Zaprojektowany przez	Sprawdzony przez	Zatwierdzony przez	Data	Data	
Maciej Bazarnik	Maciej Bazarnik	Ryszard Czajka			

Institute of Physics, Poznan
University of Technology

Analyzis chamber

01

Wydanie

Arkusz
1 / 1

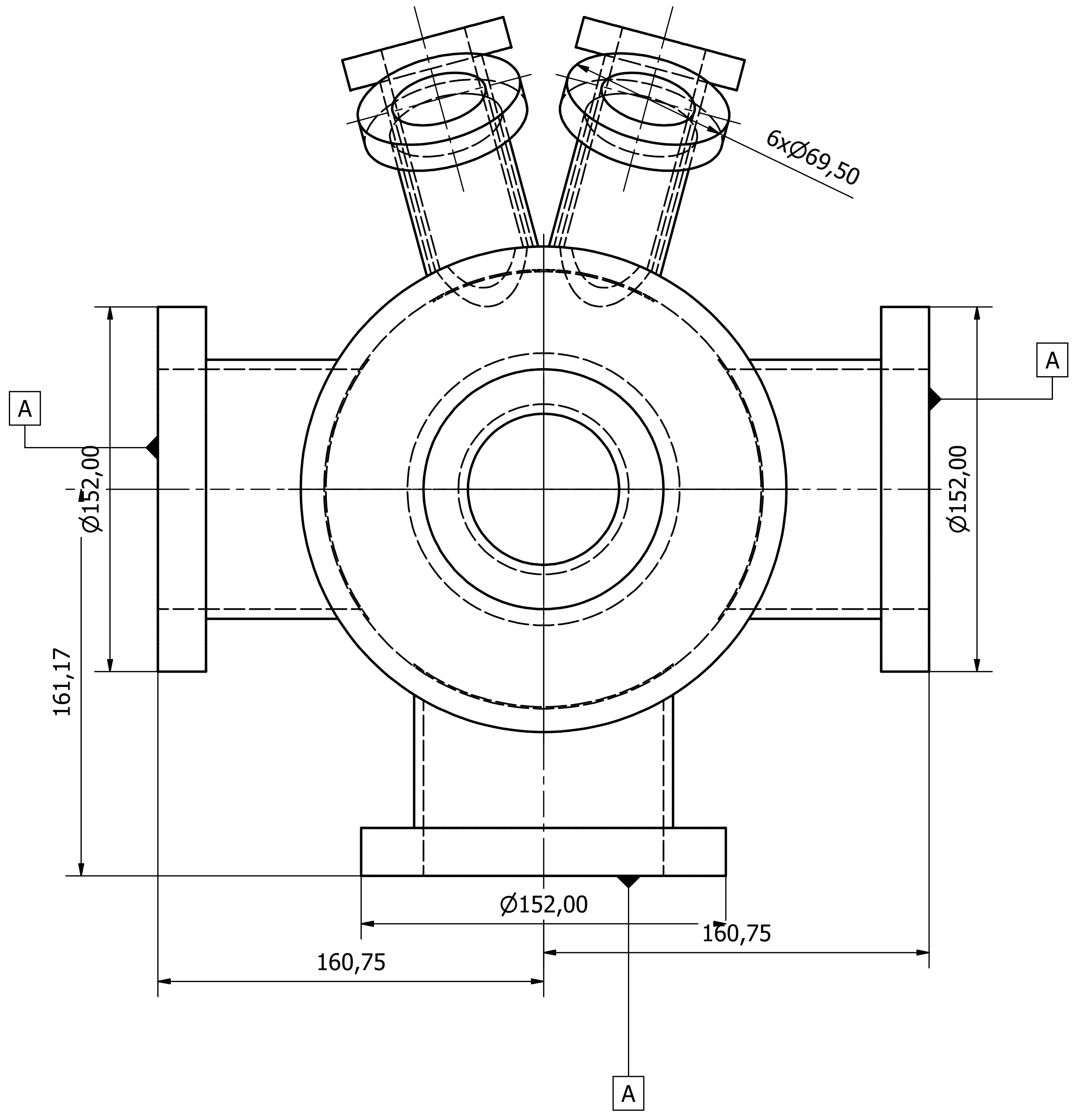

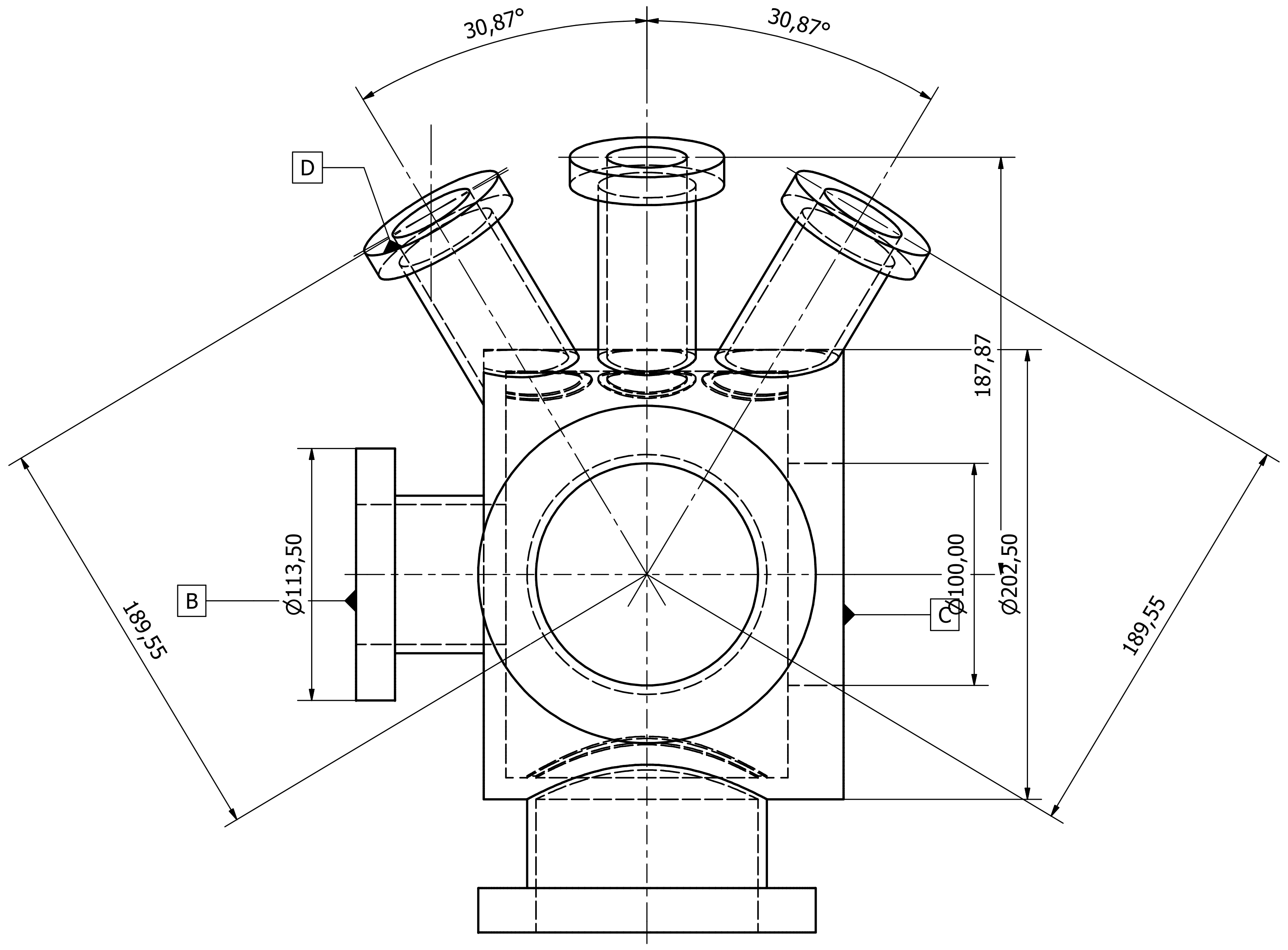

Ra0.02 (✓)

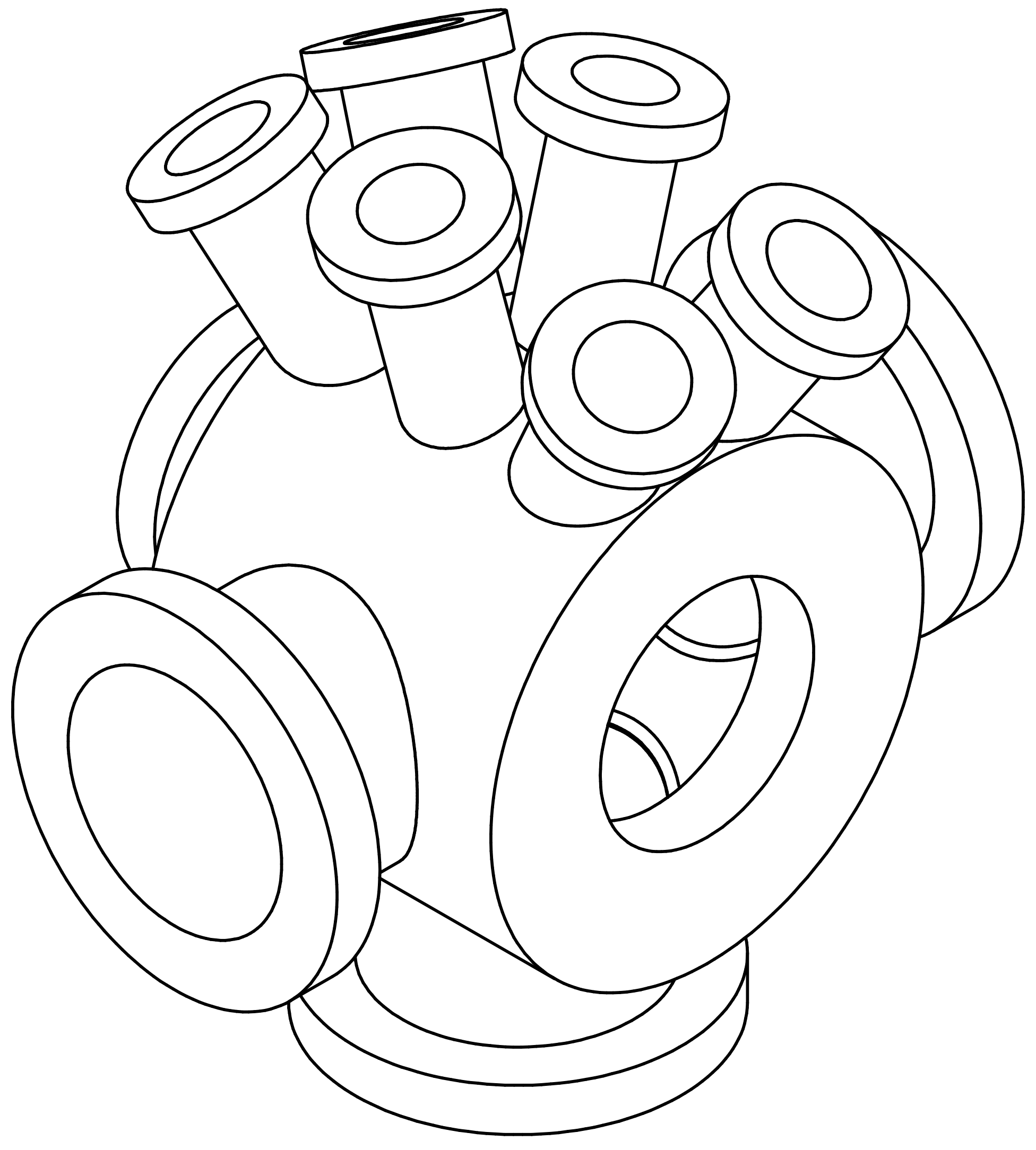

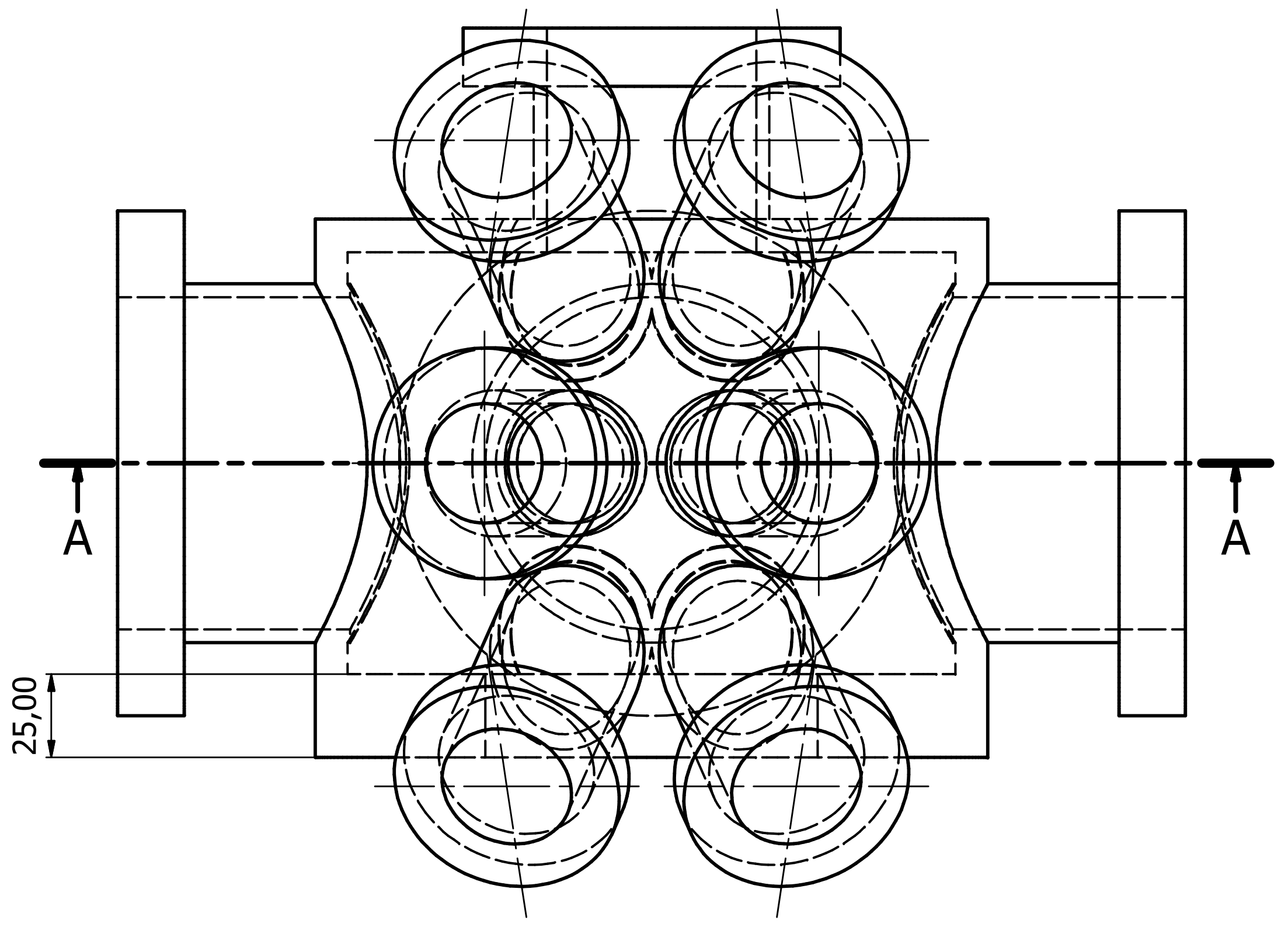

A-A (1 : 2)

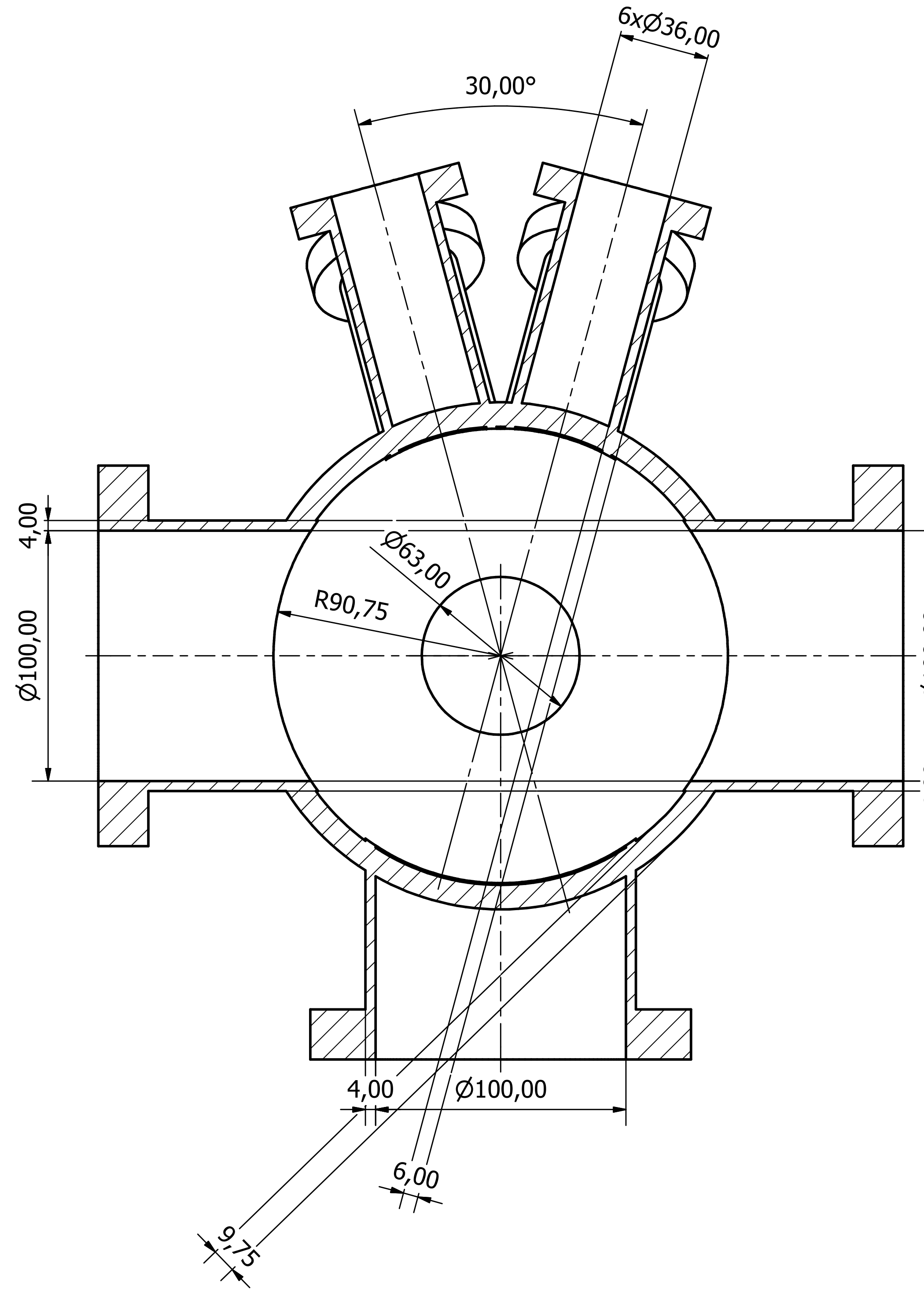

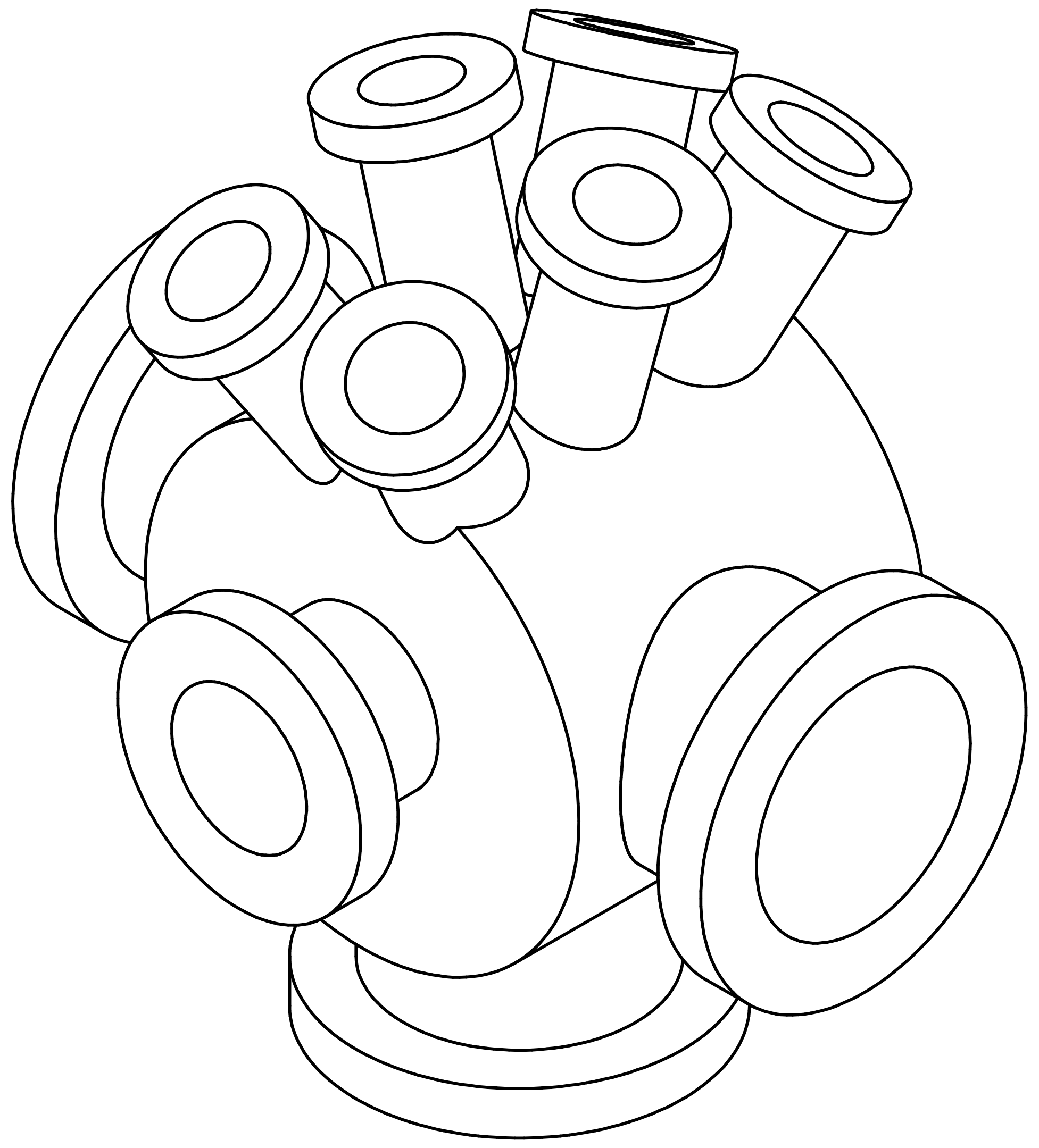

TABELA		
Id.	Quantity	Name
A	3	DN - 100CF
B	1	DN - 63CF
C	1	DN - 100CF inside
D	6	DN - 40CF

Zaprojektowany przez	Sprawdzony przez	Zatwierdzony przez	Data	Data
Maciej Bazarnik	Maciej Bazarnik	Ryszard Czajka		

Institute of Physics, Poznan
University of Technology

Preparation chamber

02

Wydanie

Arkusz
1 / 1

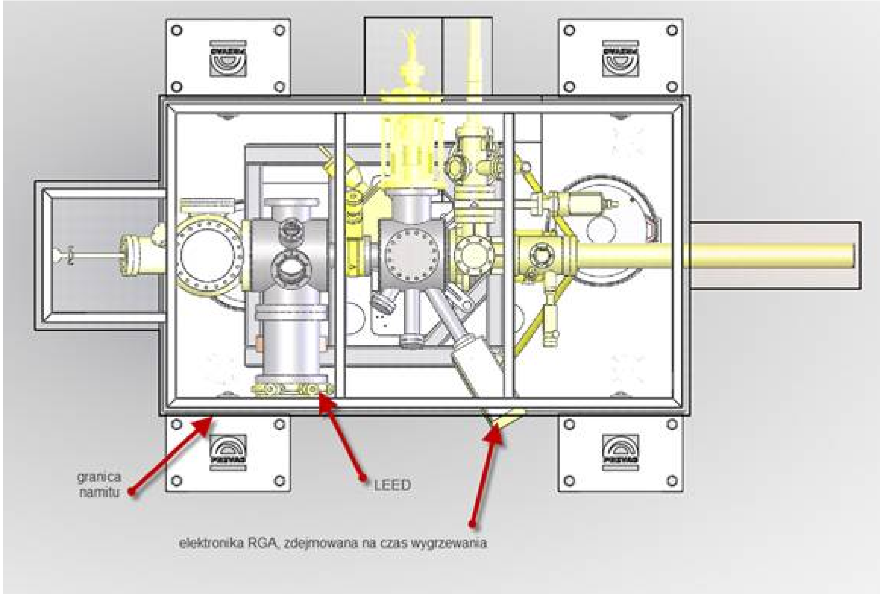

Figure 7.1: Top view of a design's computer simulation - In yellow color parts of the old system.

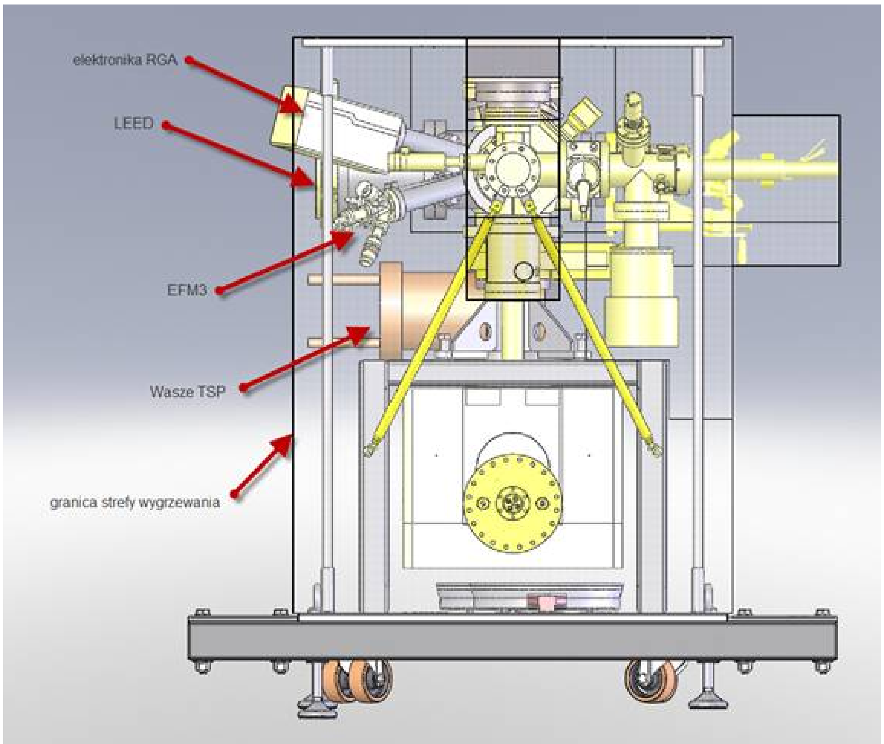

Figure 7.2: Side view of a design's computer simulation - In yellow color parts of the old system.

References

[1] G. Binnig and H. Rohrer. **Scanning tunneling microscopy**. *Helvetica Physica Acta*, **55**:726, 1982. 2

[2] G. Binnig, C.F. Quate, and Ch Gerber. **Atomic Force Microscope**. *Physical Review Letters*, **56**(9):930–933, March 1986. 2

[3] K.S. Birdi. *Scanning Probe Microscopes: Applications in Science and Technology.* CRC Press, London, 2003. 2

[4] C. Kittel. *Introduction to Solid State Physics.* Wiley, New York, 2004. 6

[5] D. Feng and G. Jin. *Introduction to Condensed Matter Physics.* World Scientific Pub. Co. Inc., 2005. 6

[6] J. Tersoff and D. R. Hamann. **Theory of scanning tunneling microscope**. *Physical Review B*, **31**(2):805, 1985. 6, 7

[7] J. Bardeen. **Tunnelling from a Many-Particle Point of View**. *Physical Review Letters*, **6**(2):57–59, January 1961. 6

[8] P. Grütter, W. Hofer, and F. Rosei, editors. *Properties Of Single Organic Molecules On Crystal Surfaces.* Imperial College Press, London, 2006. 8

[9] T. Holstein. **Studies of polaron motion**. *Annals of Physics*, **8**(3):343–389, November 1959. 8

[10] J. Bonča and S.A. Trugman. **Effect of inelastic processes on tunneling**. *Physical review letters*, **75**(13):2566–2569, 1995.

[11] E. Emberly and G. Kirczenow. **Landauer theory, inelastic scattering, and electron transport in molecular wires**. *Physical Review B*, **61**(8):5740–5750, February 2000.

[12] A.J. Heeger, S. Kivelson, J.R. Schrieffer, and W.P. Su. **Solitons in conducting polymers**. *Reviews of Modern Physics*, **60**(3):781, 1988.

[13] Z. Yu, D. Smith, A. Saxena, and A. Bishop. **Green's function approach for a dynamical study of transport in metal/organic/metal structures**. *Physical Review B*, **59**(24):16001–16010, June 1999.

[14] H. Ness, S. Shevlin, and a. Fisher. **Coherent electron-phonon coupling and polaronlike transport in molecular wires**. *Physical Review B*, **63**(12):1–16, March 2001. 8

[15] N. Mingo and K. Makoshi. **Calculation of the inelastic scanning tunneling image of acetylene on Cu(100)**. *Physical review letters*, **84**(16):3694–7, April 2000. 8

[16] N. Lorente, M. Persson, L. Lauhon, and W. Ho. **Symmetry Selection Rules for Vibrationally Inelastic Tunneling**. *Physical Review Letters*, **86**(12):2593–2596, March 2001. 8

[17] N. Mingo and K. Makoshi. **Excitation of vibrational modes of adsorbates with the scanning tunneling microscope: many-orbital theory**. *Surface Science*, **438**(1-3):261–270, September 1999. 8

[18] A. Troisi, M.A. Ratner, and A. Nitzan. **Vibronic effects in off-resonant molecular wire conduction**. *The Journal of Chemical Physics*, **118**(13):6072, 2003. 8

[19] A. Troisi and M.A. Ratner. **Propensity rules for inelastic electron tunneling spectroscopy of single-molecule transport junctions.** *The Journal of chemical physics*, **125**(21):214709, December 2006. 9, 10, 72

[20] A. Troisi and M.A. Ratner. **Molecular transport junctions: Propensity rules for inelastic electron tunneling spectra.** *Nano letters*, **6**(8):1784–8, August 2006. 8, 9, 10

[21] L. Piela. *Idee chemii kwantowej.* Wydawnictwo Naukowe PWN, Warszawa, 2006. 11, 12

[22] S. Cottenier. *Density Functional Theory and the Family of (L)APW-methods: a step-by-step introduction.* K.U.Leuven, 2002. 11, 12, 14

[23] P. Hohenberg and W. Kohn. **Inhomogeneous Electron Gas**. *Physical Review*, **136**(3B):B864–B871, November 1964. 11

[24] W. Kohn and L.J. Sham. **Self-consistent equations including exchange and correlation effects**. *Physical Review*, **140**(4A):A1133–A1138, 1965. 12

[25] A.D. Becke. **Density-functional exchange-energy approximation with correct asymptotic behavior**. *Physical Review A*, **38**(6):3098–3100, September 1988. 12

[26] Chengteh Lee, Weitao Yang, and Robert G. Parr. **Development of the Colle-Salvetti correlation-energy formula into a functional of the electron density**. *Physical Review B*, **37**(2):785–789, January 1988.

[27] J. Perdew, J. Chevary, S. Vosko, K. Jackson, M. Pederson, D. Singh, and C. Fiolhais. **Atoms, molecules, solids, and surfaces: Applications of the generalized gradient approximation for exchange and correlation**. *Physical Review B*, **46**(11):6671–6687, September 1992.

[28] J. Perdew, K. Burke, and M. Ernzerhof. **Generalized Gradient Approximation Made Simple.** *Physical review letters*, **77**(18):3865–3868, October 1996. 12

[29] M.J.S. Dewar. *The Molecular Orbital Theory of Organic Chemistry*. McGrawHill, New York, 1969. 13

[30] J.A. Pople and D.L. Beveridge. *Approximate Molecular Orbital Theory*. Academic Press, New York, 1970.

[31] J.N. Murrell and A.J. Harget. *Semiempirical Self-Consistent-Field Molecular Orbital Theory of Molecules*. New York, 1972.

[32] T. Clark. *A Handbook of Computational Chemistry*. Wiley, New York, 1985.

[33] J.J. Stewart. **MOPAC: a semiempirical molecular orbital program.** *Journal of computer-aided molecular design*, **4**(1):1–105, March 1990. 13, 14

[34] J.J. Stewart. **Optimization of parameters for semiempirical methods IV : extension of MNDO , AM1 , and PM3 to more main group elements**. *Journal of Molecular Modeling*, pages 155–164, 2004. 13, 14

[35] M.J.S. Dewar and W. Thiel. **Ground states of molecules. 38. The MNDO method. Approximations and parameters**. *Journal of the American Chemical Society*, **99**(15):4899–4907, June 1977. 13

[36] M.J.S. Dewar and W. Thiel. **Ground states of molecules. 39. MNDO results for molecules containing hydrogen, carbon, nitrogen, and oxygen**. *Journal of the American Chemical Society*, **99**(15):4907–4917, June 1977. 14

[37] J.J. Stewart. **Optimization of parameters for semiempirical methods I. Method**. *Journal of Computational Chemistry*, **10**(2):209–220, March 1989.

[38] J.J. Stewart. **Optimization of parameters for semiempirical methods II. Applications**. *Journal of Computational Chemistry*, **10**(2):221–264, March 1989. 13, 14

[39] R.T. Morrison and R.N. Boyd. *Chemia organiczna*. Wydawnictwo Naukowe PWN, Warszawa, v edition, 1998. 14, 15

[40] J. Dokić, M. Gothe, J. Wirth, M.V. Peters, J. Schwarz, S. Hecht, and P. Saalfrank. **Quantum chemical investigation of thermal cis-to-trans isomerization of azobenzene derivatives: substituent effects, solvent effects, and comparison to experimental data.** *The journal of physical chemistry. A*, **113**(24):6763–73, June 2009. 15, 16

[41] N. Tamai and H. Miyasaka. **Ultrafast Dynamics of Photochromic Systems.** *Chemical reviews*, **100**(5):1875–1890, May 2000. 16, 46, 47

[42] W. Ho. **Single-molecule chemistry**. *The Journal of Chemical Physics*, **117**(24):11033, 2002. 21, 22, 71

[43] M. Persson. **Theory of elastic and inelastic tunnelling microscopy and spectroscopy: CO on Cu revisited.** *Philosophical transactions. Series A, Mathematical, physical, and engineering sciences*, **362**(1819):1173–83, June 2004. 22

[44] F.A. Settle, editor. *Handbook of Instrumental Techniques for Analytical Chemistry.* Prentice-Hall, New York, 1997. 26

[45] R. G. W. Norrish and G. Porter. **Chemical Reactions Produced by Very High Light Intensities**. *Nature*, **164**(4172):658–658, October 1949. 28, 29

[46] S.R. Hair, G.A. Taylor, and L.W. Schultz. **An easily implemented flash photolysis experiment for the physical chemistry laboratory: The isomerization of 4-anilino-4'-nitroazobenzene**. *Journal of Chemical Education*, **67**(8):709, August 1990. 28, 29, 58

[47] M.A. Thompson. **ArgusLab**. 30

[48] H. Gawronski, J. Henzl, V. Simicmilosevic, and K. Morgenstern. **Using a chemical concept for reactivity for the interpretation of STM images of physisorbed molecules**. *Applied Surface Science*, **253**(23):9047–9053, September 2007. 32, 62

[49] J. Rowe and N. Smith. **Photoemission spectra and band structures of d-band metals. V. The (100) and (111) faces of single-crystal copper**, October 1974. 41

[50] T. Yokoyama and K. Takayanagi. **Anomalous flipping motions of buckled dimers on the Si(001) surface at 5 K**. *Physical Review B*, **61**:5078–5081, February 2000. 42, 43

[51] Y. Kondo, T. Amakusa, M. Iwatsuki, and H. Tokumoto. **Phase transition of the Si(001) surface below 100 K**. *Surface Science*, **453**:L318–L322, May 2000. 42, 43

[52] K. Hata, S. Yoshida, and H. Shigekawa. **p(2x2) Phase of Buckled Dimers of Si(100) Observed on n-Type Substrates below 40 K by Scanning Tunneling Microscopy**. *Physical Review Letters*, **89**(28):2–5, December 2002. 43

[53] H. Rau. **Further evidence for rotation in the π,π* and inversion in the n,π* photoisomerization of azobenzenes**. *Journal of Photochemistry*, **26**(2-3):221–225, August 1984. 46

[54] P. Bortolus and S. Monti. **Cis-trans photoisomerization of azobenzene. Solvent and triplet donors effects**. *The Journal of Physical Chemistry*, **83**(6):648–652, March 1979. 46

[55] H. Rau and E. Lueddecke. **On the rotation-inversion controversy on photoisomerization of azobenzenes. Experimental proof of inversion**. *Journal of the American Chemical Society*, **104**(6):1616–1620, March 1982.

[56] G. Zimmerman, L.-Y. Chow, and U.-J. Paik. **The Photochemical Isomerization of Azobenzene**. *Journal of the American Chemical Society*, **80**:3528, 1958.

[57] D. Gegiou, K.A. Muszkat, and E. Fischer. **Temperature dependence of photoisomerization. V. Effect of substituents on the photoisomerization of stilbenes and azobenzenes**. *Journal of the American Chemical Society*, **90**(15):3907–3918, July 1968.

[58] Shmuel Malkin and Ernst Fischer. **TEMPERATURE DEPENDENCE OF PHOTOISOMERIZATION. PART II.1 QUANTUM YIELDS OF cis â‡† trans ISOMERIZATIONS IN AZO-COMPOUNDS**. *Journal of Physical Chemistry*, **66**(12):2482–2486, December 1962. 46

[59] S. Monti, A. Energia, G. Orlandi, and P. Palmieri. **FEATURES OF THE PHOTOCHEMICALLY ACTIVE STATE SURFACES OF AZOBENZENE**. *Chemical Physics*, **71**:87–99, 1982. 46, 47

[60] C. Angeli, R. Cimiraglia, and H.-J. Hofmann. **On the competition between the inversion and rotation mechanisms in the cis-trans thermal isomerization of diazene**. *Chemical Physics Letters*, **259**:276–282, September 1996. 47

[61] Igor K. Lednev, Tian-Qing Ye, Ronald E. Hester, and John N. Moore. **Femtosecond Time-Resolved UV-Visible Absorption Spectroscopy of trans -Azobenzene in Solution**. *The Journal of Physical Chemistry*, **100**:13338–13341, January 1996. 47

[62] T. Nagele, R. Hoche, W. Zinth, and J. Wachtveitl. **Femtosecond photoisomerization of cis-azobenzene**. *Chemical Physics Letters*, **272**:489–495, July 1997.

[63] J. Wachtveitl, T. Nägele, B. Puell, W. Zinth, M. Krüger, S. Rudolph-Böhner, D. Oesterhelt, and L. Moroder. **Ultrafast photoisomerization of azobenzene compounds**. *Journal of Photochemistry and Photobiology A: Chemistry*, **105**:283–288, May 1997.

[64] J. Azuma, N. Tamai, A. Shishido, and T. Ikeda. **Femtosecond dynamics and stimulated emission from the S2 state of a liquid crystalline trans-azobenzene**. *Chemical Physics Letters*, **288**:77–82, May 1998. 47

[65] I.K. Lednev, T.-Q. Ye, M. Towrie, P. Foggi, F.V.R. Neuwahl, S. Umapathy, R.E. Hester, and J.N. Moore. **Femtosecond time-resolved UV-visible absorption spectroscopy of trans-azobenzene: dependence on excitation wavelength**. *Chemical Physics Letters*, **290**:68–74, June 1998.

[66] P. Hamm, S.M. Ohline, and W. Zinth. **Vibrational cooling after ultrafast photoisomerization of azobenzene measured by femtosecond infrared spectroscopy**. *The Journal of Chemical Physics*, **106**(2):519, 1997.

[67] N. Biswas and S. Umapathy. **Wavepacket dynamical studies on trans-azobenzene: absorption spectrum and resonance Raman excitation profiles of the n-π* transition**. *Chemical Physics Letters*, **236**:24–29, April 1995. 47

[68] C.G. Morgante and W.S. Struve. **S2-S0 fluorescence in trans-azobenzene**. *Chemical Physics Letters*, **68**:267–271, December 1979. 47

[69] S. Hamai and F. Hirayama. **-**. In *Ann. Symp. Photochem.*, page 315, 1984. 47

[70] B.-Y. Choi, S.-J. Kahng, S. Kim, H. Kim, H. Kim, Y. Song, J. Ihm, and Y. Kuk. **Conformational Molecular Switch of the Azobenzene Molecule: A Scanning Tunneling Microscopy Study**. *Physical Review Letters*, **96**(15):1–4, April 2006. 47, 48

[71] J. Henzl, M. Mehlhorn, H. Gawronski, K.-H. Rieder, and K. Morgenstern. **Reversible cis-trans isomerization of a single azobenzene molecule.** *Angewandte Chemie (International ed. in English)*, **45**(4):603–6, January 2006. 47, 48

[72] J. Henzl, M. Mehlhorn, and K. Morgenstern. **Amino-nitro-azobenzene dimers as a prototype for a molecular-level machine.** *Nanotechnology*, **18**(49):495502, December 2007. 47, 48

[73] M. Alemani, M.V. Peters, S. Hecht, K.-H. Rieder, F. Moresco, and L. Grill. **Electric field-induced isomerization of azobenzene by STM.** *Journal of the American Chemical Society*, **128**(45):14446–7, November 2006. 47, 48

[74] M.J. Comstock, N. Levy, A. Kirakosian, J. Cho, F. Lauterwasser, J. Harvey, D. Strubbe, J. Fréchet, D. Trauner, S. Louie, and M. Crommie. **Reversible Photomechanical Switching of Individual Engineered Molecules at a Metallic Surface**. *Physical Review Letters*, **99**(3):1–4, July 2007. 47, 48

[75] L. Ovari, M. Wolf, and P. Tegeder. **Reversible Changes in the Vibrational Structure of Tetra-tert-butylazobenzene on a Au(111) Surface Induced by Light and Thermal Activation**. *Journal of Physical Chemistry C*, **111**(42):15370–15374, October 2007. 47

[76] S. Hagen, F. Leyssner, D. Nandi, M. Wolf, and P. Tegeder. **Reversible switching of tetra-tert-butyl-azobenzene on a Au(111) surface induced by light and thermal activation**. *Chemical Physics Letters*, **444**(1-3):85–90, August 2007. 47, 48

[77] S. Hagen, P. Kate, F. Leyssner, D. Nandi, M. Wolf, and P. Tegeder. **Excitation mechanism in the photoisomerization of a surface-bound azobenzene derivative: Role of the metallic substrate.** *The Journal of chemical physics*, **129**(16):164102, October 2008. 48, 78

[78] N. Levy, M.J. Comstock, J. Cho, L. Berbil-Bautista, A. Kirakosian, F. Lauterwasser, D.A. Poulsen, J.M.J. Fréchet, and M.F. Crommie. **Self-patterned molecular photoswitching in nanoscale surface assemblies.** *Nano letters*, **9**(3):935–9, March 2009. 47

[79] N. Henningsen, R. Rurali, K. J. Franke, I. Fernández-Torrente, and J. I. Pascual. **Trans to cis isomerization of an azobenzene derivative on a Cu(100) surface**. *Applied Physics A*, **93**(2):241–246, August 2008. 48

[80] J. Henzl and K. Morgenstern. **An electron induced two-dimensional switch made of azobenzene derivatives anchored in supramolecular assemblies.** *Physical chemistry chemical physics : PCCP*, **12**(23):6035–44, June 2010. 48, 49, 60, 61, 76, 82

[81] X. Zhang, Y. Wen, Y. Li, G. Li, S. Du, H. Guo, L. Yang, L. Jiang, H. Gao, and Y. Song. **Molecularly Controlled Modulation of Conductance on Azobenzene Monolayer-Modified Silicon Surfaces**. *Journal of Physical Chemistry C*, **112**(22):8288–8293, June 2008. 48

[82] D. Riedel, M. Cranney, M. Martin, R. Guillory, G. Dujardin, M. Dubois, and P. Sonnet. **Surface-isomerization dynamics of trans-stilbene molecules adsorbed on Si(100)-2 x 1.** *Journal of the American Chemical Society*, **131**(15):5414–23, April 2009. 48

[83] M. Alemani, S. Selvanathan, F. Ample, M.V. Peters, K.-H. Rieder, F. Moresco, C. Joachim, S. Hecht, and L. Grill. **Adsorption and Switching Properties of Azobenzene Derivatives on Different Noble Metal Surfaces: Au(111), Cu(111), and Au(100)**. *Journal of Physical Chemistry C*, **112**(28):10509–10514, July 2008. 48

[84] J. Henzl, T. Bredow, and K. Morgenstern. **Irreversible isomerization of the azobenzene derivate Methyl Orange on Au(111)**. *Chemical Physics Letters*, **435**(4-6):278–282, February 2007. 48

[85] D. E. Brown, D. J. Moffatt, and R. A. Wolkow. **Isolation of an Intrinsic Precursor to Molecular Chemisorption**. *Science*, **279**(5350):542–544, January 1998. 48

[86] C. Dri, M.V. Peters, J. Schwarz, S. Hecht, and L. Grill. **Spatial periodicity in molecular switching.** *Nature nanotechnology*, **3**(11):649–53, November 2008. 48

[87] M. Böhringer, K. Morgenstern, W.-D. Schneider, R. Berndt, F. Mauri, A. De Vita, and R. Car. **Two-Dimensional Self-Assembly of Supramolecular Clusters and Chains**. *Physical Review Letters*, **83**(2):324–327, July 1999. 48

[88] M. Vladimirova, M. Stengel, A. De Vita, and A. Baldereschi. **Supramolecular self-assembly and selective step decoration on the Au (111) surface**. *Europhys. Letters*, **56**(2):254–260, 2001.

[89] J.V. Barth. **Molecular architectonic on metal surfaces.** *Annual review of physical chemistry*, **58**:375–407, January 2007.

[90] J.W. Elemans, S. Lei, and S. De Feyter. **Molecular and supramolecular networks on surfaces: from two-dimensional crystal engineering to reactivity.** *Angewandte Chemie (International ed. in English)*, **48**(40):7298–332, January 2009. 48

[91] J. Miwa, S. Weigelt, H. Gersen, F. Besenbacher, F. Rosei, and T.R. Linderoth. **Azobenzene on Cu(110): adsorption site-dependent diffusion.** *Journal of the American Chemical Society*, **128**(10):3164–5, March 2006. 48

[92] D. Wang, Q. Chen, and L.-J. Wan. **Structural transition of molecular assembly under photo-irradiation: an STM study.** *Physical chemistry chemical physics : PCCP*, **10**(43):6467–78, November 2008.

[93] S. Selvanathan, M.V. Peters, J. Schwarz, S. Hecht, and L. Grill. **Formation and manipulation of discrete supramolecular azobenzene assemblies**. *Applied Physics A*, **93**(2):247–252, August 2008. 48

[94] N. Biswas and S. Umapathy. **Structures, Vibrational Frequencies, and Normal Modes of Substituted Azo Dyes: Infrared, Raman, and Density Functional Calculations**. *The Journal of Physical Chemistry A*, **104**(12):2734–2745, March 2000. 53, 54, 56

[95] D. L. Dexter. **A Theory of Sensitized Luminescence in Solids**. *The Journal of Chemical Physics*, **21**(5):836, 1953. 58

[96] Th. Förster. **Transfer Mechanisms of Electronic Excitation Energy**. *Radiation Research Supplement*, **2**:326, 1960. 58

[97] M. Bazarnik, J. Henzl, R. Czajka, and K. Morgenstern. **Light driven reactions of single physisorbed azobenzenes.** *Chemical communications (Cambridge, England)*, **47**(27):7764–6, July 2011. 58

[98] W. Hofer, a. Fisher, G. Lopinski, and R. Wolkow. **Adsorption of benzene on Si(100)-(2x1) Adsorption energies and STM image analysis by ab initio methods**. *Physical Review B*, **63**(8):1–7, February 2001. 66

[99] Z. Salamon, H.A. Macleod, and G. Tollin. **Surface plasmon resonance spectroscopy as a tool for investigating the biochemical and biophysical properties of membrane protein systems . I : Theoretical principles**. *Biochimica et Biophysica Acta*, **1331**:117–129, 1997. 79

[100] Z. Salamon, H.A. Macleod, and G. Tollin. **Surface plasmon resonance spectroscopy as a tool for investigating the biochemical and biophysical properties of membrane protein systems. II: Applications to biological systems.** *Biochimica et Biophysica Acta*, **1331**(2):131–152, September 1997.

[101] I. Gryczynski, J. Malicka, Z. Grzyczynski, and J.R. Lakowicz. **Radiative decay engineering 4. Experimental studies of surface plasmon-coupled directional emission**. *Analytical Biochemistry*, **324**(2):170–182, January 2004.

[102] I. Gryczynski, J. Malicka, Z. Gryczynski, and J.R. Lakowicz. **Surface Plasmon-Coupled Emission with Gold Films.** *The journal of physical chemistry. B*, **108**(33):12568–12574, July 2004. 79

[103] M.J. Comstock, N. Levy, J. Cho, L. Berbil-Bautista, M.F. Crommie, D.A. Poulsen, and J.M.J. Frechet. **Measuring reversible photomechanical switching rates for a molecule at a surface**. *Applied Physics Letters*, **92**(12):123107, 2008. 81

[104] A. Safiei, J. Henzl, and K. Morgenstern. **Isomerization of an Azobenzene Derivative on a Thin Insulating Layer by Inelastically Tunneling Electrons**. *Physical Review Letters*, **104**(21):1–4, May 2010. 82

List of Figures

2.1 Schematics of the energetic barrier 5
2.2 Elastic and inelastic tunneling processes 6
2.3 Energetic scheme of isomerization processes 15

3.1 Schematics of the STM 18
3.2 Schematics of the I to V converter 19
3.3 Schematic IET signal detection 21
3.4 Lock-in connection schematics 22
3.5 Inelastic electron tunneling manipulation 23
3.6 In-situ light irradiation 24
3.7 Energetic schematics of optical spectroscopies 26
3.8 Flash photolysis experimental set-up 29
3.9 SCF iterations 31

4.1 Photography of RT UHV system - front view 34
4.2 Photography of RT UHV system - back view 34
4.3 Photography of the LT UHV system - front view 36
4.4 Photography of LT UHV system - back view 37

5.1 STM images clean Cu(111) surface 40
5.2 LDOS of the Cu(111) surface 41
5.3 STM images of clean Si(100) surface 42
5.4 Calculated LDOS of Si(100) surface 43
5.5 STS of Si(100) at LT and RT 44
5.6 Possible isomerization pathways for 4-anilino-4'-nitroazobenzene 45

6.1 Calculated structures of *cis* and *trans* 4-anilino-4'-nitroazobenzene . . . 51
6.2 UV-VIS spectroscopy of solid 4-anilino-4'-nitroazobenzene 52
6.3 IR spectroscopy of solid 4-anilino-4'-nitroazobenzene 53
6.4 Raman spectroscopy of solid 4-anilino-4'-nitroazobenzene 55
6.5 UV-VIS spectroscopy of 4-anilino-4'-nitroazobenzene in ACN 57
6.6 Differential absorbance spectroscopy of 4-anilino-4'-nitroazobenzene in ACN 58
6.7 STM images of 4-anilino-4'nitroazobenzene adsorbed at the Cu(111) surface 59
6.8 Assignment of calculated models 61
6.9 STM image of 4-anilino-4'-nitroazobenzene on Cu(111) after local high voltage/high current treatment 62
6.10 STM images of 4-anilino-4'nitroazobenzenes main adsorption configurations at Si(100) 64
6.11 STM image and calculated model of the *trans*-flat configuration 65
6.12 Calculated densities izocontours of the *trans*-flat configuration 66
6.13 Electronic structure of the *trans*-flat configuration 67
6.14 STM image and calculated model of the *trans*-standing configuration . . 69
6.15 Calculated densities izocontours of the *trans*-standing configuration . . . 69
6.16 STM image and calculated model of the *cis*-standing configuration . . . 70
6.17 Calculated densities izocontours of the *cis*-standing configuration 71
6.18 IETS of 4-anilino-4'-nitroazobenzene adsorbed on Cu(111) 73
6.19 IET Manipulation 74
6.20 Yield 75
6.21 IET manipulation of 4-anilino-4'-nitroazobenzene on Si(100) 77
6.22 Photoisomerization of 4-anilino-4'-nitroazobenzene on the Cu(111) surface 79
6.23 Photoisomerization energetic diagram 80
6.24 Photoisomerization of 4-anilino-4'-nitroazobenzene on the Si(100) surface 81

7.1 Top view of a design's computer simulation 89
7.2 Side view of a design's computer simulation 89

List of Tables

6.1 Vibration modes of solid 4-anilino-4'-nitroazobenzene obtained via various methods. In mode names: ip stands for in-plane, oop stands for out-of-plane bending, s stands for stretch, and t stands for torsion. . . . 54

Declaration

I herewith declare that I have produced this paper without the prohibited assistance of third parties and without making use of aids other than those specified; notions taken over directly or indirectly from other sources have been identified as such. This paper has not previously been presented in identical or similar form to any other Polish or foreign examination board.

The thesis work was conducted under the supervision of Prof. Ryszard Czajka at the Institute of Physics, Poznan University of Technology.

Poznan, 25th June 2011